DLR-IB-AS-BS-2017-10

Numerical Parameter Study of a Strake on a Turboprop Engine in Active High-Lift Configuration

Studienarbeit

Yasim Hasan

DLR
Deutsches Zentrum
für Luft- und Raumfahrt

Bericht des Instituts für Aerodynamik und Strömungstechnik
Report of the Institute of Aerodynamics and Flow Technology

DLR-IB-AS-BS-2017-10

Numerical Parameter Study of a Strake on a Turboprop Engine in Active High-Lift Configuration

Y. Hasan, D. Keller

Herausgeber:
Deutsches Zentrum für Luft- und Raumfahrt e.V.
Institut für Aerodynamik und Strömungstechnik
Lilienthalplatz 7, 38108 Braunschweig

ISSN 1614-7790

Stufe der Zugänglichkeit: 1
Braunschweig, im Februar 2017

Institutsdirektor:

Prof. Dr.-Ing. habil. C.-C. Rossow

Verfasser:

cand. mach. Y. Hasan
Dipl.-Ing. D. Keller

Abteilung: Transportflugzeuge

Abteilungsleiter:

Prof. Dr.-Ing. R. Rudnik

Der Bericht enthält:

94	Seiten
75	Bilder
15	Tabellen
29	Literaturstellen

Student Research Project

Numerical Parameter Study of a Strake on a Turboprop Engine in Active High-Lift Configuration

Yasim Hasan

Supervisor: Dipl.-Ing. Dennis Keller
Examiner: Prof. Dr.-Ing. Ralf Rudnik

DLR German Aerospace Center
Institute of Aerodynamics and Flow Technology
Transport Aircraft
Braunschweig

Deutsches Zentrum
für Luft- und Raumfahrt
German Aerospace Center

Statutory Declaration

I declare in lieu of an oath that I have developed and written this Student Research Project, entitled "Numerical Parameter Study of a Strake on a Turboprop Engine in Active High-Lift Configuration", completely by myself, and that I have not used any sources or resources other than stated for its preparation. I further declare that this Student Research Project was not used in the same or in a similar version to achieve an academic grading or is being published elsewhere.

February 01, 2016,
Braunschweig, Germany

Yasim Julian Hasan

Abstract

The engine integration into the wing of an aircraft often has a significant impact on lift generation in high-lift configuration. Within this project, the SFB 880 aircraft, equipped with a droop nose and an active Coanda flap is analysed in the landing configuration. The integration of large turboprop engines leads to strong nacelle vortices that cause a wake burst above the flap inboard of the engine and therefore reduces $C_{L,max}$ recognisably. Therefore, a nacelle strake parameter study is performed, based on an initial strake. The strake optimisation allows for a lift recovery of $C_{L,max}$ by around $17\ LC$ and an increase of α_{max} by $2°$ compared to the configuration without strake. Since nacelle strakes have not been extensively investigated for aircraft with turboprop engines and an active high-lift system, particular attention is paid to the effects of the parameter variations and to the nature of the improvements. It turns out that the lift recovery arises from an effective weakening of the nacelle vortex. This is particularly achieved thanks to a smaller distance between the nacelle and the strake vortex compared to the case with the initial strake. Thereby, the strake vortex shows a very good interaction with the nacelle vortex while its impact on the flow close to the surface is kept low. Hence, a final enlargement of the strake area also allows for an increase of lift. In addition, further potential for an augmentation of $C_{L,max}$ by the utilisation of a supplementary outboard strake is revealed. Finally, the impact of the strake integration on drag in cruise configuration is analysed. Hereby, a drag increase at the beginning of cruise of 0.222% is determined.

Contents

List of Figures

List of Tables

Nomenclature

Abbreviations

CAD	Computer-Aided Design
CFD	Computational Fluid Dynamics
CFL	Courant-Friedrichs-Lewy
DC	Drag count ($1DC \,\widehat{=}\, \Delta C_D = 10^{-4}$)
DLR	Deutsches Zentrum für Luft- und Raumfahrt
DNS	Direct Numerical Simulation
LC	Lift count ($1LC \,\widehat{=}\, \Delta C_L = 10^{-2}$)
LES	Large-Eddy Simulation
RANS	Reynolds-Averaged Navier Stokes
SA	Spalart-Allmaras
SFB	Sonderforschungsbereich
STOL	Short Take-Off and Landing

Latin Symbols

a	Speed of sound
b	Wing span
c	Chord
$\bar{c}$	Mean chord
c_f	Local skin friction coefficient
c_p	Local pressure coefficient
C_l	Section lift coefficient
C_D	Integral drag coefficient
C_L	Integral lift coefficient
C_{L0}	Integral lift coefficient at a zero angle of attack
$C_{L\alpha}$	Integral lift coefficient slope
c_μ	Blowing Coefficient
D	Aerodynamic drag
E	Specific total energy
f	Size factor
F	Thrust
$\vec{F}$	Flux density vector

$\overline{\overline{F}}$	Flux density tensor
h	Root chord-semispan ratio
H	Specific total enthalpy
k	Coefficient of thermal conductivity
l	Characteristic length
L	Aerodynamic lift
L'	Section lift
$\dot{m}$	Mass flow
Ma	Mach number
$\vec{n}$	Normal vector
p	Static pressure
p_t	Total pressure
Pr	Prandtl number
q	Dynamic pressure
Q	Heat transfer
$\vec{r}$	Distance vector
Re	Reynolds number
s	Wing semispan
$\dot{s}$	Stretching rate
S	Wing area
T	Static temperature
u	Velocity component in x-direction
v	Velocity component in y-direction
w	Velocity component in z-direction
$\vec{v}$	Velocity vector
V	Absolute value of velocity
$\vec{W}$	Vector of conservative variables
y^+	Dimensionless wall distance

Greek Symbols

α	Angle of attack
$\widetilde{\alpha}$	Dissipation term
δ	Boundary layer thickness
δ_a	Aileron deflection angle
δ_{dn}	Droop nose angle
δ_f	Flap deflection angle
Γ	Circulation
ϑ	Dihedral angle
Λ	Aspect ratio
μ	Dynamic viscosity
ν	Kinematic Viscosity
ρ	Density
$\overline{\overline{\tau}}$	Viscous stress tensor
τ_W	Wall shear stress

φ	Sweep angle
$\vec{\omega}$	Vorticity vector
ω_k	Kinematic vorticity number
Ω	Computational domain

Other Symbols

∇	Nabla-operator
$\triangle$	Laplace-operator

Super- and subscripts

$\widetilde{x}$	*Favre*-averaged value
x'	Turbulent fluctuation value
x^l	Value at laminar flow
x^t	Modelled value due to turbulence
x_{max}	Maximum value
x_{res}	Residual
x_S	Strake
x_∞	Free stream value
x_Θ	Tangential component

1 Introduction

The trend of increasing global air traffic brings new challenges and leads to growing requirements for future aircraft. With respect to environmental protection, a higher efficiency needs to be provided and fuel consumption has to be reduced. Besides, the capacities of major airports are likely to be exceeded by the higher amount of flights while smaller airports often only possess shorter runways [3]. Therefore, a desirable feature for future aircraft would be a short take-off and landing distance, which implies the need for more effective high-lift systems. In addition, the reduction of aircraft noise emissions has become increasingly important in recent years.

In order to design an aircraft that fulfills these requirements, the interdisciplinary research project SFB (*Sonderforschungsbereich*) 880, which is a collaboration of the German Aerospace Center, the Technical University of Braunschweig and the Leinbniz University of Hannover, was launched in 2011. Within the scope of this project a STOL (*Short Take-Off and Landing*) aircraft configuration, based on new technologies, is investigated in terms of noise emission, efficient high-lift generation and flight dynamic aspects. The aircraft concept envisages the deployment of a droop nose and an active blown Coanda flap in order to realise a take-off and landing distance of less than $800\ m$. Since such a so-called active high-lift system operates without slots, it is assumed that noise emission can herewith be reduced [17]. According to the concept, the aircraft shall be equipped with two turboprop engines and is supposed to permit a maximal payload of about 100 passengers or $12\ 000\ kg$ respectively. With a cruise Mach number of 0.74, its target range shall be around $2\ 000\ km$ [27].

The SFB 880 aircraft is continuously examined and enhanced by the participating research scientists. Within this design and development process, the initial conceptional turboprop model has also been replaced by a more detailed engine. This modification of the turboprop has particularly resulted in an increased nacelle size. As a consequence, the larger size of the nacelle has a significant influence on the aerodynamic quality of the aircraft. The shedding of strong vortices on the nacelle weakens the flow and leads to a reduced performance of the flap. As a result, a significant lift loss at high angles of attack is suffered.

Nacelle strakes are known to remedy this and to allow for a partly lift recovery. Hereby, the strakes, which are small plates attached to the nacelle, serve as vortex generators. The vortices shed by the strake are normally used in order to counteract undesired vortices, whose nature is mostly an interference effect due to the installation of engines.

1.1 State of the Art

The use of nacelle strakes is widespread for conventional aircraft. Thereby, the actual position on the nacelle, the setting angle and the form of the strake can vary recognisably. The optimal set of strake parameters depends on the actual geometry of the complete engine, the slat and the arrangement of the junction [10]. Since the strake effect is very sensitive to its position, it needs to be designed very thoroughly.

Nacelle strakes are almost exclusively utilised for conventional aircraft with a turbofan engine in combination with a slat and a cutout at the junction, required for the installation of the nacelle. Here, the strake is mostly used to suppress separation that would occur because of vortices, shed either due to the cutout or due to the nacelle. The downwash of the strake vortex has a stabilising effect on the local flow. Thereby, an inboard strake is usually mounted, which is only sometimes complemented by an outboard strake. Many different strakes have been investigated for these kind of configurations [8], [15], [16], [19], [29].

However, the SFB 880 aircraft is equipped with a turboprop engine and a droop nose. In addition, the negative effect of the engine integration leads to a wake burst above the flap rather than to separation at the leading edge. Therefore, the effects of the engine integration are supposed to be different here. Most conventional aircraft containing turboprop engines are operated without strakes. Nevertheless, the A400M from *Airbus* which has nacelles of similar size also possesses very small nacelle strakes near the wing's leading edge. However, the A400M differs from the SFB aircraft by its high-lift system. It is equipped with a double slotted flap and has a fixed, slightly drooped leading edge [18].

1.2 Outline

Within this research project, an inboard nacelle strake shall be found that allows for a lift recovery of the lift loss caused by the integration of the larger nacelles. Therefore, the case without strake will first be analysed in detail in order to obtain an understanding of the flow phenomena caused by the nacelle vortices and of the nature of the lift loss. In order to provide a good resolution of the vortices and other flow phenomena, the hybrid unstructured grid will be extended by structured elements on the wing and in the wake of the vortices. The grid will furthermore be evaluated in terms of quality. Subsequently, an initial strake that has been designed within a foregoing study shall be optimised within an extensive nacelle strake parameter study with the aim to maximise $C_{L,max}$. Hereby, the efforts are not only limited to the increase of lift. Due to the little knowledge concerning nacelle strakes in the case of a turboprop engine and an active high-lift system, special attention will also be paid to the effects of strake parameter variations. The optimised strake and its effects shall then be analysed in detail. In a final step, the nacelle strake impact on the drag coefficient in cruise flight will be determined and compared both with the case without strake and with the configuration containing the initial strake.

2 Theoretical Background

In this chapter the theoretical background of this research project shall be explained. Therefore, a short introduction into the basic conservation laws of fluid mechanics will be given and the fundamentals of vortices will be described. In addition, an insight into aircraft aerodynamics will be provided and high-lift-devices as well as their functionality will be presented in detail. Finally, the basics of Computational Fluid Dynamics and the underlying principles will be explained.

2.1 Governing Equations

The general behaviour of a fluid, supposed to be a continuum, can be described by three conservation laws: the conservation of mass (Eq. 2.1), the conservation of momentum (Eq. 2.2) and the conservation of energy (Eq. 2.3). These equations form the so-called complete system of the *Navier-Stokes equations*. This is a set of non-linear partial differential equations of second order. Since analytical solutions only exist for simplified problems, the set of *Navier-Stokes equations* needs to be solved numerically [1].

Conservation of Mass

The change of mass within a stationary finite control volume Ω depends only on the mass flux across the outer surface $\partial\Omega$ of the control volume. The integral form of the so-called continuity equation can therefore be written as

$$\frac{\partial}{\partial t}\iiint\limits_{\Omega}\rho\, d\Omega + \iint\limits_{\partial\Omega}\rho\left(\vec{v}\cdot\vec{n}\right)\, dS = 0, \tag{2.1}$$

where ρ denotes the density, $\vec{v}$ is the flow velocity vector and $\vec{n}$ is the unit normal vector [1].

Conservation of Momentum

If we assume the absence of external forces, the momentum inside the control volume changes due to the transport of momentum across the outer surface as well as to the pressure distribution and the stresses on the boundary. The integral form of the momentum equation can then be written as

$$\frac{\partial}{\partial t}\iiint\limits_{\Omega}\rho\vec{v}\,d\Omega+\iint\limits_{\partial\Omega}\rho\vec{v}\cdot(\vec{v}\cdot\vec{n})\,dS+\iint\limits_{\partial\Omega}p\vec{n}\,dS=\iint\limits_{\partial\Omega}\overline{\overline{\tau}}\cdot\vec{n}\,dS. \tag{2.2}$$

Here, p denotes the pressure distribution and $\overline{\overline{\tau}}$ is the viscous stress tensor, containing both shear and normal stresses [1].

Conservation of Energy

Finally, assuming that there is no energy contribution of radiation or chemical reactions, the energy equation without external forces shall be presented. The total energy inside the control volume changes due to the total enthalpy flux across the boundary, the work done by the stresses and the heat transfer as a result of thermal conduction. The integral form of the energy equations is then

$$\frac{\partial}{\partial t}\iiint\limits_{\Omega}\rho E\,d\Omega+\iint\limits_{\partial\Omega}\rho H\left(\vec{v}\cdot\vec{n}\right)\,dS=\iint\limits_{\partial\Omega}\left(\overline{\overline{\tau}}\cdot\vec{v}\right)\cdot\vec{n}\,dS+\iint\limits_{\partial\Omega}k\left(\nabla T\cdot\vec{n}\right)\,dS. \tag{2.3}$$

The specific total enthalpy can be obtained by $H = E + p/\rho$, whereby the specific total energy E contains the specific kinetic and the specific internal energy of a volume element. Here, k denotes the thermal conductivity coefficient and T is the temperature distribution [1].

2.2 Aircraft Aerodynamics

As a result of the flow around an aircraft, a characteristic flow field is created and aerodynamic forces and moments are induced. Within the field of aircraft aerodynamics, specific flow features and their dependency on the aircraft's geometry are investigated. The aerodynamic forces and moments are usually represented in form of dimensionless quantities.

2.2.1 Similarity Parameters

The flow field only depends on the aircraft's geometry and the similarity parameters and is therefore independent of the absolute values of the flow parameters and geometry. Assuming a rigid aircraft and steady flow, there are two similarity parameters:

- The Reynolds number, given by

  $$Re = \frac{\rho V l}{\mu} \tag{2.4}$$

  with a characteristic length l and the dynamic viscosity μ presents the relation between inertial forces and viscous forces and is therefore a measure of the influence of viscosity [21].

- The Mach number represents the influence of compressibility effects. It is the ratio of flow speed and the speed of sound a [21]:

$$Ma = \frac{V}{a}. \tag{2.5}$$

If these two similarity parameters Re and Ma are identical and if two bodies are geometrically similar, similitude is guaranteed and the flow field around these bodies are mechanically similar [21].

2.2.2 Circulation

The concept of circulation plays an important role for bodies generating lift. Circulation is defined as the line integral of the velocity field along the closed curve ∂A [21]:

$$\Gamma = \oint_{\partial A} \vec{v} \, d\vec{s} \tag{2.6}$$

It is a scalar that has values different from zero if lift is produced by a body in a potential flow. It can be interpreted as the superposition of the translation flow around that body without lift and a vortex and thus leads to a rotation of the flow field [21]. Figure 2.1 depicts the circulation for a two-dimensional airfoil profile in a non-viscous flow. On the basis of this figure, we can easily see that circulation is related to lift.

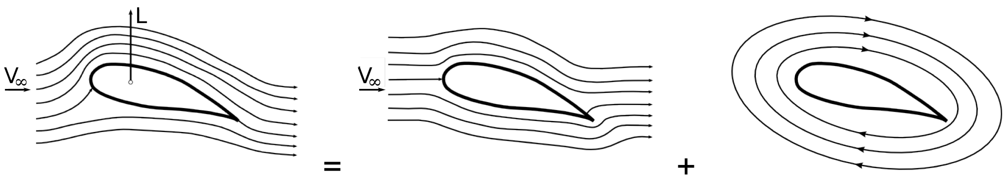

(a) Flow field with lift (b) Translation flow (c) Circulation flow

Figure 2.1: Subdivision of the flow field around an airfoil profile (based on [21])

According to the *Kutta-Joukowski theorem*, there is a linear relation between circulation and lift produced by an airfoil profile, namely

$$L' = \rho V_\infty \Gamma, \tag{2.7}$$

where L' denotes the section lift [21].

2.2.3 Aerodynamic Coefficients

On a body in an oncoming flow, aerodynamic forces and moments are generated. In order to make these forces and moments independent of absolute values and to provide comparability they are scaled with the dynamic pressure of the free stream

$$q_\infty = \frac{\rho}{2} V_\infty^2 \tag{2.8}$$

and geometric quantities and thus expressed in form of dimensionless coefficients. These coefficients are then only dependent on the geometry and the similarity parameters Re and Ma (see subsection 2.2.1). The aerodynamic coefficients that will be important in this project shall be presented in the following. Aerodynamic drag D of an aircraft is given by the integral drag coefficient

$$C_D = \frac{D}{q_\infty S}, \tag{2.9}$$

with the wing area S. In analogy, lift is expressed by means of the integral lift coefficient

$$C_L = \frac{L}{q_\infty S}. \tag{2.10}$$

In the range of low angles of attack α of the aircraft relative to the flow direction, the lift coefficient is supposed to be linearly dependent on the angle of attack

$$C_L = C_{L\alpha} \cdot \alpha + C_{L,0}. \tag{2.11}$$

At high angles of attack a non-linear decrease of the slope of the lift curve occurs that gets stronger along with the angle of attack, see also Figure 2.4. This is caused by separation. In an incompressible, non-viscous fluid, the derivative $C_{L\alpha} = \partial C_L / \partial \alpha$ depends mainly on the shape of the wing, given by the aspect ratio

$$\Lambda = \frac{b^2}{S}. \tag{2.12}$$

Thereby, b denotes the wing span. According to the *Prandtl lifting-line-theory*, the $C_{L\alpha}$ of wings with a high aspect ratio can be approximated as [22]

$$C_{L\alpha} = 2\pi \frac{\Lambda}{\Lambda + 2}. \tag{2.13}$$

Furthermore, the local coefficients c_f and c_p can be defined. The skin friction coefficient c_f constitutes the dimensionless local skin friction τ:

$$c_f = \frac{\tau_W}{q_\infty} \tag{2.14}$$

And finally, the dimensionless pressure coefficient c_p presents the pressure difference between the local static pressure p and the free stream static pressure p_∞:

$$c_p = \frac{p - p_\infty}{q_\infty} \tag{2.15}$$

At a local stagnation point c_p is 1 and if the local velocity is higher than the free stream velocity, c_p is smaller than 0.

2.3 Fundamentals of Vortices

The movement of a fluid element consists of a translatory and a rotationary part. The rotationary part can be quantified by the so-called vorticity $\vec{\omega}$ which can be obtained by the rotation of the velocity field [25]:

$$\vec{\omega} = \mathrm{rot}\ \vec{v} = \nabla \times \vec{v} \tag{2.16}$$

A flow without rotation ($\vec{\omega} = \vec{0}$) is then called translation flow while a pure rotational movement of fluid elements around a rotational axis is called a vortex. The definition of circulation (Eq. 2.6) can now be rewritten using the *Stokes' theorem* [25]:

$$\Gamma = \oint_{\partial A} \vec{v}\, d\vec{s} = \iint_{A} \vec{\omega} \cdot \vec{n}\, dS \tag{2.17}$$

Thus, circulation can be obtained if we form the integral of the vorticity field over surface A. According to Equation 2.7, there exists consequently a relation between lift and vorticity.

2.3.1 The *Helmholtz's Theorems*

The general three-dimensional behaviour of vortices in a non-viscous flow is characterised by the three *Helmholtz's theorems*, namely:

1. A fluid element that is irrotational from the beginning stays irrotational. As a consequence, vorticity of a fluid element is constant in time [21].
2. All fluid elements that are part of a vortex filament remain part of the vortex filament [21]. This means that vortex filaments move along with the fluid.
3. The strength of the vortex filament, which is circulation, is constant along the vortex filament. Therefore, vortex filaments either need to be closed or continue to the boundaries of the flow field [21].

2.3.2 The *Biot-Savart Law*

The *Biot-Savart law* states that vortices have an impact on the surrounding flow field. A vortex filament induces a velocity at a point P in the form of

$$\vec{v} = \frac{\Gamma}{4\pi} \oint_{s} \frac{\vec{r} \times d\vec{s}}{|\vec{r}|^3}. \tag{2.18}$$

where $\vec{r}$ is the position vector of point P originating from the vortex filament and s is a path along the vortex filament [21]. So, vortices induce a point symmetric velocity field around their center line, decreasing with the distance. The flow field is superimposed by this induced velocity field.

2.3.3 Horseshoe Vortex Model

The third *Helmholtz theorem* has an important consequence on the three-dimensional wing with limited span, that generates lift [21]. We suppose a wing, that generates lift so that circulation is constant along the span direction, see Figure 2.2. According to the Equations 2.7 and 2.17 this is synonymous with a non-zero vorticity which is constant along the span direction. We can therefore model vorticity with a bound vortex of the strength Γ along the wing (see also Figure 2.1). However, due to the third *Helmholtz theorem*, the vortex cannot end at the wing's tips where no lift is generated. Hence, two trailing tip vortices are shed. In order to model a closed path of the vortex filament, these vortices are connected far downstream by the starting vortex. This model is called horseshoe vortex model because of the characteristic shape of the vortex filament resembling a horseshoe [21].

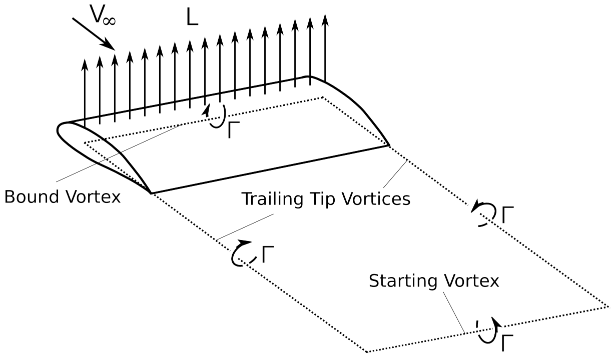

Figure 2.2: Horseshoe vortex of a wing with a uniform lift distribution (based on [21])

The trailing tip vortices in this model are of significant importance. On the one hand, they induce a downwash behind the trailing edge according to the *Biot-Savart law* (see subsection 2.3.2) that leads to an induced angle of attack and thus to induced drag [22]. On the other hand, the vortex itself plays a decisive role in civil aviation and the regulation of air traffic since it has a major impact on wake turbulence. Within this project, it will be of particular interest when it comes to the functionality of nacelle strakes in section 2.5.

2.3.4 Kinematic Vorticity

In the boundary layer of a body in an oncoming flow, high velocity gradients can occur. According to Equation 2.16 this can lead to high values of vorticity even if this might be caused by shear. In order to distinguish between a pure rotational movement of fluid elements and irrotational pure shear, the so-called kinematic vorticity number ω_k can be used. It is defined as the ratio between vorticity and the three components of the stretching rate $\dot{s_1}$, $\dot{s_2}$ and $\dot{s_3}$ [24]:

$$\omega_k = \frac{|\vec{\omega}|}{2\sqrt{\dot{s_1}^2 + \dot{s_2}^2 + \dot{s_3}^2}} \tag{2.19}$$

According to this definition, a pure shear deformation results in a kinematic vorticity number $\omega_k \to 0$ while a pure rotational movement leads to $\omega_k \to \infty$ [24].

2.4 High-Lift Devices

In order to increase the lift generation in low speed of an aircraft, so-called high-lift devices are used. Since lift depends quadratically on the flight velocity (Equation 2.10), very high landing and take-off velocities would be necessary in the cruise configuration, resulting in high landing and take-off distances. Therefore, a wide range of leading- and trailing-edge devices are employed. Today, slotted multi-element-devices are mostly utilised in civil aviation [6]. These high-lift systems make use of gap effects that keep the air attached at higher angles of attack and increase lift [23]. However, these slotted high-lift-devices are critical in terms of noise emission. In order to reduce noise, single-element devices without gaps paired with active circulation control, so-called active high-lift systems can be used. [12].

2.4.1 Droop Nose and Coanda Flap

Within the framework of this work a single-element high-lift system deploying a droop nose and an active Coanda flap will be of interest. Figure 2.3 shows the structure of such an airfoil. These types of high-lift-devices work through the variation of the airfoil's geometry. The radius of the nose, having a significant influence on the pressure distribution, can be adapted. By varying the nose radius, the magnitude of low-pressure peaks, provoking separation, can be reduced [3]. In addition, a deflection of the flap and the drooping of the nose lead to an increase of camber of the mean line compared to the basic configuration. The theoretical maximum local lift coefficient $C_{l,max}$ of a body in a non-viscous flow can be reached by a closed mean line in the shape of a circle [23]. As can be seen in Figure 2.3, the mean line in the high-lift configuration comes closer to the shape of a half-circle and circulation is thus increased. However, the increase of camber is limited by the appearance of separation. In order to increase the flap deflection angle and to reach higher angles of attack and therefore higher lift coefficients, active circulation control systems can be deployed [12]. Hereby, air is blown out of small slots so that it flows tangentially to the surface. Thanks to the *Coanda effect*, the flow stays attached, even at higher turning angles. As a result, higher airfoil camber can be realised and trailing edge separation is likely to be shifted to higher angles of attack.

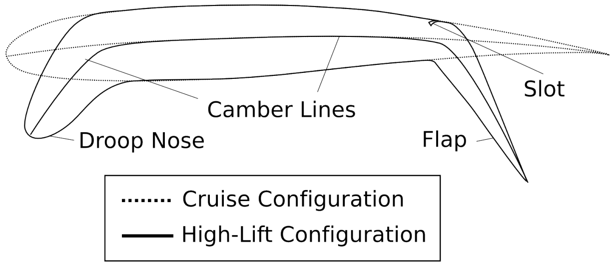

Figure 2.3: Structure of a single-element airfoil with a droop nose and a flap

The *Coanda Effect*

The tendency of a jet in a viscous flow to attach to other jets or to a wall is called *Coanda effect*. While normal tangential flows are only capable to follow a convex surface for a short time until separation occurs, a jet stays attached to the wall for a much longer time. In order to use this effect, an air jet is blown out of slots along a surface. The air between the jet and the convex surface is entrained by the jet because of momentum transport, leading to a local pressure reduction. The jet itself prevents air inflow from the outer flow so that a pressure gradient occurs, forcing the jet to follow the wall. This results in a curved streamline [12]. The air jet is then able to follow very high deflection angles.

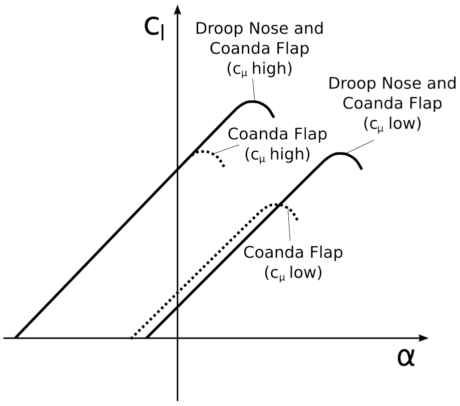

Figure 2.4: Qualitative effect of an active high-lift system on the lift curve (based on [3])

Figure 2.4 shows a simplified sketch of the local lift curve of such an active high-lift system, based on the investigations of [3]. Here, the influence of the droop nose and of the blowing coefficient c_μ, which is defined as a dimensionless momentum coefficient [14], namely

$$c_\mu = \frac{\dot{m}_{jet} V_{jet}}{q_\infty S_{ref}}, \tag{2.20}$$

on the local maximum lift coefficient $c_{l,max}$ and its corresponding angle of attack α_{max} is of particular interest. We see that the droop nose leads a shift of separation to higher angle of attacks and thus to higher lift coefficients. The variation of the blowing coefficient results in an overall shift of the lift curve to higher c_l while α_{max} is decreased at the same time. Additionally, the blowing coefficient influences the lift curve with droop nose. While lift at low angles of attack is higher for a clean nose configuration, a higher blowing coefficient results in similar values of c_l in that region. It should be taken into account that Figure 2.4 only describes the effect of c_μ and the droop nose on α_{max} and $c_{l,max}$. However, the different blowing rates also have an impact on the stall behaviour, leading to different mechanisms [3]. This figure does not depict these mechanisms. Nevertheless, we see that the use of an active high-lift system can significantly increase the maximum lift coefficient.

The possible flow turning angles and thus the amount of circulation can be adapted with the help of the blowing coefficient c_μ. Hereby, two different modes can be utilised:

- The *Boundary layer control mode* can be used to control the behaviour of the boundary layer and to adjust the occurance of separation to reach the highest efficiency. [14]

- The *Super-Circulation mode* is used to increase circulation by additional blowing beyond the point of a fully attached flow [14].

In order to achieve the highest efficiency, it is furthermore possible to separate the slots into spanwise sections in order to control the local amount of circulation respecting the local flow field [14].

2.5 Nacelle Strakes

The integration of engines into the wing can lead to interference effects that are most crucial in the high-lift configuration. Thereby, the maximum lift coefficient can be reduced significantly [10]. However, in order to reduce these interference effects and to allow for a recovery of $C_{L,max}$, nacelle strakes can be used. The effects of strakes is explained in the following section.

2.5.1 Engine Interference Effects in case of a Turbofan Engine and Slats

The integration of a turbofan engine requires a cut-out in the slat. The local absence of the slat results in two slat vortices shed inboard and outboard of the cutout. This leads to a flow separation at the leading edge that propagates to the trailing edge [10]. Hereby, the area inboard of the pylon is often the most critical region for twin engine aircraft. Associated with the premature flow separation, the lift decreases considerably. The nacelle itself may have a counteracting effect. At high angles of attack it generates lift and two nacelle vortices are shed. The inboard nacelle vortex may induce a downwash in the region of separated flow according to subsection 2.3.2, suppressing or reducing separation [10]. However, the flow field in the region of the junction is very complex, containing various shear layers [8] and it depends strongly on the geometry of the junction and the cut-out [10]. 2.5(a) shows an exemplary pylon-nacelle-junction

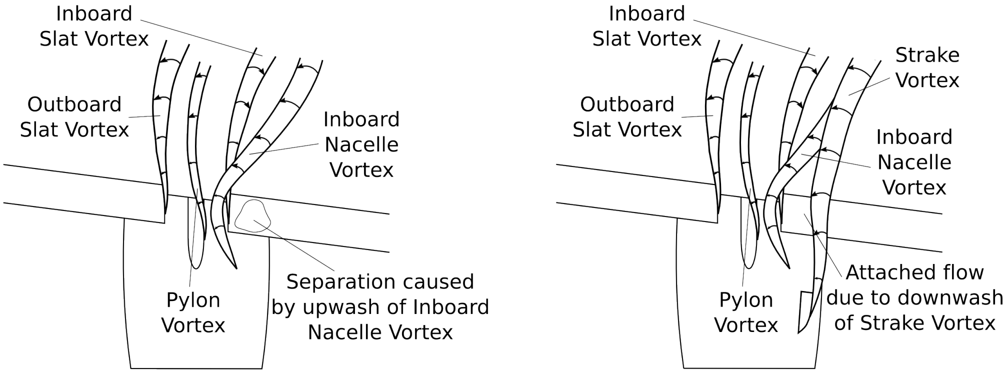

(a) Configuration without strake (b) Configuration with strake

Figure 2.5: Sketch of the essential vortices at the junction (based on [26])

and illustrates the essential vortices in this area, namely the slat vortices, the inboard nacelle vortex and the vortex shed by the pylon. In this case, there is separation on the slat inboard of the nacelle, which is here mainly caused by the nacelle vortex. Since it propagates through the cut-out, it passes the wing very close to the surface, inducing an upwash on the inboard slat which leads to the separation. Subsequently, the slat separation triggers a trailing edge separation on the main wing [26].

The basic idea of strakes is to generate another vortex, that can keep the flow attached and furthermore minimise the engine interference effects and thus lead to a recovery of lift. Nacelle strakes are vortex generators in the form of flat plates attached to the nacelle [10]. As presented in 2.5(b), the strake vortex passes the wing at a position inboard of the junction. Thereby, the strake vortex interacts with the nacelle vortex and induces an additional downwash in the region of the separated flow, strengthens the boundary layer and keeps it attached [10]. If the strake is properly configured, the upwash is induced in a less critical area. In this manner, the utilisation of optimised nacelle strakes can lead to a regain of most of the loss, caused by the integration of the engine [16]. However, the effect of nacelle strakes is very sensitive to both the strength of the generated vortex and to the position on the nacelle [8]. As a consequence, nacelle strakes need to be dimensioned very thoroughly.

Total Pressure

As explained above, a strake can induce a downwash at a critical region and entrain flow of the outer flow field into the boundary layer. This way, the low-energy boundary layer is re-energised by the outer high energy flow and thus strengthened [29]. This circumstance and the energy loss due to high gradients inside a vortex, especially at the core, suggest that the total pressure can be used to determine the local effect of the strake. The total pressure for a non-compressible flow is defined as

$$p_t = p + q. \tag{2.21}$$

The nacelle strake's position and geometry can also be optimised by examination of the total pressure loss and its reduction near the wing's surface in the critical region.

2.5.2 Engine Interference Effects in case of a Turboprop Engine and a Droop Nose

Within the framework of this project the aircraft's wing is equipped with a turboprop engine and a droop nose. In contrast to subsection 2.5.1 the engine interference effects are thus different and less critical. Turboprop engines are very closely connected to the wing, as can be seen on Figure 2.6. As a consequence, pylons are not necessary for the integration and the break of the droop nose can be realised without large gaps. Together with the lower aerodynamic load applied to the droop nose compared to the load on slats (as pointed out in subsection 2.4.1) there are no strong leading edge vortices present. Nevertheless, the vortices shed by the nacelle at high angles of attack interact with the flow field. As a result of the close integration of the turboprop, the vortices pass very close to the upper wing's surface and weaken the boundary layer

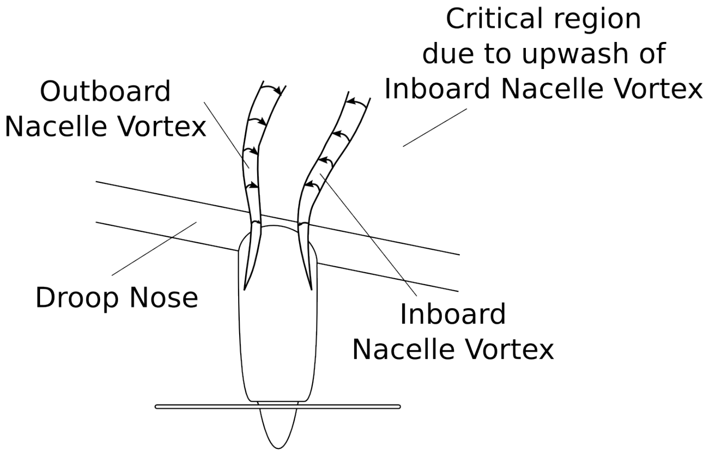

Figure 2.6: Sketch of the essential vortices at the turboprop-droop nose-intersection

near the trailing edge in the region of the induced upwash. Therefore, strakes can be used to minimise the negative effect caused by the nacelle vortices.

2.6 Turbulence

A turbulent flow is characterised by fluctuations of the main parameters of the flow field. While laminar flows are composed of different layers with relatively low interaction, the molecules in a turbulent flow move across the different layers in a chaotic way, causing a higher momentum and energy exchange [1]. This leads to high-frequent variations of temperature, pressure and the velocity components and provokes a seemingly higher viscosity [2]. Moreover, according to the phenomena of the energy cascade, it is assumed that turbulent energy is obtained at large scales and is, due to the decomposition into smaller whirls, finally dissipated. Turbulence is therefore present at a large frequency range and can only be supposed to be quasi-stationary if averaged over a sufficient interval [2].

The consideration of turbulence in a numeric flow simulation can be achieved in different ways. First of all, a direct simulation of the turbulent structures, called *Direct Numerical Simulation* (DNS) would be possible. Alternatively, the *Large-Eddy Simluation* (LES) can be used in order to simulate large scale turbulence and to model the small scales. However, such simulations require a very high computational effort so that their application is limited to simple flow problems [1].

2.6.1 The *Reynolds-Averaged Navier Stokes Equations*

A more effective way to take turbulence into account is the numerical solution of the so-called *Reynolds-Averaged Navier Stokes* (RANS) equations. Hereby, all parameters are *Reynolds*-averaged which means their decomposition into an average value and a turbulent fluctuation. In our case, the mass-weighted average, the so-called *Favre-Average* is used [9] :

$$v_i = \widetilde{v}_i + v_i' \tag{2.22}$$

The application of this decomposition to the flow parameters and the subsequent averaging of the governing equations leads to the averaged *Navier-Stokes equations*, which are here given in the differential form in tensor notation for reasons of clarity and compactness and under neglection of the molecular diffusion and the turbulent transport of the turbulent kinetic energy [1], [9]:

$$\begin{gathered}
\frac{\partial \widetilde{\rho}}{\partial t} + \frac{\partial}{\partial x_i}\left(\widetilde{\rho}\widetilde{v}_i\right) = 0 \\
\frac{\partial}{\partial t}\left(\widetilde{\rho}\widetilde{v}_i\right) + \frac{\partial}{\partial x_j}\left(\widetilde{\rho}\widetilde{v}_i\widetilde{v}_j\right) + \frac{\partial \widetilde{p}}{\partial x_i} = \frac{\partial}{\partial x_j}\left(\widetilde{\tau}_{ij} - \widetilde{\rho}\widetilde{v_i'v_j'}\right) \\
\frac{\partial}{\partial t}\left(\widetilde{\rho}\widetilde{E}\right) + \frac{\partial}{\partial x_j}\left(\widetilde{\rho}\widetilde{v}_j\widetilde{H}\right) = \frac{\partial}{\partial x_j}\left[\widetilde{v}_i\left(\widetilde{\tau}_{ij} - \widetilde{\rho v_i'v_j'}\right)\right] + \frac{\partial}{\partial x_j}\left(k\frac{\partial \widetilde{T}}{\partial x_j} - \widetilde{\rho v_j'h'}\right)
\end{gathered} \tag{2.23}$$

As can be seen, there are now two additional terms compared to Equations 2.1 - 2.3, namely the symmetric *Reynolds stress tensor*

$$\tau_{ij}^t = -\widetilde{\rho}\widetilde{v_i'v_j'}, \tag{2.24}$$

containing six additional unknown components and the turbulent heat transfer

$$\dot{Q}^t = -\frac{\partial}{\partial x_i}\widetilde{\rho v_j'h'}, \tag{2.25}$$

adding three additional variables [1]. The task of turbulence models is to provide further equations and to close this set of equations. There are different types of turbulent models for the RANS equations, that can be classified by their order. First order models can be distinguished by the number of equations employed to describe the transport of a turbulent variable while in second order models the turbulent stress tensor is defined by an algebraic definition [1]. In this work, the *Spalart-Allmaras turbulence model* will be used and in the following section we will therefore concentrate on this model.

2.6.2 The *Boussinesq Eddy-Viscosity Hypothesis*

According to the *eddy-viscosity hypothesis*, turbulent stresses behave similar to laminar stresses and depend on the mean flow. Therefore the turbulent shear stresses are supposed to be linearly related to the strain rates with a turbulent equivalent to the molecular viscosity, namely the eddy viscosity μ^t [1]. In addition, the turbulent heat flux vector is then approximated as

$$-\frac{\partial}{\partial x_i}\widetilde{\rho v_j'h'} = k^t\frac{\partial \widetilde{T}}{\partial x_i} = c_p\frac{\mu^t}{Pr^t}\frac{\partial \widetilde{T}}{\partial x_i}, \tag{2.26}$$

with the turbulent Prandtl number $Pr^t = 0.9$ and the specific heat coefficient c_p [1]. In order to respect these approximations in the averaged *Navier-Stokes equations* mentioned above, the dynamic viscosity and the thermal conductivity coefficient are simply replaced by the expressions [1]

$$\begin{aligned} \mu &= \mu^l + \mu^t \\ k &= k^l + k^t = c_p \left(\frac{\mu^l}{Pr^l} + \frac{\mu^t}{Pr^t} \right), \end{aligned} \tag{2.27}$$

where the superscript "l" denotes the molecular values, that would occur in a pure laminar flow. The values superscripted with "t" are the modelled parameters, respecting the turbulent character of the flow. As can be seen from Equation 2.27, the closure problem of the nine additional unknown variables has been reduced to a problem with the eddy viscosity as the only additional variable. Thus, a single supplementary equation becomes necessary to close the set of equations.

2.6.3 The *Spalart-Allmaras Turbulence Model*

The *Spalart-Allmaras turbulence model* is a first-order closure one-equation model based on the eddy-viscosity hypothesis explained in subsection 2.6.2. It is a transport equation for the SA viscosity $\widetilde{\nu}$, that is defined as

$$\mu^t = f_{v1} \widetilde{\rho} \widetilde{\nu}, \tag{2.28}$$

where f_{v1} denotes a damping function in dependency of the viscosity ratio $\widetilde{\nu}/\nu^l$ [9] (see appendix A.1 for further information). According to the model, the SA viscosity inside a control volume changes due to certain source terms, basically the production, the diffusion and the destruction of $\widetilde{\nu}$. With the closest wall distance d and the molecular kinematic viscosity ν^l, the basic equation of the *Spalart-Allmaras turbulence model* can be written as [1], [9]

$$\begin{aligned} \frac{\partial \widetilde{\nu}}{\partial t} + \frac{\partial}{\partial x_j} \left(\widetilde{\nu} v_j \right) = \; & \underbrace{C_{b1} \left(1 - f_{t2} \right) \widetilde{S} \widetilde{\nu}}_{\text{Production}} \; + \; \underbrace{\frac{1}{\sigma} \left[\frac{\partial}{\partial x_j} \left(\left(\nu^l + \widetilde{\nu} \right) \frac{\partial \widetilde{\nu}}{\partial x_j} \right) + C_{b2} \frac{\partial \widetilde{\nu}}{\partial x_j} \frac{\partial \widetilde{\nu}}{\partial x_j} \right]}_{\text{Diffusion}} \\ & - \; \underbrace{\left(C_{w1} f_{w1} - \frac{C_{b1}}{\kappa^2} f_{t2} \right) \left(\frac{\widetilde{\nu}}{d} \right)^2}_{\text{Destruction}} \; - \; \underbrace{\frac{1}{\sigma} \left(\nu^l - \widetilde{\nu} \right) \frac{\partial \widetilde{\rho}}{\partial x_j} \frac{\partial \widetilde{\nu}}{\partial x_j}}_{\text{Compressibility Effects}}. \end{aligned} \tag{2.29}$$

All other terms occuring in Equation 2.29 are generic relations, containing empiric values. Further detailed information on the terms is provided by appendix A.1. Depending on the version of the *Spalart-Allmaras turbulence model*, supplementary terms can be added to the transport equation [9]. In this case, the term considering compressibility effects is explicitly mentioned, because it is integrated in the turbulence model, employed within this project. It is added to the equation since the diffusion term does not include compressibility effects and is therefore non-conservative [1], [9]. Finally, the RANS equation together with the *Spalart-Allmaras turbulence model* form a closed set of equations that needs to be solved in order to obtain a numerical solution of a flow problem.

The *Spalart-Allmaras turbulence model* has, like practically all turbulence models, strengths and weaknesses. One of its main advantages is clearly the low computational effort, paired with robustness and a fast convergence even at a moderate grid solution [1]. It is strong for attached flows and is still suitable for mild separation. On the other hand it has significant deficits regarding flows with massive separation, adverse pressure gradients and high local stream line curvatures [9].

2.7 Computational Fluid Dynamics

The term *Computational Fluid Dynamics* (CFD) refers to the numerical treatment of flow problems, as well as their solution and analysis. Therefore, the underlying governing equations are spatially and temporally discretised and numerically solved, using mathematical approximation schemes. The result is typically a field solution, providing all flow quantities at every discretisation point of the flow field.

2.7.1 Computational Domain

When using a finite-volume scheme, the physical domain needs to be divided into volume cells. The entity of the cells is then the computational domain. The subdivision can be performed either using a structured or an unstructured grid. The unstructured grid generation is more suitable for complex model geometries but in contrast requires a larger amount of cells and is therefore numerically more expensive [2]. Since it will be used in the framework of this project, we will concentrate on three-dimensional hybrid unstructured meshes. An unstructured hybrid mesh is a grid containing different geometries that are arranged irregularly. It is composed of:

- **Prismatic cells**, which are placed near walls and should particularly resolve the boundary layer.
- **Hexahedral cells**, which are used analogously. However, hexahedra are preferable to prisms, if the different coordinate directions are on different length scales [9].
- **Tetrahedral cells**, which are positioned beyond the prism layers.
- **Pyramidal cells**, acting as connectors between the different cell types [9].

The grid generation is a crucial part of the numeric treatment of flow problems since it has a major impact on the quality and accuracy of the solution [1].

2.7.2 Flow Solver

Now, the *Navier-Stokes equations* (Eq. 2.1 - Eq. 2.3), respectively the RANS equations (Eq. 2.23), here given in the integral form

$$\frac{\partial}{\partial t}\iiint\limits_{\Omega}\vec{W}\,d\Omega+\iint\limits_{\partial\Omega}\overline{\overline{F}}\cdot\vec{n}\,dS=0, \tag{2.30}$$

with vector $\vec{W}$, containing the conservative variables, and the flux density vector $\vec{F} = \overline{\overline{F}} \cdot \vec{n}$ can be spatially discretised. Detailed information on Equation 2.30 can be found in appendix A.2.

Spatial Discretisation

In order to discretise the governing equations, the conservative variables $\vec{W}$ are assumed to be constant inside a control volume and depend on the sum of all fluxes over the boundaries of the cell S_i [1]

$$\frac{d}{dt}\vec{W} = -\frac{1}{\Omega}\sum_{i=1}^{n}\vec{F}_i S_i \tag{2.31}$$

Furthermore, the fluxes across the boundaries need to be determined. There are multiple schemes to describe the fluxes. Within this work we will deal with the central discretisation schemes.

Central Scheme with Artificial Dissipation

If the central discretisation scheme is used, the convective fluxes over a surface can be approximated in relation to the arithmetic average of the conservative variables in the the two adjacent control volumes, connected by the face [1]. Figure 2.7 shows two control volumes around the points P_i and P_{i+1} and their common face $S_{i,i+1}$. This is a discretisation of the cell vertex dual metric type which is employed within this work.

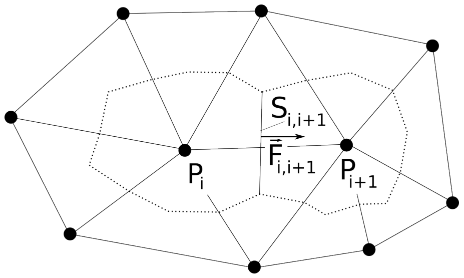

Figure 2.7: Control volumes according to the cell vertex dual metric type (based on [9])

Thereby, the flow variables are assigned to the vertices of the basic grid and the control volumes are formed by connecting the geometric centers of the associated grid cells and the midpoints of the edges. This way, the control volumes do not overlap [1].

Using the central scheme, we can now approximate the convective flux over the surface $S_{i,i+1}$ as the convective flux due to the mean flow variables at the surface [1]:

$$\begin{aligned}\left(\vec{F}_c S\right)_{i,i+1} &= \frac{1}{2}\left(\vec{F}_{c,r} + \vec{F}_{c,l}\right)_{i,i+1} S_{i,i+1} - D_{i,i+1} \\ &= \frac{1}{2}\left(\vec{F}_c(\vec{W}_i) + \vec{F}_c(\vec{W}_{i+1})\right) S_{i,i+1} - D_{i,i+1}\end{aligned} \tag{2.32}$$

The term $D_{i,i+1}$ represents artificial dissipation, which is added for reasons of stability. It is similar to the viscous terms in the governing equations and is given by [9]

$$D_{i,i+1} = \frac{1}{2}\widetilde{\alpha}\left[\epsilon^{(2)}_{i,i+1}\left(\vec{W}_i - \vec{W}_{i+1}\right) - \epsilon^{(4)}_{i,i+1}\left(\triangle\vec{W}_i - \triangle\vec{W}_{i+1}\right)\right]. \tag{2.33}$$

As can be seen, it consists of second- and fourth-order differences, that can be controlled by the coefficients $\epsilon^{(2)}_{i,i+1}$ and $\epsilon^{(4)}_{i,i+1}$, which are dependent on a pressure sensor function. The fourth-order differences suppress odd-even-decoupling that would occur and are therefore mainly used in the domain. However, the fourth-order differences can lead to oscillations at discontinuities. In order to minimise these oscillations, the second-order differences are activated there [1]. The dissipation term $\widetilde{\alpha}$ depends on the characteristics of the flow field and can either be dimensioned using the highest eigenvalue inside a cell (scalar dissipation scheme) or by using a matrix (matrix dissipation scheme) [1].

Temporal Discretisation

In addition to the spatial discretisation Equation 2.31 needs to be discretised and integrated in time until the steady-state solution is reached. In case of explicit time-stepping schemes, the maximum time step is limited according to the CFL (*Courant-Friedrichs-Lewy*) condition, which signifies that the physical domain of dependency is completely contained in the numerical domain [1].

Multigrid

The multigrid process is an acceleration technique that can be used to achieve a faster convergence to the steady-state solution. Hereby, the initial grid is coarsened by joining cells of the initial grid. Due to the coarser grid, the time step can be increased and therefore the computing time decreases. Additionally, the convergence is accelerated because the low-frequency error at the beginning of the computation is damped more effectively [1]. There are multiple cycles that can be passed using the multigrid technique, in which the grid is coarsend and refined stepwise to minimise the computing time and effort [1].

2.7.3 The DLR TAU-Code

The DLR TAU-Code is a flow solver developed and maintained by the DLR-Institute of Aerodynamics and Flow Technology Göttingen and Braunschweig [9]. It is an unstructured finite volume flow solver for the RANS equation, employing the cell vertex dual metric scheme. It has various types of spatial discretisation schemes, containing central and upwind schemes, implemented, disposes of explicit and implicit time stepping schemes and supports convergence acceleration techniques. Turbulence can be modelled within the DLR TAU-Code using first or second order turbulence models. The DLR TAU-Code is used within the framework of this project to perform the calculations [9].

3 Aircraft Model

In the context of this project, the nacelle strake parameter study is performed for the generic aircraft configuration of the collaborative research project SFB (*Sonderforschungsbereich*) 880 (see chapter 1). This high wing aircraft is illustrated in Figure 3.1. It is equipped with two turboprop engines and an active high-lift system, deploying an adaptive droop nose and an active coanda flap. In addition, the aileron is also internally blown. Therefore, a plenum is integrated along 75% of the chord c, which is subdivided spanwise into six sections that can be controlled independently. This way the blowing coefficient can be adjusted locally and the efficiency can be increased [14].

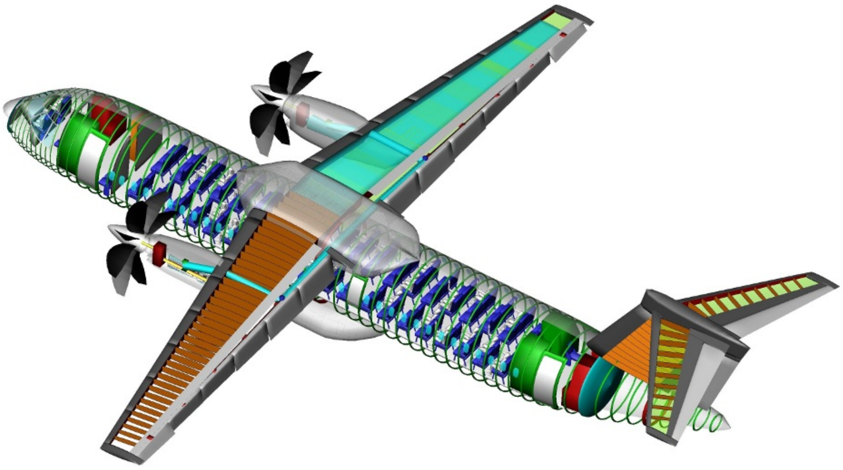

Figure 3.1: Conceptual figure of the reference aircraft of the SFB 880 [11]

Furthermore, the airfoil profile of the wing is based on the DLR F15 airfoil. This airfoil has been developed by the German Aerospace Center for high-lift investigations and has therefore been examined and modified in multiple test campaigns also with regards to active flow control techniques [28]. Thereby, the relative thickness varies from the wing root to the wing tip. Further information on the concept of the SFB 880 aircraft can be found in [27]

Within this work the turboprop geometry, especially the area of the engine integration as well as the wing in the nacelle wake region, are of particular interest. The general geometric parameters of the wing are summarised in Table 3.1. The geometry of both the nacelle and the rotor is depicted in Figure 3.2. As can be seen from 3.2(c), with a length of about $4\ m$ the nacelle is relatively large compared to the mean aerodynamic chord. In addition, it has a rather squarish form. Therefore, the lift generated by the nacelle at high angles of attack is supposed to be higher than in case of conical nacelles. As a consequence, strong vortices are shed by the nacelle, which interact with the flow field and weaken the boundary layer in the wing area. This fact suggests that the negative engine integration interference effects are strong in our case and the necessity of strakes becomes clear. Since a numerical simulation is always linked with a high computational effort, the underlying geometry in this work is simplified in order to improve the efficiency. First of all, a half model is used. Given that the problem is symmetric in this parameter study, the impact of this simplification on the significance of the results is assumed to be neglible. In addition, the tailplane is not considered to further minimise the amount of nodes of the grid. The tailplane of this configuration is arranged downstream of the main wing. Hence, its influence on the flow field around the wing can be assumed to be small. The CAD models are shown in Figure 3.3 and 3.5. The adaption of the CAD models, particularly the strake parameter changes are realised with the commercial software CATIA [7]. The two configurations of the SFB 880 aircraft that are needed within this project are described in the following.

Wing area S	$95\ m^2$
Mean chord $\overline{c}$	$3.428\ m$
Wing span b	$28.775\ m$
Aspect ratio Λ	8.716
Dihedral ϑ	-2°
Leading edge sweep φ	10°
Basic airfoil section	DLR F15

Table 3.1: Geometric parameters of the reference aircraft's wing [14]

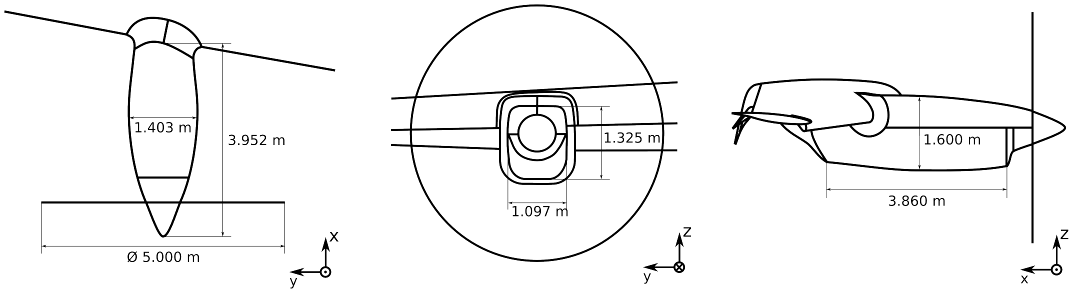

(a) Top view (b) Front view (c) Side view

Figure 3.2: Geometry and dimensions of the turboprop engine

3.1 Landing Configuration

The simplified model of version REF2-2013 of the SFB 880 aircraft in the landing configuration is illustrated in Figure 3.3. On the basis of this configuration the nacelle strake parameter study will be performed. In this configuration the flap deflection angle is $\delta_f = 65°$. It is simplified as a single panel which is shown in 3.3(b). The aileron is also used to generate lift and is deflected by $\delta_a = 45°$ [14]. Furthermore, the droop nose is drooped by $\delta_{dn} = 30°$ [4]. As can be seen in 3.3(a), no gap has been modelled at the droop nose-nacelle-intersection. This simplification is made under the assumption that the engine interference effect is mainly driven by the nacelle vortices and that due to the comparatively small gap because of the close integration of the turboprop, no vortices are shed at the junction (see also subsection 2.5.2). Figure 3.4 shows an airfoil section of the wing, outboard of the nacelle. It also provides a detailed view of slot and contains its relative dimensions. The trailing edge has a thickness of $0.35 \cdot 10^{-3}$ of the local chord and the blowing slot has a height of $0.6 \cdot 10^{-3}c$.

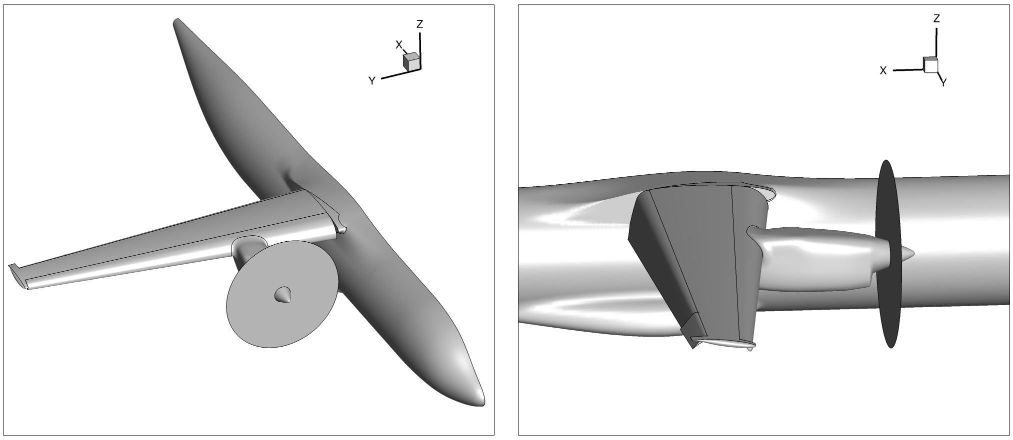

(a) View of the complete aircraft model (b) View of the wing

Figure 3.3: Simplified model of landing configuration of the SFB 880 aircraft

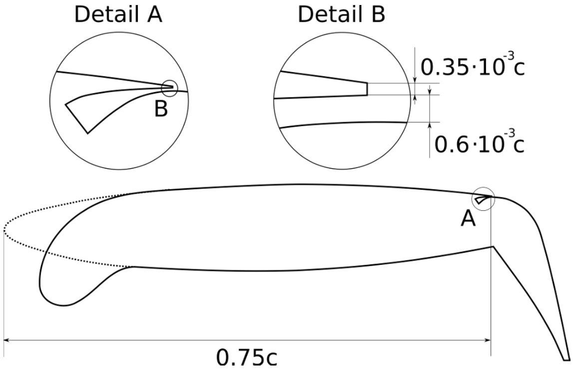

Figure 3.4: Airfoil section and detailed view of the slot

3.2 Cruise Configuration

Following the parameter study, the strake influence on drag in the cruise flight will be determined. Therefore, the cruise configuration model of the underlying aircraft is needed. Figure 3.5 shows the model, again without tailplane, that will be used for this simulation. Flap and aileron as well as the adaptive droop nose are in the retracted position and active blowing is turned off. It should be noted that the rotor is modelled as a thin actuator disc to which boundary conditions will be assigned.

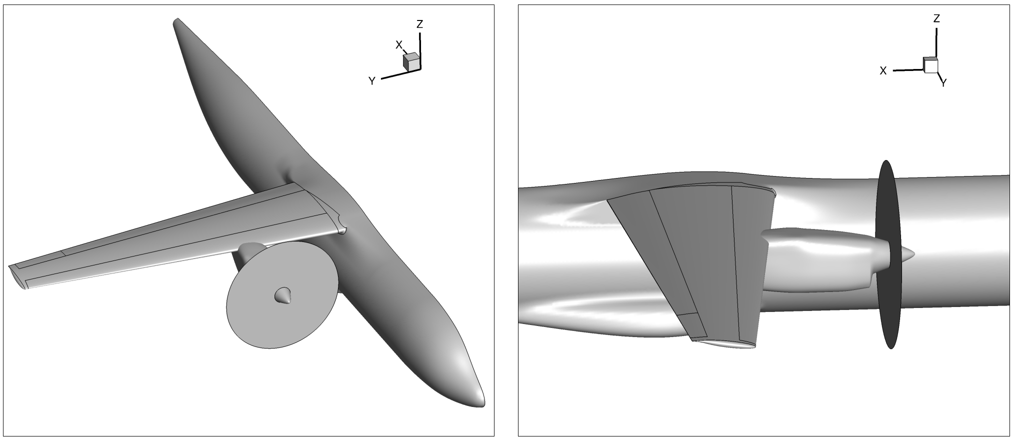

(a) View of the complete aircraft model (b) View of the wing

Figure 3.5: Simplified model of cruise configuration of the SFB 880 aircraft

4 Grid Generation Process

Within the scope of this chapter the grid generation process for the landing configuration (section 3.1) will be described. The mixed hybrid grid is generated with the commercial software CENTAUR, Version 10.5.0.2 [5] which is a largely automated unstructured grid generation program. The grid generation is processed on the basis of CAD geometry models. It can be globally controlled using basic parameters and locally adapted by means of sources. The grid generation is then performed in three consecutive stages, namely the surface grid generation, the generation of prisms and hexahedra and the final tetrahedral grid generation.

In foregoing investigations an unstructured hybrid grid has already been generated for this configuration. Within these investigations a grid convergence study has been performed for the wing-fuselage configuration with a deflected aileron and deflected flaps but a clean nose. This grid is now modified in this work. Since structured elements are considered as favourable for the simulation of vortices [8], these modifications include particularly the insertion of structured hexahedron sections into the wing area inside the wake of the nacelle. However, the utilised version of CENTAUR only supports the generation of structured elements that are linked to panels containing exactly four boundary curves. Therefore, several panels of the geometry model first need to be repartioned. Subsequently, the grid parameters and sources are defined based on the initial grid, which has been extensively examined. The fuselage section is not modified and is therefore not further specified in the following.

4.1 Modular Grid Generation

In the context of a parameter study, many simulations need to be performed, resulting in a high number of grids. Taking into account the high complexity of the present aircraft configuration, it becomes obvious that a complete grid generation process for every strake parameter variation would lead to a considerable expenditure of time. Apart from that, the grid has a non-neglible impact on the results of a numerical simulation [2] and is therefore a very crucial part of the simulation with respect to the significance of the results. Therefore, the modular grid generation approach is used within this project in order to realise the grid changes. Thereby, the geometry is subdivided into different zones, each containing a different module. The grid is then generated for the entity of zones. Changes in geometry can consequently be performed by replacing single modules. The basic grid of the unchanged zones is mainly reused while the new grid inside the modified zone is then rebuilt by means of the basic grid. This way, the effort in computing time for the complete grid generation can be reduced to a mimimum. Furthermore, the main grid of different cases is identical. Hence, differences in the numerical solution are likely to be caused by the changes in geometry and are independent of the grid in the other zones. Figure 4.1 depicts the geometry of the module box used in this work. It should be noted that the design of the module box requires some basic rules in order to allow for a smooth transition between the zones. First of all, the module box edges should be aligned normal to the surface in order to avoid skewness of the cells and chopping at the zone boundaries. Secondly, the module box needs to be dimensioned in such a way that there is enough space between the geometry changes and the module box boundaries for the cells to grow within an adequate stretching ratio. Finally, the basic grid should be generated with the most critical module box geometry. In the case of a nacelle strake variation in position, this signifies that the basic grid should be generated with the strake that is nearest to the wing-sided boundary.

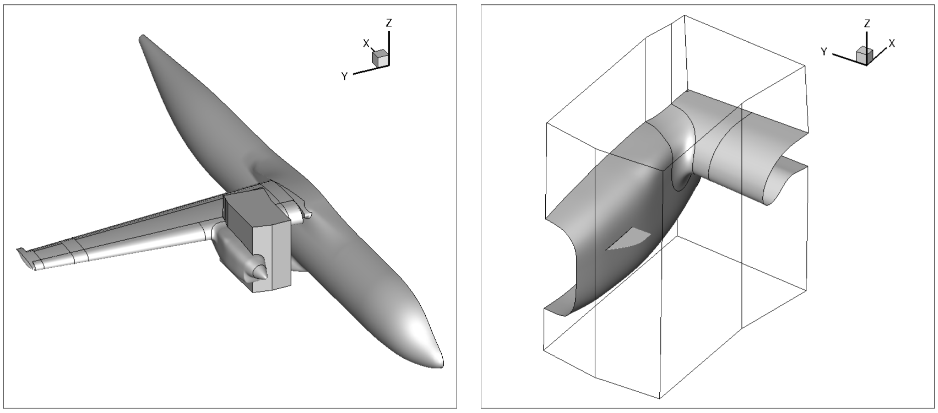

(a) Position of the module box (b) Detailed view of the module box

Figure 4.1: Geometry of the module box

4.1.1 Main Zone

The first step of the grid generation process is the repartition of panels because CENTAUR only supports the generation of structured elements that are linked to panels containing exactly four boundary curves. Therefore, the main wing is initially subdivided spanwise into several sections. Thereby, it needs to be ensured that geometry edges are faced with unstructured elements, so that the grid elements can contract both in span and in streamwise direction. Figure 4.2, showing the surface grid of the main zone, illustrates this subdivision. Section 1 near the wing tip is the first section containing structured elements. Section 2 is an interface zone, containing unstructured elements. The reason is the complex geometry at the trailing edge between aileron and flap. Section 3 is the most important section, for it contains the wake region of nacelle and strake. It is mainly composed of structured cells. Due to the engine integration the panels in section 4 cannot be equipped with structured elements near the leading edge. Therefore, the grid at droop nose and nacelle are unstructured in this region.

Finally, the wing root in section 5 is unstructured for the same reasons. In order to further clarify the construction of structured element sections, 4.3(a) depicts the surface grid of Detail A, which is the transition between the structured hexahedral and unstructured prismatic sections at the aileron-flap-interface. As can be seen, the panel of the structured section is once again divided in streamwise direction. The interpanel, which is adjacent to the wing's trailing edge, is composed of unstructured prismatic elements. This way it can be ensured that the cells can contract from the structured panel to the very small size of the cells at the trailing edge and the slot. The regions of transition between structured and unstructured elements are very crucial with respect to numerical dissipation. Therefore, the interpanel needs to be well dimensioned so that an adequate stretching rate is ensured. The structured cells are designed to have a value of anisotropy of $3 - 4$, which is not suitable for unstructured prismatic cells. In order to prevent high anisotropy unstructured cells at the panel boundaries, the structured cells are contracted locally by means of a source. This way a smooth transition between the different type of cells can be achieved. The particular surface

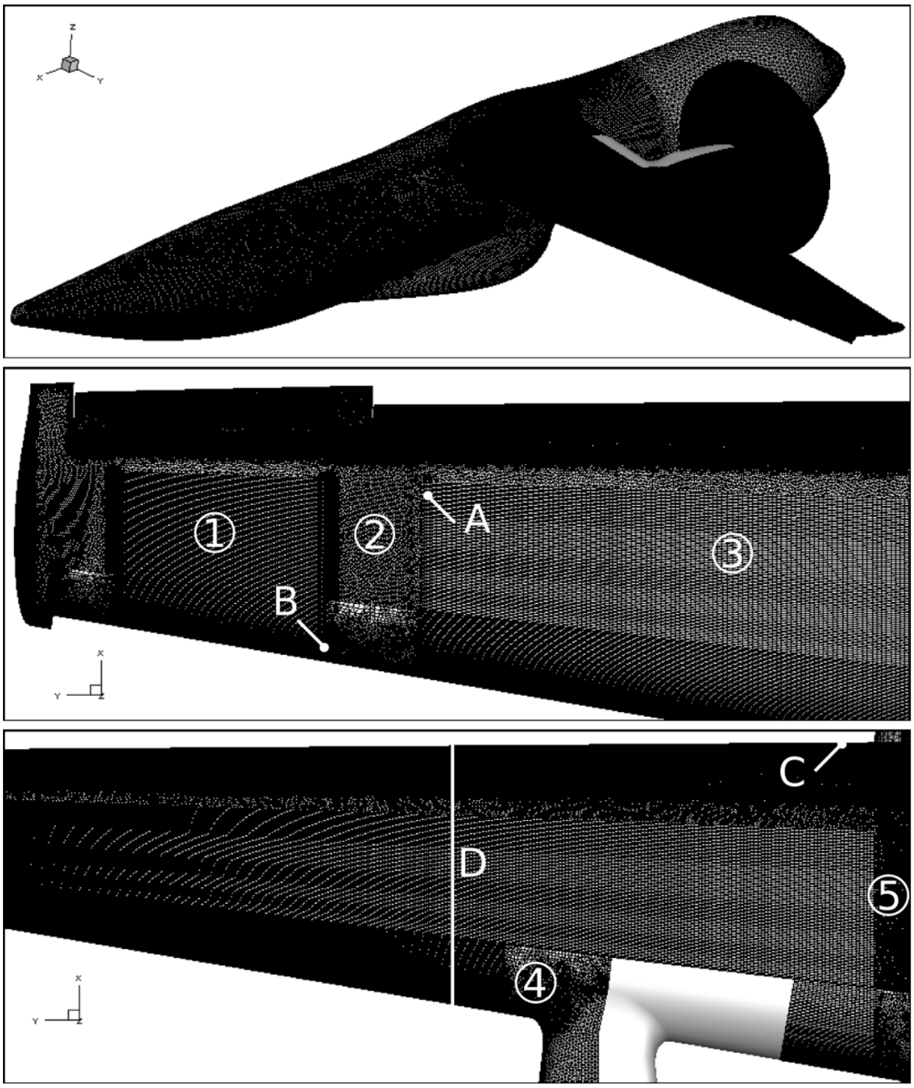

Figure 4.2: Surface grid, top: main zone, middle: wing tip, bottom: wing root

grid topology in the structured droop nose region is represented by Detail B, which is depicted in 4.3(b). On grounds of the high flow velocities and the resulting high gradients around the droop nose, the anisotropy of structured cells near the leading edge is further increased. Due to the nature of structured cells, it is not possible to increase the spanwise contraction of the cells at the droop nose panel boundary without influencing those of the main wing panel. Therefore, unstructured hexahedras are used on the adjacent panels instead of prismatic cells. These are more suitable for the passage to high anisotropy structured cells. Within the prismatic and hexahedral grid generation step, some of the unstructured hexahedra are divided in half by CENTAUR in order to respect the thicknesses of the initial prism layer. However, this is a circumstance that cannot be regulated in the version of CENTAUR used in this project. It can only be reduced by anticipation during the surface grid setup. Since this is not always possible, some cells that are divided this way can be found in the present grid. For the sake of completeness, 4.3(c) shows Detail C, which signifies the flap region near the wing root. In analogy to the structured main wing and droop nose panels, the structured hexahedral panel on the flap is separated both from the flap's trailing edge and the very finely resolved slot region by unstructured prismatic interpanels. As can be seen in 4.3(c), structured elements can also be divided in half during the prismatic grid generation. However this happens very rarely, and within the present grid it is furthermore ensured, that no division has taken place in the strake wake region on the upper side of the wing. The aileron is set up in the same manner.

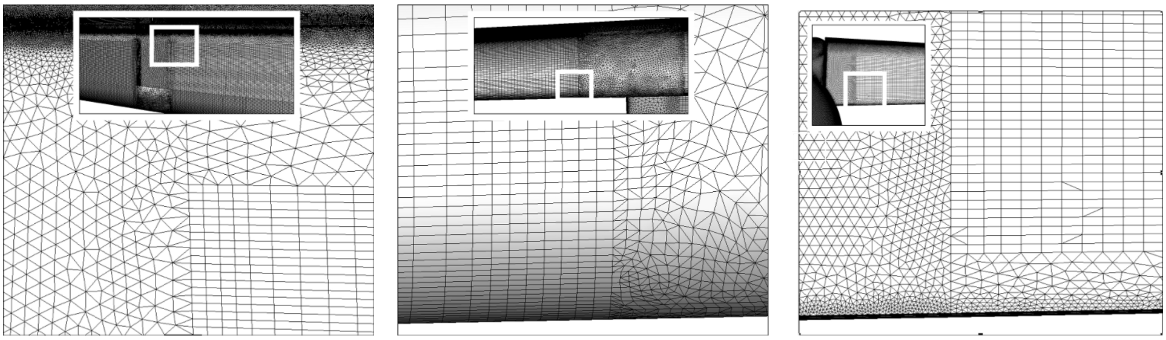
(a) Detail A: Main wing (b) Detail B: Droop nose (c) Detail C: Flap

Figure 4.3: Transition between structured and unstructured surface sections

For a proper resolution of the boundary layer the prismatic and hexahedral layers need to be well defined. Therefore, the boundary layer thicknesses of the aircraft elements are approximated by means of the actual local Reynolds numbers, estimated with the flat-plate law. In order to resolve the viscous sub-layer, the initial prism layer thickness, here denoted as y must be sufficiently small. Hence, it is approximated in such a manner that an overall dimensionless first wall distance, defined as [20]

$$y^+ = \frac{y}{\delta} = \frac{y}{\nu}\sqrt{\frac{\tau_W}{\rho}}, \tag{4.1}$$

of $y^+ < 1$ is ensured. In addition, the complete boundary layer needs to be covered by the prismatic grid. Thus, the number of prism layers need to be defined, depending on the local estimated boundary layer thickness. 4.4(a) depicts the prism layer distribution of an airfoil section on the basis of Cut D, shown in Figure 4.2. For the main wing and the droop nose 37 layers are basically used while the flap and aileron grid is composed of 40 layers due to the higher local Reynolds number and in order to capture the wake of the main wing. However, in regions of complex geometry, the amount of layers cannot always be realised. Therefore, CENTAUR disposes of two basic approaches to deviate in particular regions from the general settings. First, the prism stretching can be reduced, resulting in smaller prism layers. This is the case in the concave wall region of the wing-flap interface as can be seen in 4.4(a). The region inside the plenum and around the slot, illustrated in 4.4(b), is even more critical. Due to the very fine geometry, the reduction of the prism thicknesses is not sufficient. Therefore, the prism layers are chopped down to a minimum amount of 13 layers near the wing's trailing edge. On the flap, the layers then grow rapidly up to the default amount of 40 layers. This way, a sufficient distance between the upper and lower prism grid inside the plenum is provided, which ensures that there are tetrahedral cells inside the slot. The prism grid inside the plenum is composed of about 20 to 22 layers.

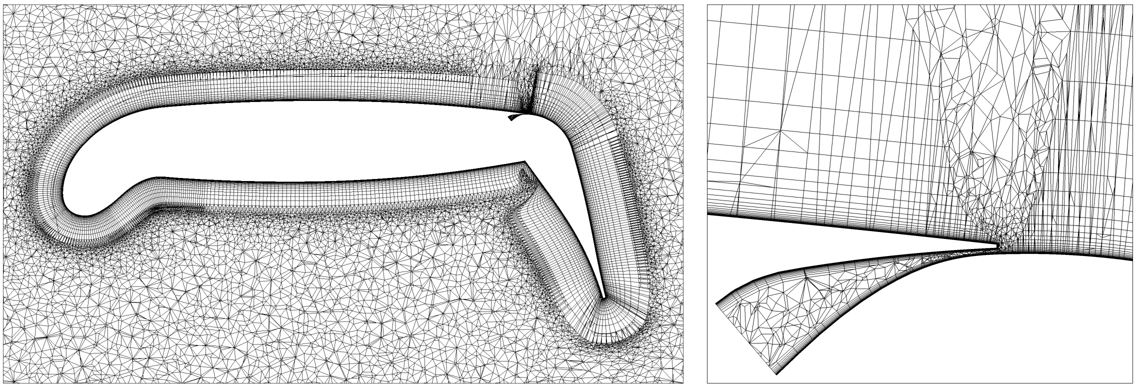

(a) Cut D: Prism grid of airfoil section (b) Prism grid in slot region

Figure 4.4: Airfoil section cut showing prism layers

Since the wake of nacelle and strake on the main wing is of particular interest for this parameter study, a hexahedral block is placed into this region. The hexahedral block, which is shown in Figure 4.5, is linked to the main wing panels inboard of the nacelle's symmetry plane. It is a block containing structured hexahedral elements that are placed on top of the hexahedral layers in that region. The grid within the block is vertically discretised in 36 layers and thus increases the grid resolution of the area that the vortices are supposed to propagate through. Since it can only be linked to structured panels, it covers only the front section of the wing and ends at the interpanel, as becomes clear when we look at 4.5(a). 4.5(b) shows the cutaway view of the hexahedral block on the left-hand side. In addition, it depicts the boundaries of the module box on the right-hand side. Within the modular grid generation the tetrahedral elements at the module box boundaries need to be attached to tetrahedral elements of the main zone. Therefore, CENTAUR does not support the linking of the hexahedral block with the module box boundary panel. Nevertheless, tapering of the block in vertical direction, as illustrated in the figure, can remedy this.

A multitude of sources is deployed on grounds of the aircraft's geometry and with the aim to provide a smooth cell transition at edges and boundaries. Moreover, some geometrical sources are placed into the main zone to account for the expected flow phenomena. Hereby, the grid is locally refined in the regions containing the inboard and outboard nacelle vortices, as well as in the regions of the clean edge vortices of wing tip and root. However, these sources are not presented here. In subsection 4.1.2, the geometric source accounting for the strake vortex will be exemplarily discussed. To conclude, the main grid, excluding the module box, contains about 45 million nodes.

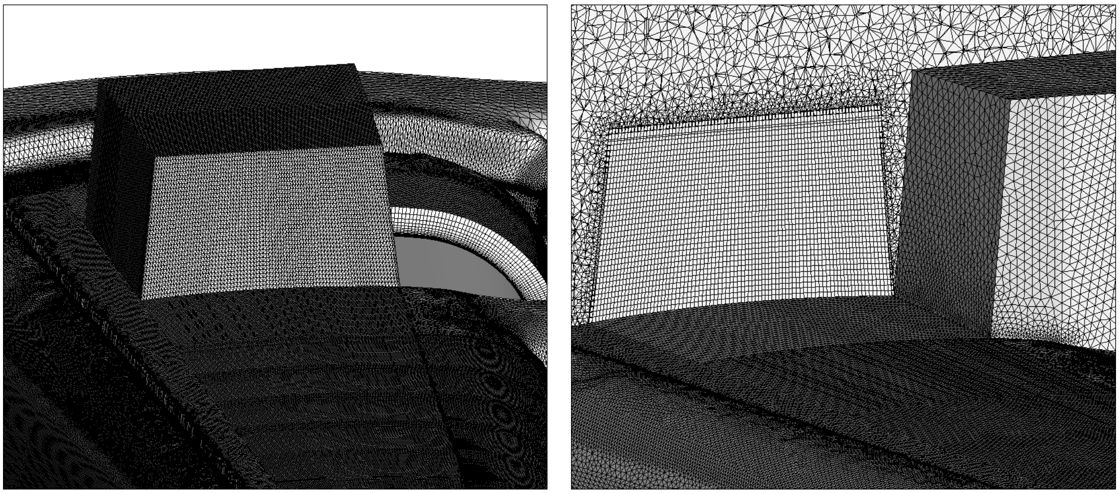

(a) Geometry of the hexahedral block (b) Cutaway view of the hexahedral block

Figure 4.5: Structured hexahedral block in the strake wake section of the wing

Node points	$45.4 \cdot 10^6$
Grid cells	$143.0 \cdot 10^6$
Surface elements	$2.1 \cdot 10^6$
Hexahedra, prisms and pyramids	$52.7 \cdot 10^6$
Tetrahedra	$90.3 \cdot 10^6$

Table 4.1: Grid statistics of the main zone

It is composed of about 140 million cells, among them about 90 million tetrahedral and 50 million prismatic cells. Table 4.1 summarises the grid statistics for the main zone.

4.1.2 Module Box Zone

The second step to obtain the final grid is the grid generation for the module box. Figure 4.6 shows the surface grid and the prism layers of the underlying geometry inside the zone, containing the initial strake version the following nacelle strake parameter study is based on. As already pointed out in section 4.1, the grid of the main zone should be generated with the most critical module box configuration with respect to the geometry. Therefore, the intial grid generation has been carried out with a strake that is positioned $1\ m$ downstream of the present strake and $0.2\ m$ above. In doing so, it is ensured that the grid is constructed in such a manner that a wide range of parameter variations can be investigated.

For reasons of better resolution of the strake vortex, the module box contains the curved tube source, represented in 4.6(a). It starts at the leading edge of the strake, passes the droop nose-nacelle intersection and forms a path downstream along which the strake vortex is supposed to propagate. In doing so, the local relative surface and tetrahedral element sizes are reduced to 16.7% at the first point and to 50% at the last point of the corresponding cell sizes of the direct environment. 4.6(b) illustrates this refinement on the basis of the prism grid. Within the strake parameter study the grid inside the module box zone will constantly be regenerated in order to respect the strake geometry changes. Thereby, the geometry of the strake source also needs to be adapted with respect to the strake parameter changes. The basic strake grid of the module box contains slightly more than a million node points and is composed of about 3 million elements, as can be seen from Table 4.2.

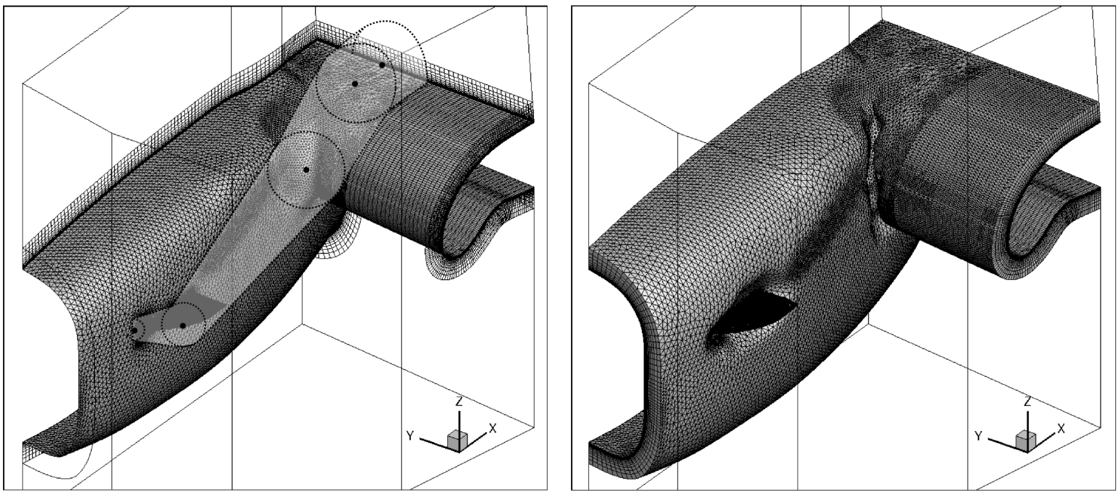

(a) Surface grid and strake source (b) Prism grid

Figure 4.6: Grid of the module box zone

Node points	$1.2 \cdot 10^6$
Grid cells	$3.1 \cdot 10^6$
Surface elements	$0.1 \cdot 10^6$
Hexahedra, prisms and pyramids	$1.7 \cdot 10^6$
Tetrahedra	$1.3 \cdot 10^6$

Table 4.2: Grid statistics of the module box zone

4.2 Qualitative Evaluation of the Grid

As already mentioned at the beginning of this chapter, the grid can have a significant influence on the results of a numerical simulation. For this purpose, grid convergence studies ought to be carried out. Thereby, the overall grid is refined at least three times. On the basis of the numerical results obtained for these grids, the aerodynamic coefficients for a hypothetical grid with infinitesimal small cell sizes can be extrapolated [2]. However, due to the high complexity of the present aircraft configuration, a complete grid convergence study will not be performed within this project. The grid generation process, especially in combination with the deployment of structured elements, has turned out to be a very time-consuming procedure. The main reason was, that compromises between grid structures, desired for the flow resolution and grid structures, necessary for CENTAUR to succesfully generate the grid, had to be made. Therefore, it is not possible to perform a complete grid convergence study with a reasonable effort.

Nevertheless, the present grid shall be evaluated on a qualitative basis. The resolution of the strake and nacelle vortices is of highest importance in our case. For this reason, the grid inside the region containing the vortex paths shall be refined locally. This includes the panels of nacelle, strake and flap as well as some of the wing panels. Subsequently, the solutions, obtained with the different grid finenesses, are regarded in the modified area and analysed with respect to the flow conditions. Thereby, the configuration with the initial strake, namely configuration 11-6S2, is taken as a basis.

In order to refine the grid in the region, the surface elements are approximately halved. In case of the structured elements this can only be done by a bisection of the cell's spanwise length without influencing the grid in the other regions. As a result, the cell's aspect ratio is reduced. The unstructured surface cells can simply be adapted by a modification of the corresponding sources, preserving their aspect ratio. The refined grid is shown by Figure B.2 in the appendix. For comparison, Figure B.1 depicts the actual grid. In order to reduce the effort, the prism layers are not modified. A reduction of the prism layer thicknesses and therefore an accompanied augmentation of the amount of prism layers could only be conducted for the complete wing. The reduction of the prism cell sizes thus only results from the refinement of the surface grid. As a consequence, the cells of the outer prism layers have a high height-width ratio. This circumstance is illustrated on Figure B.4 in the appendix, which shows a cut normal to the streamwise direction at $x = 14.0\ m$. As can be seen, the ratio is clearly smaller in case of the coarser grid, shown by Figure B.3. In addition, the vertical discretisation in the nacelle wake area outside the prism grid, controlled by the hexahedral block, is halved, which is also depicted by the figure. Finally, the tetrahedral element sizes are also reduced by around 50%.

The resulting lift curves for the configuration with the initial strake, calculated on the basic and on the refined grid, are depicted by Figure 4.7. In the first instance, we observe that the grid refinement indeed has a significant impact on the lift curve. As shown, the maximum lift coefficient is reduced by $\Delta C_L \approx 0.035$ for the refined grid. It can be seen that the difference in C_L increases along with the angle of attack. At $\alpha = 6°$, the discrepancy of both lift curves is still small while lift obtained on the refined grid declines more rapidly at post-stall angles of attack. This fact suggests that the vortices are less dissipated on the refined grid, leading to a stronger reduction of lift than on the basic grid. However, as can be seen, α_{max} is identical for both grids.

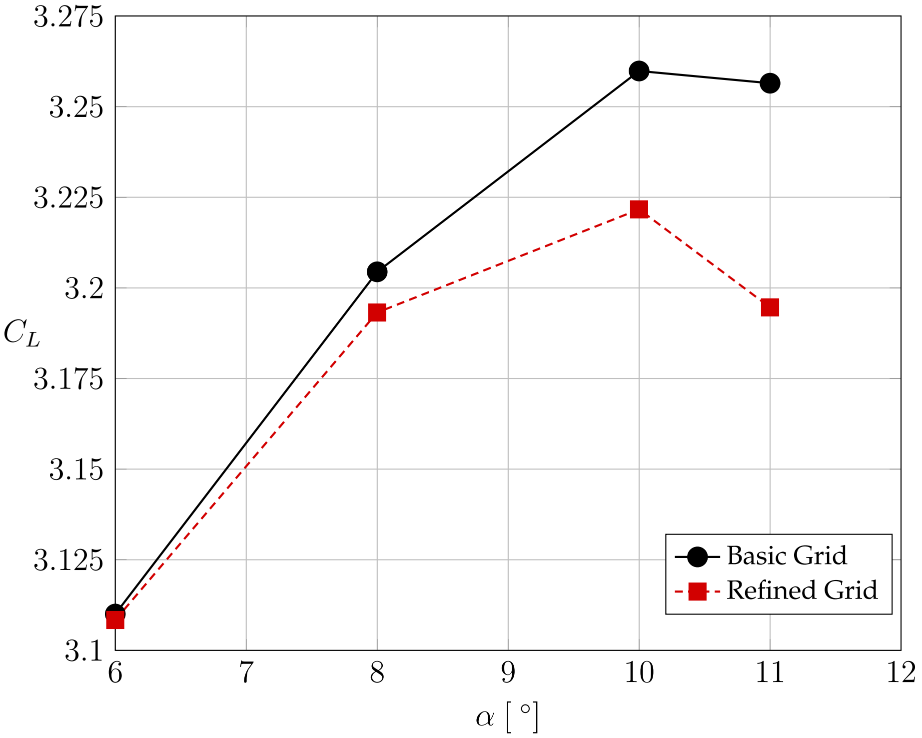

Figure 4.7: Influence of grid refinement on the lift curve

Fur a further understanding of the differences, the distribution of suction peaks on the flap are depicted by Figure 4.8 for $\alpha = 6°$ and $\alpha = 10°$. At $\alpha = 6°$, shown by 4.8(a), the nacelle vortex can be found at around 25% of the semispan while the the

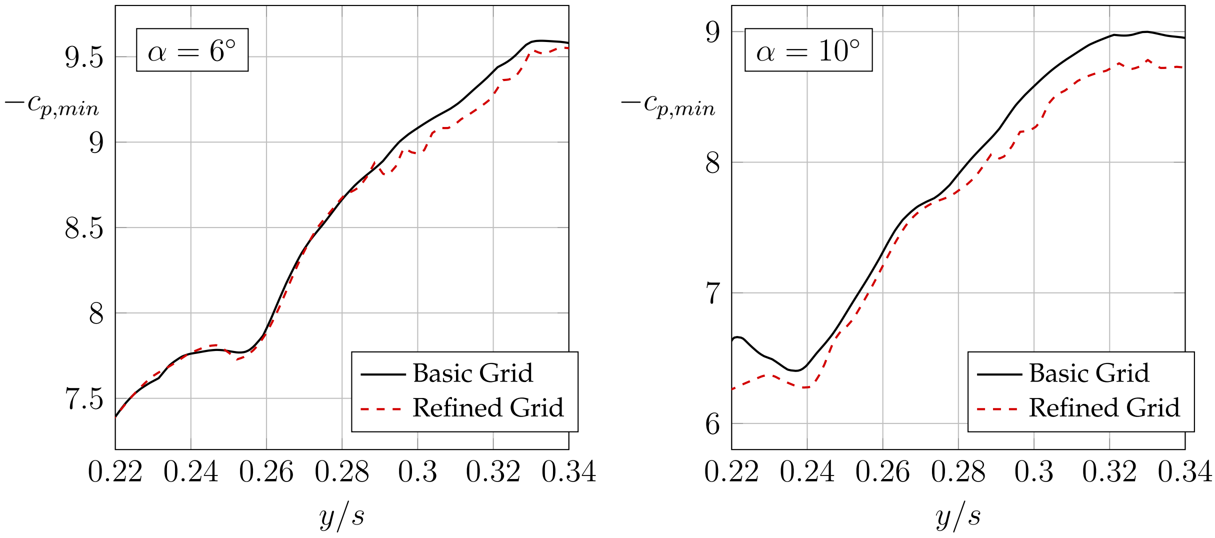

(a) $\mathbf{c_{p,min}}$-distribution at $\boldsymbol{\alpha} = \mathbf{6}°$

(b) $\mathbf{c_{p,min}}$-distribution at $\boldsymbol{\alpha} = \mathbf{10}°$

Figure 4.8: Different suction peak distributions on the flap due to grid refinement

strake vortex is located at $y/s \approx 0.27$. Two effects can be observed here. Firstly, the nacelle vortex is more distinct in case of the refined grid, which is indicated by the more distinct wave-like pattern. Secondly, the strake vortex seems to be stronger, leading to a higher downwash on the right-hand side, resulting in lower suction peaks. As shown by 4.8(b), the differences of the suction peak distributions are more substantial. This applies particularly to the nacelle vortex. Due to the higher deflection at $\alpha = 10°$ it is now located at around 23.5% of the semispan. It can be observed that $c_{p,min}$ is recognisably reduced here compared to the solution on the basic grid which again indicates its higher strength and explains the strong decrease of C_L.

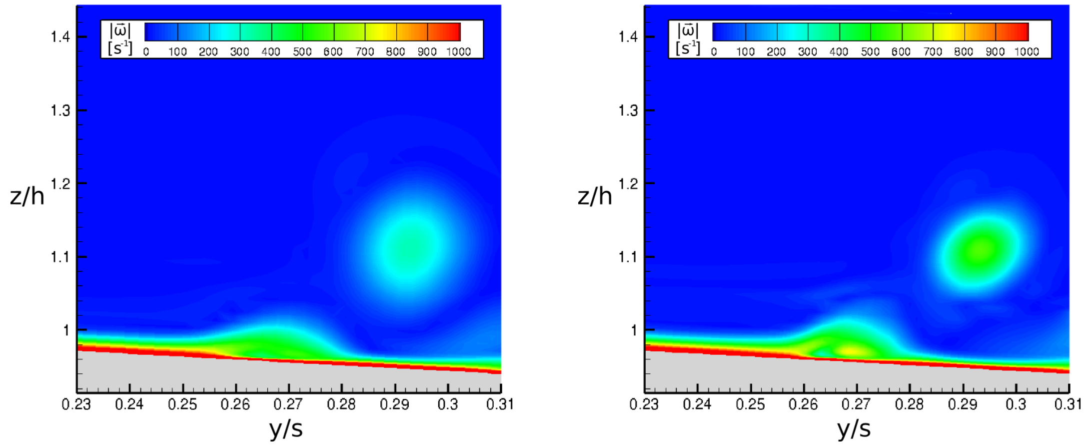

(a) Basic grid at $\boldsymbol{\alpha = 6}°$ (b) Refined grid at $\boldsymbol{\alpha = 6}°$

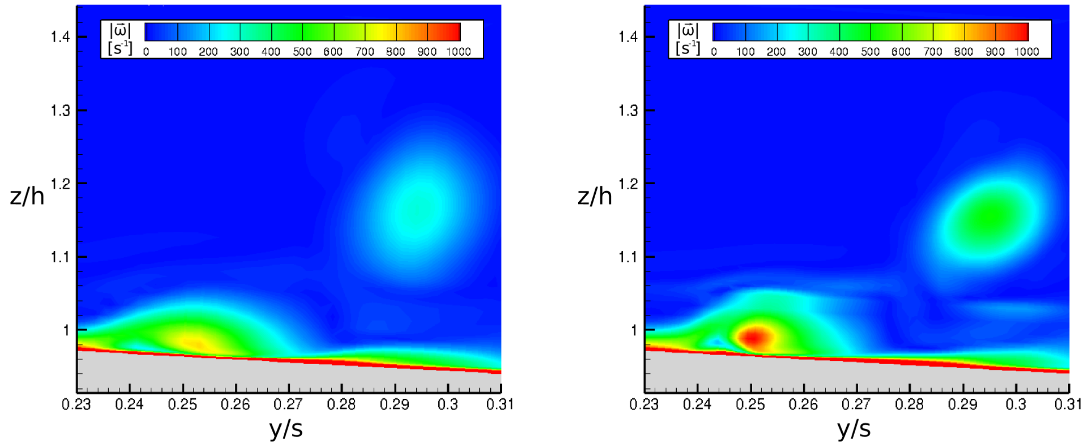

(c) Basic grid at $\boldsymbol{\alpha = 10}°$ (d) Refined grid at $\boldsymbol{\alpha = 10}°$

Figure 4.9: Differences in vortex resolution due to grid refinement, cut at $\mathbf{x = 14.0\ m}$

Finally, Figure 4.9 shows cutting planes for the angles of attack considered before at $x = 14.0\ m$, which signifies a location at about 70% of the wing. An overview of all cutting planes and their positions on the wing is provided by Figure B.7 in the appendix. The cutting planes are coloured by the absolute values of vorticity $|\vec{\omega}|$ and therefore unveil the vortices. In accordance with the foregoing assumptions, it can be seen that the vortices are stronger for the refined grid. This can particularly be observed for the nacelle vortex at $\alpha = 10°$. In addition, the sharper contours of the strake vortex on the refined grid clarify the higher resolution due to the refined grid. However, the upper side of the nacelle vortex at $\alpha = 10°$ is blurred on the refined grid. This is most likely caused by the large height-width ratio of the outer prism cells as explained before. Contrary to the different values of vorticity, the fineness of the cells do not seem to influence the location of the vortex paths.

In summary, the qualitative evaluation of the grid has given some insights into the grid influence on the solution. A grid impact on C_L is existent and increases along with the angle of attack. However, both the characteristic behaviour of the lift curve and the flow phenomena are reproduced correctly in qualitative terms by the coarser grid. The positions of the vortex paths agree on both grids which is the most important condition with respect to the following nacelle strake parameter study. Therefore, we will in the following perform the calculations on the coarser grid which allows for a reduced numerical effort. Nevertheless, it has to be kept in mind, that $C_{L,max}$ of the optimised strake, which will be found within the next chapter, is expected to be overestimated.

5 Nacelle Strake Parameter Study

This chapter centers around the optimisation of the nacelle strake geometry and position in order to obtain a maximum lift coefficient $C_{L,max}$. Therefore, several numerical simulations of the aircraft's landing configuration with different strakes will be carried out. Thereby, we will concentrate on the realisation and optimisation of an inboard strake. Since the present aircraft possesses a backward-swept wing with negative dihedral, the inboard nacelle vortex is supposed to pass closer to the upper wing's surface than the outboard nacelle vortex. Therefore, a higher potential of lift recovery by means of an inboard strake is assumed. This nacelle strake parameter study is based on a pre-study in the context of which two different strakes have been investigated by numerical simulation. The study unfolded that a strake whose trailing edge is placed at about one third of the streamwise length of the nacelle and near the vertical symmetry plane (see Figure 5.7) shows a better performance than a strake that is placed near the droop nose-nacelle-intersection. Hence, within the following parameter study we will start with this more effective strake as the initial strake. The parameters will then be stepwise modified in order to achieve further improvements. However, the configuration without strake will be analysed before the parameter study in order to obtain an understanding of the local flow conditions and the characteristics of the actual nacelle vortices. In addition, the case with the initial strake will be examined.

5.1 Numerical Setup

For the flight conditions of the approach, the atmospheric values of the standard atmosphere at sea level are taken as a basis. The aircraft's Mach number is $Ma = 0.15$ and the Reynolds number amounts about 12 million. The dimensionless momentum coefficient is set to $c_\mu = 0.03$ which represents the *boundary layer control mode* with fully attached flow on the flap at an angle of attack of 6° [13]. Furthermore, in these investigations the case without thrust is examined, so the turbuprop engines are adjusted to negate their own drag. The aircraft's flight conditions are summarised in Table 5.1. All calculations are performed using the DLR TAU-Code (see subsection 2.7.3) on the basis of the same numerical setup which is given in Table 5.2. The convective fluxes are discretised by means of a central scheme with artificial dissipation. A scalar dissipation scheme has been chosen as the central dissipation scheme even though it leads to higher dissipation and is less accurate than the matrix dissipation scheme. However, in consequence of its higher robustness and the faster convergence up to steady-state, it appears to be more suitable to perform a high number of calculations as it is the case within this project. Time stepping is undertaken by an implicit *Backward Euler*

Mach number Ma	0.15	
Reference density ρ_0	1.225	kg/m^3
Reference kinematic viscosity ν_0	$1.4607 \cdot 10^{-5}$	m^2/s
Reference temperature T_0	288.16	K
Reynolds number of incident flow Re_∞	$12 \cdot 10^6$	
Dimensionless momentum coefficient c_μ	0.033	

Table 5.1: Flight conditions during landing

scheme and the initial CFL number is set to 4.0 and is switched to 2.0 in case of high pressure gradients. In order to accelerate the convergenve to steady-state, the multigrid method is used. Therefore, calculations are performed on three grids of different refinement levels within V-cycles. The calculation is furthermore parallelised utilising ten nodes, each containing 24 cores. The *Spalart-Allmaras turbulence model* with rotational and vortical correction is employed within the calculations. The rotor is modelled with an actuator disk whose load is approximated by a radial distribution of force coefficients [14]. The calculations are performed in multiple consecutive steps. First, the solution for $\alpha = 6°$ is determined. Thereby, the multigrid method is primarily used within the first $12\ 000$ iteration steps to obtain a fast damping of the low frequency error. Subsequently, $15\ 000$ iterations on the finest grid are run through in order to minimise the low frequency error and to reach a well-converged solution. Based on

Solver	Unstructured finite volume RANS solver
Convective flux discretisation type	Central scheme
Central dissipation scheme	Scalar dissipation
Time discretisation	*Backward Euler scheme*
Initial CFL number	4.0 / 2.0
Parallelisation	240
Multigrid cycle	V
Multigrid levels	3
Turbulence Model	*Spalart-Allmaras* with rotational correction (SARC)

Table 5.2: Parameters of the numerical simulation

Angle of attack	$\alpha = 6°$		$\alpha = 8°$	$\alpha = 10°$	$\alpha = 11°$	$\alpha = 12°$	$\alpha = 13°$
Grid	Multi	Single	Multi	Multi	Multi	Multi	Multi
Iterations	12 000	15 000	12 000	12 000	12 000	12 000	12 000

Table 5.3: Number of iterations used for flow computation at different angles of attack

the solution at $\alpha = 6°$ further changes of the angle of attack are calculated consecutively. However, as can be seen in Figure 5.1, the final $15\ 000$ iterations, performed to calculate the solution of $\alpha = 6°$, only have a very small influence on the dimensionless parameters. Therefore, solely the $12\ 000$ iterations on the multigrid are used for the further cases of $\alpha = 8°$ up to $\alpha = 13°$. Nevertheless, in a foregoing analysis, the configurations have been analysed and compared at $\alpha = 6°$ before higher angles of attack have been examined. Thus, the final single grid iterations have been performed for all configurations at $\alpha = 6°$.

5.1.1 Convergence Behaviour

In this section the convergence behaviour of the solution shall be discussed. With respect to the high amount of calculations, performed within this project, the convergence behaviour will only be exemplarily shown for the configuration without strake. Figure 5.1 shows the courses of the dimensionless parameters C_L and C_D for this case as well as the normalised density residual ρ_{res}/ρ_0 in time, represented by the iteration steps. Since the focus within the following parameter study will be on the maximisation of $C_{L,max}$, the course of C_L is the relevant criteria in order to decide if the solution is converged. Thereby, the magnitude of the lift coefficient oscillation needs to be in a range of about 1 LC (Lift Count), which denotes a ΔC_L of 0.01. As can be seen from the figure, the initial disturbances decrease fast within the first $5\ 000$ multigrid iterations, which can particularly be observed by the course of ρ_{res}. From there on, the error

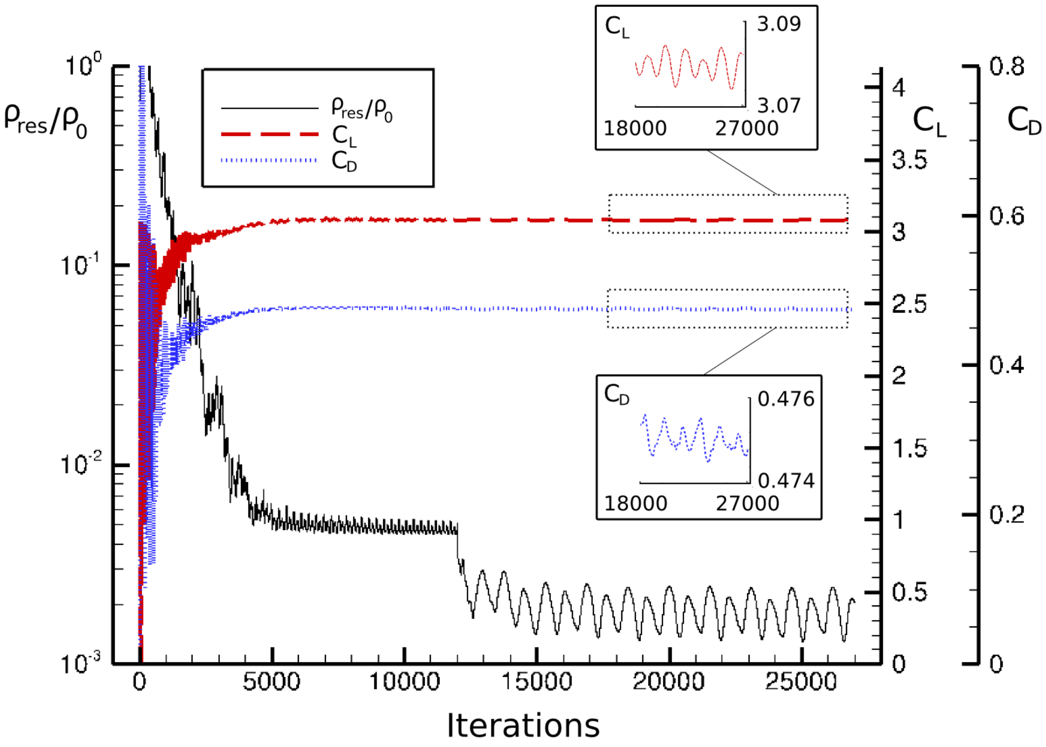

Figure 5.1: Convergence behaviour, simulation at $\alpha = 6°$

decreases slower and at about 7 000 iterations both the dimensionless coefficients and ρ_{res}/ρ_0 seem to oscillate around horizontal asymptotes. Thereby, the drag coefficient variation is in a range of about 10 DC (Drag Counts), where 1DC $\hat{=}$ $\Delta C_D = 10^{-4}$. Here, the density residual has declined to less than 1% of ρ_0. At 12 000 iterations, the single grid is turned on, which results in a further decdrease of the density residual up to an average of about 0.2% of the reference density. However, no significant changes of C_L and C_D can be obtained by the calculation on the finest grid. The two frames in the figure give a detailed view of the dimensionless parameters at the final 9 000 iteration steps. It can be seen that the defined criterium for C_L is fulfilled. Nevertheless, the values oscillate in a repetitive pattern around an average course. This variation of C_L of about $1LC$ is problematic with respect to the goal of this project. Since a maximisation of the maximum lift coefficient $C_{L,max}$ should be achieved, the final optimisation potential lies at a range of a few lift counts. Therefore, the dimensionless parameters are averaged over the last 2 000 iterations steps before different configurations can be compared and evaluated. More information on the nature of these high-frequency variations can be found in Figure B.5 in the appendix, which shows the distribution of Δc_p between a local maximum and a minimum. As can be seen, the oscillations derive from the trailing vortices shed due to the gap between aileron and flap and due to the junction of fuselage and droop nose. After the initial numerical simulation at $\alpha = 6°$, further solutions at higher angles of attack are calculated based on this first solution. Figure 5.2 shows the consecutive calculations up to $\alpha = 13°$. We see that the convergence behaviour is qualitatively similar in the other cases. Indeed, we can see at about

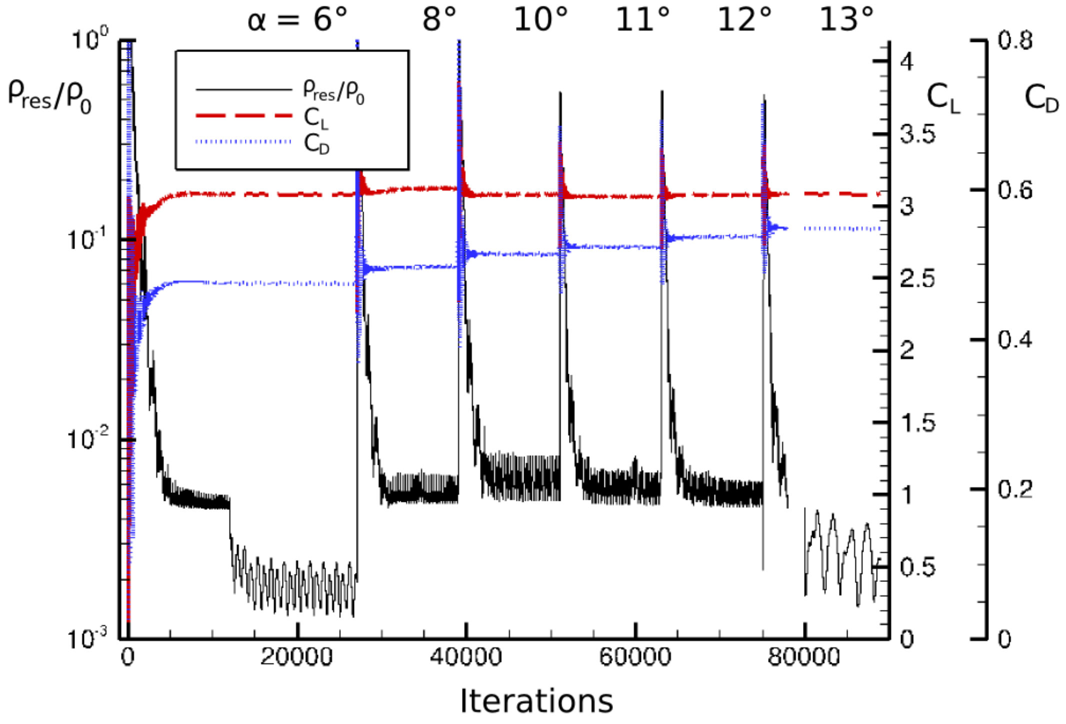

Figure 5.2: Convergence behaviour, simulation of the complete lift curve

78 000 iteration steps that the density residual is further decreased. This signifies that during the calculation of $\alpha = 13°$, the initial CFL-number of 4.0 has been set to 2.0. In addition, the calculations have been continued on the single grid which results in a more accurate resolution of the flow variables. As a matter of principle, all configurations show a similar convergence behaviour. If convergence could not be reached within the given iteration steps, additional iterations have been performed. The few calculations at $\alpha = 7°$ and $9°$ will be performed in the same manner.

5.2 Configuration 11-6: without Strake

In this section the landing configuration without strake, namely configuration 11-6, is regarded. Therefore, a complete lift curve has been calculated, which is depicted in 5.3(a). It can be seen that the slope of the lift curve decreases after an angle of attack of $6°$. Finally, the maximum lift coefficient of $C_{L,max} \approx 3.12$ is already reached at $\alpha_{max} = 8°$. The corresponding spanwise distributions of the section lift coefficient c_l for the cases $\alpha = 6°$,$8°$ and $10°$ are represented in 5.3(b). The nacelle symmetry plane is located at about 35% of the wing semispan, which can be verified by Figure B.6 in the appendix. The nacelle position is characterised by a local minimum of lift. On the left hand side of the nacelle, the inboard nacelle vortex can be identified. At an angle of attack of $6°$, the vortex is only noticeable by a small local minimum in the distribution. However, at α_{max} the vortex is clearly visible and results in a slight lift loss at $y/s \approx 0.25$ while lift is increasing in the other areas of the wing. At the post-stall angle of attack $\alpha = 10°$, the inboard vortex causes a significant lift collapse that spreads to the sides and also leads to high losses in the nacelle wake region. The nacelle outboard vortex can be located on the other side at about 41% of the wing semispan. Its effect on c_l is only moderate even at high angles of attack. We can indeed see a lift minimum at $\alpha = 10°$, but the loss is very small compared to the loss caused by the inboard nacelle

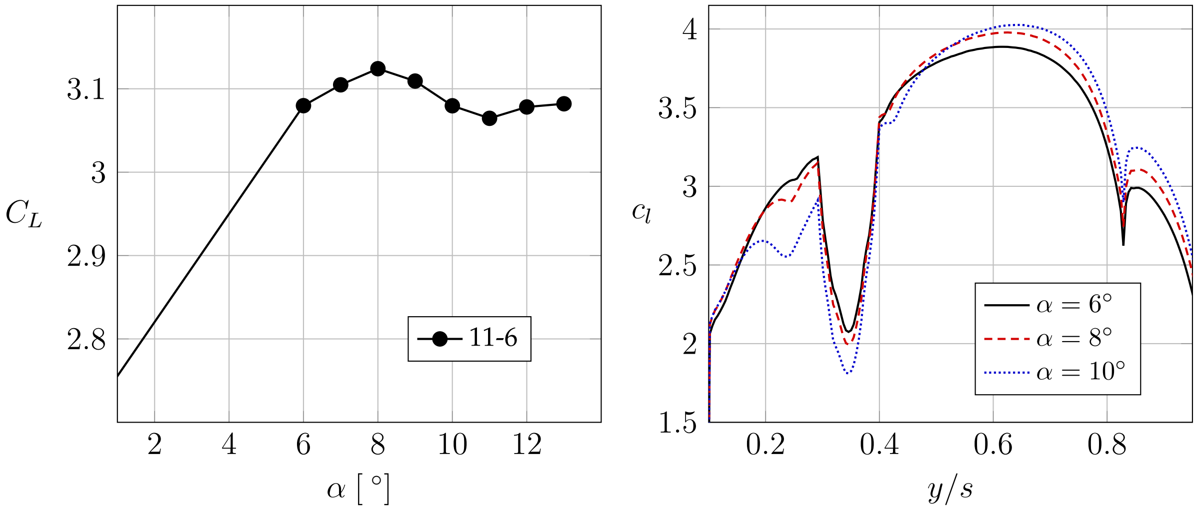

(a) Lift curve (b) Spanwise distribution of $\mathbf{c_l}$

Figure 5.3: $\mathbf{C_L}$-characteristics of configuraton 11-6

vortex. This fact suggests the higher significance of an inboard strake. At $y/s \approx 0.82$ another minimum can be recognised. At this position the gap between flap and aileron is situated, which leads to a reduced generation of lift in this section. In addition, trailing tip vortices are shed on flap and aileron which lead to locally detached flow.

Since the negative effects of the inboard nacelle vortex are already distinct at α_{max}, this is the most interesting case in order to analyse the nature of these effects. In the following, we will therefore concentrate on this case. Figure 5.4 shows the propagation of both the inboard and the outboard nacelle vortices, visualised by streamlines. The aircraft's surface is coloured by the local streamwise friction coefficient $c_{f,x}$. In addition, multiple slices are shown that represent the vorticity in x-direction along the vortices. It can be seen that the outboard nacelle vortex rotates along and the inboard vortex rotates against the x-direction. Furthermore, it is noticeable that the vortices propagate in opposite directions and get weaker along their paths. The surface contours reproduce the effects of the vortices. Basically, it can be said that the skin friction coefficient, due to its relation to the velocity gradient, represents the tendency of a flow to separate.

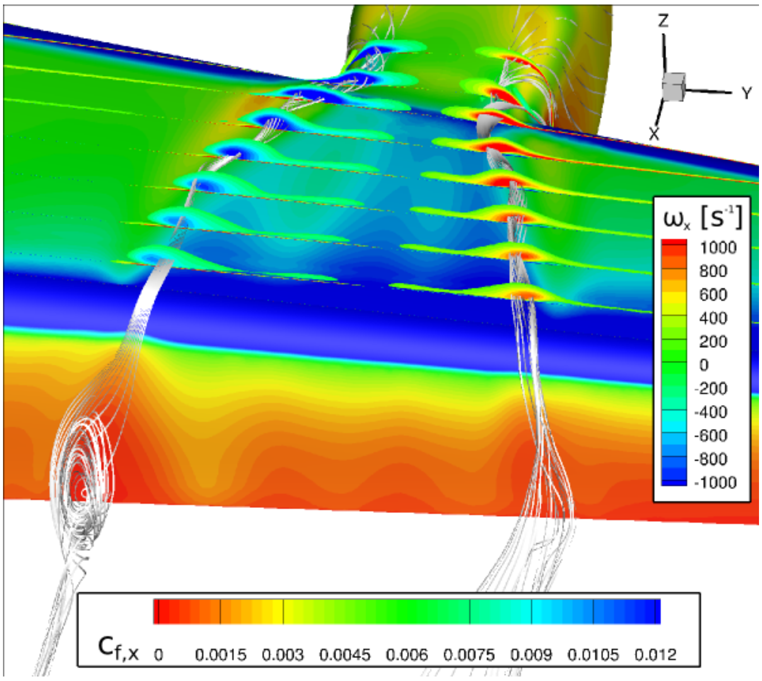

Figure 5.4: Nacelle vortex propagation of configuration 11-6 at $\alpha = 8°$

We can see that the skin friction in x-direction in the upwash regions of the vortices are reduced which is equivalent to a weakening of the boundary layer. This becomes particularly clear by regarding the inboard area near the droop nose where $c_{f,x}$ has a local minimum or by regarding the transition region between the main wing and the flap. In contrast, the boundary layer is strenghtened in the downwash region between the vortices. Consistently, the skin friction is higher in this region. Near the flap's trailing edge $c_{f,x}$ is further reduced. The region on the flap the outboard vortex propagates through is characterised by low $c_{f,x}$ which are sill positive. The streamtraces also clarify that the flow is fully attached there. In contrast, the inboard nacelle vortex seems to be more critical. The streamtraces here are very irregular. However, the local skin

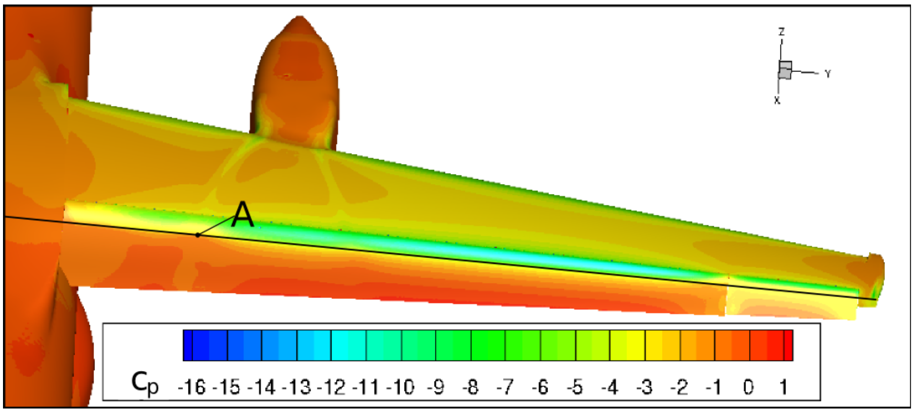

Figure 5.5: Wing c_p-distribution of configuration 11-6 at $\alpha = 8°$

friction coefficient still has a positive value, which indicates that the inboard nacelle vortex causes a wake burst above the flap. This means that the flow is still attached at the surface while the flow in the wake is separated. For further information, Figure B.8 in the appendix can be regarded, which illustrates the wake burst and moreover shows that the flow is still attached.

This is also shown by Figure 5.5, which shows the c_p-distribution on the wing's surface and on the nacelle. The nacelle vortices are traced on the main wing's surface and the region of the wake burst is characterised by a lack of pressure recovery on the flap. Detail A is given in Figure 5.6. It shows a closeup view of the inboard nacelle vortex by means of a cutting plane at $x = 15.09\ m$. An overview of all cutting planes and their positions on the wing is provided by Figure B.7 in the appendix. It is coloured by the total pressure loss $p_{t,loss}$. In addition, the tangential velocity vectors inside the plane are shown. Hereby, the vectors represent the velocities relative to the vertical velocity of the vortex core. It should be noted that the vectors are illustrated with uniform lengths in order to provide a better clarity. The negative total pressure loss signifies total pressure gain due to the employment of active blowing which inserts energy into the flow. The figure shows that the vortex is accompanied by a loss of energy whereby the maximum loss occurs slightly below the core. We can observe that the vortex, which is very close to the surface and very strong, interacts with the jet layer. It induces velocities of which those normal to the surface are most critical. The high energy layer of the active blowing is washed to the side and replaced by low energy flow of the surrounding flow field. Hence, the effect of the active blowing is locally missing and the outer flow layers cannot follow the high turning angles of the flap's contour any more. As a consequence, a wake burst occurs that expands at higher angles of attack and leads to the significant lift collapse.

5.3 Configuration 11-6S2: with initial Strake

Before the nacelle strake study is carried out it is important to understand the effects of the initial strake. This strake, deployed in configuration 11-6S2, has been designed in a pre-study. Its geometry and dimensions are depicted in Figure 5.7. It is mounted

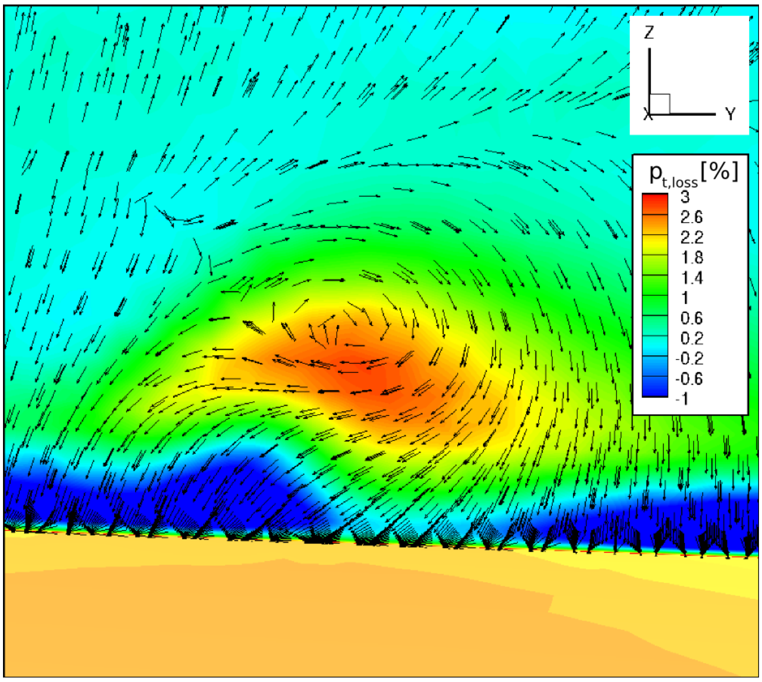

Figure 5.6: Detail A: Cut at $\mathbf{x} = \mathbf{15.09\ m}$ revealing $\mathbf{p_{t,loss}}$ on the flap at $\boldsymbol{\alpha} = \mathbf{8}^\circ$

with a setting angle of $\alpha_S = -5^\circ$ and has a root chord of $c_{S,root} = 0.6\ m$ and a semispan of $s_S = 0.3\ m$ which makes a root chord-semispan ratio h_S of 2.0. Its reference area is $0.132\ m^2$ which will be defined within this project as a strake size factor of $f_S = 6.0$. It is placed near the vertical nacelle symmetry plane and with a distance to the nacelle-droop nose-intersection of about $1.5\ m$.

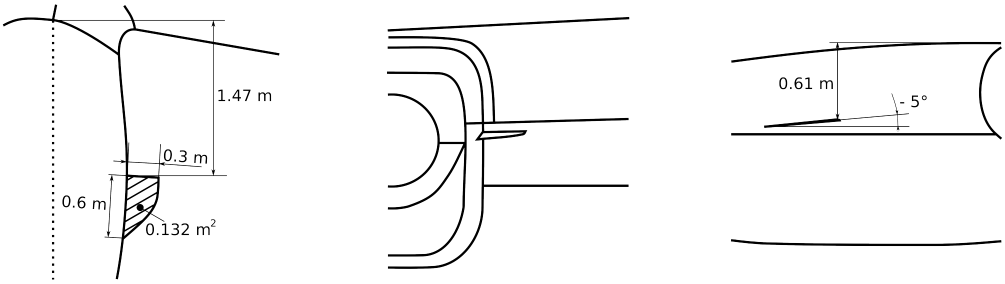

(a) Top view (b) Front view (c) Side view

Figure 5.7: Geometry and dimensions of the initial strake

5.8(a) shows the lift curve of configuration 11-6S2. In addtion, it contains the lift curve of the configuration without strake. The utilisation of this initial strake already allows for a significant lift recovery of about $14\ LC$ leading to $C_{L,max} \approx 3.26$. Furthermore, it rises α_{max} by $\Delta\alpha = 2^\circ$, shifting it to $\alpha_{max} = 10^\circ$. In Figure 5.8 the spanwise c_l-distribution is shown for $\alpha = 8^\circ$ and 10° in comparison with those of configuration 11-6. It can be seen that lift in the inboard nacelle vortex area at about 25% of the wing semispan can be largely recovered at $\alpha = 8^\circ$ by using the strake. Furthermore, at $\alpha = 10°$ a further lift increase in the inboard region is achieved. This behaviour signifies that the inboard nacelle vortex is appreciably weakened and the effect of the increase of angle of attack predominates.

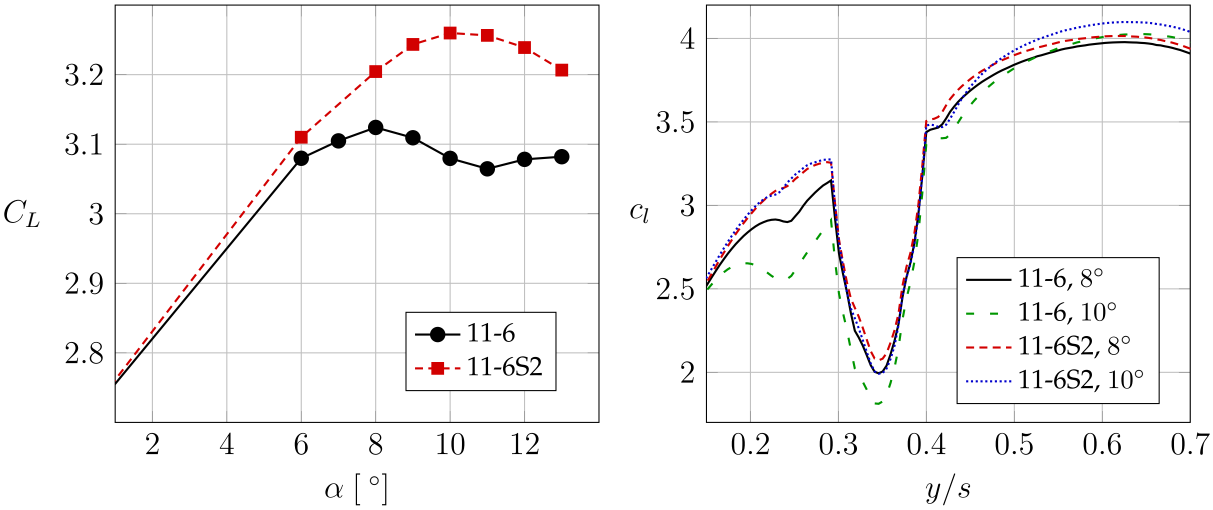

(a) Lift curve

(b) Spanwise distribution of $\mathbf{c_l}$

Figure 5.8: $\mathbf{C_L}$-characteristics of configuration 11-6S2

In the following we will again concentrate on the solution at an angle of attack of 8° to provide comparability to the solution of configuration 11-6. Figure 5.9 shows the junction area and the shedding of the vortices. The vortices are visualised using Iso-Surfaces defined by the constant values of the kinematic vorticity $\omega_k = 1.2$, 1.5 and 2.0. Since the kinematic vorticity number denotes a vorticity-shear ratio (see subsection 2.3.4), the advantage of the utilisation ω_k is that the boundary layer, containing high gradients due to shear stresses, is not illustrated. The surfaces are then coloured according to their sense of rotation. It can be seen that the strake vortex passes the upper wing's surface with a much greater distance than the nacelle vortices. We can likewise recognise that the strake vortex already interacts with the inboard nacelle vortex on the nacelle which results in a second faint vortex and a weakening of the initial inboard nacelle vortex. This can also be observed in Figure 5.10 which shows the vortices, visualised by streamtraces. Here, it can be seen that the strength of the inboard nacelle vortex decreases significantly thanks to the strake vortex. Near the flap, its core has a strength of $\omega_x \approx -300\ s^{-1}$. By comparison, the nacelle vortex core at this streamwise position in the case of configuration 11-6 had a strength of $\omega_x \approx -750\ s^{-1}$. The result is a fully attached flow in the wake above the flap and the absence of a wake burst. The second vortex decays rapidly and has no essential influence on the flow field near the flap. However, the utilisation of a strake vortex seemingly has some influence on the outboard nacelle vortex which is slightly reinforced. Figure 5.11 shows the c_p-distribution on the wing of configuration 11-6S2. Consistently to the above mentioned observation, at the flap's trailing edge of the outboard nacelle vortex propagation path, a lack of pressure recuperation can be recognised. However, the flow in this region is still attached and this has no significant influence on the lift distribution (as seen in 5.8(b)). The c_p-distribution again clarifies that the inboard nacelle vortex is weakened

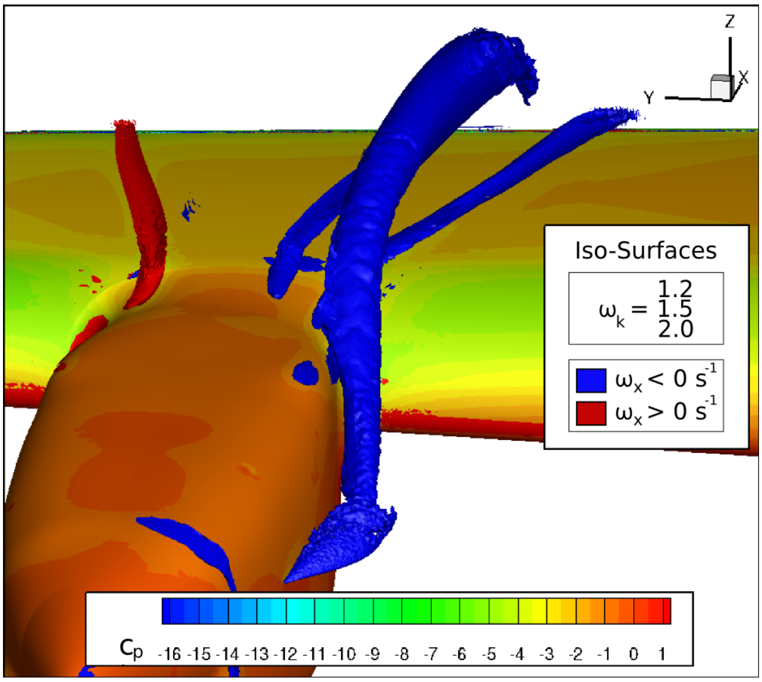

Figure 5.9: Shedding of vortices in the junction area of configuration 11-6S2 at $\alpha = 8°$

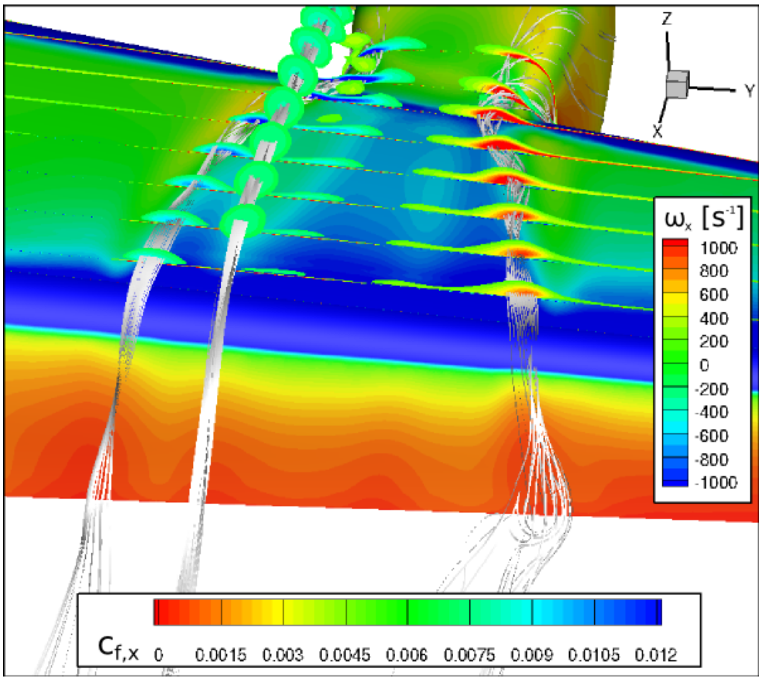

Figure 5.10: Nacelle and strake vortex propagation of configuration 11-6S2 at $\alpha = 8°$

by the strake vortex. Its traces on the wing's surface vanish at about 25% of the local chord. Furthermore, pressure is regained at the flap's trailing edge in the inboard nacelle vortex path. In order to further understand the result of the weakening of the inboard nacelle vortex on the flow conditions on the flap, Figure 5.12 illustrates the

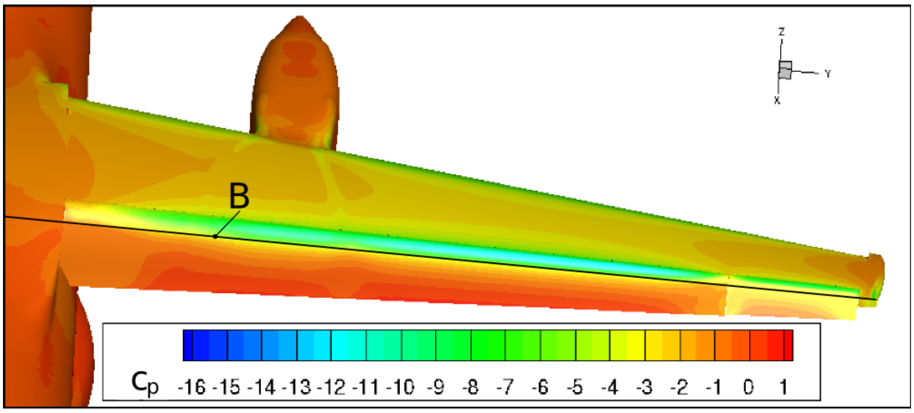

Figure 5.11: Wing c_p-distribution of configuration 11-6S2 at $\alpha = 8°$

cutting plane of Detail B at the same x-position as in Figure 5.6. It is likewise coloured by $p_{t,loss}$. Detail B includes both the inboard nacelle vortex and the strake vortex. The tangent velocity vectors are again given with uniform lengths. In addition, the vectors are here referred to the vertical velocity of the strake vortex core. Due to the larger frame and the differences in vertical velocity of the different layers, this allows for a better clarity. As a result of the weakening of the inboard nacelle vortex, the induced velocities are not high enough to entrain the complete high energy layer. We can indeed observe that a part of the jet layer is washed to the side but especially near the flap's surface the jet layer prevails. Hence, the *Coanda-effect* of active blowing is preserved and the wake burst is prevented. In addition, the strake vortex itself, which is

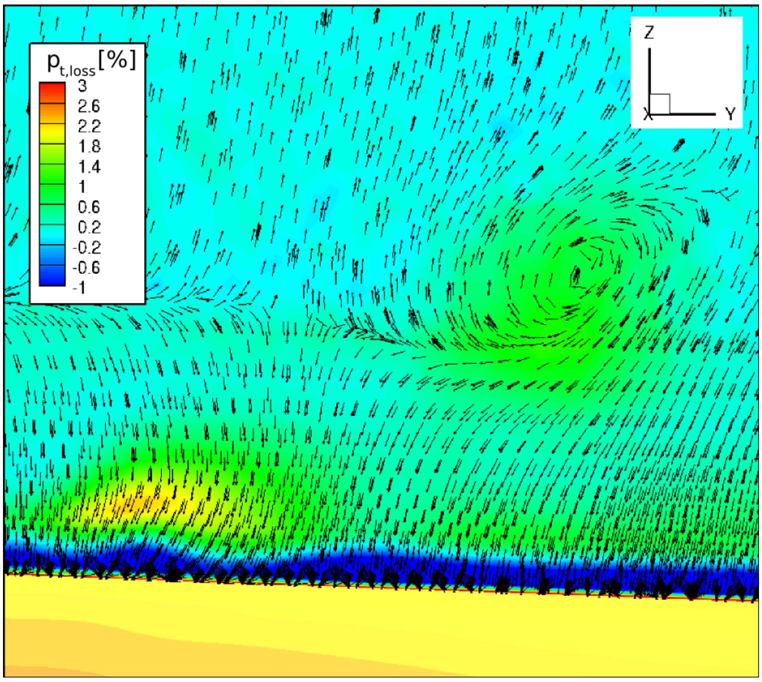

Figure 5.12: Detail B: Cut at $\mathrm{x} = 15.09\ \mathrm{m}$ revealing $p_{t,loss}$ on the flap at $\alpha = 8°$

accompanied by a smaller loss of total pressure, has no significant influence on the jet layer. Due to its greater distance to the flap surface, its induced velocities do not create a sidewash of the layer.

In summary, it can be said that the intial strake has a perceivable effect on the flow field. The trailing edge separation can be suppressed and a significant lift recovery is achieved. This fact can be attributed to the weakening of the inboard nacelle vortex resulting in a fainter sidewash of the high energy layer. Nevertheless, the detail cut reveals that the nacelle vortex still interacts with the jet layer and weakens the local flow near the surface. This circumstance suggests that a larger recuperation of lift by modification of the strake is possible. The cutting plane view indicates that the distance between inboard nacelle vortex and strake vortex is still large. Thus, further improvements are supposed to be possible by reduction of the distance between the vortices on the flap or by an amplification of the strake vortex. These modifications will be undertaken stepwise within the following section.

5.4 Configuration 11-6S3: Maximisation of $\mathrm{C}_{\mathrm{L,max}}$ by Variation of Strake Parameters

This section centers around the optimisation and design process of the new inboard nacelle strake for configuration 11-6S3. As the goal of this project is the maximisation of the maximum lift coefficient, the validation of a strake version requires the calculation of a complete lift curve of the aircraft configuration. With respect to the amount of strake parameters and the high numerical effort of a calculation, it is not efficient to calculate the lift curves for every strake parameter variation. Therefore, the strake design process will be performed within three consecutive steps:

1. The first step comprises the investigation of single and multiple strake parameter changes in consideration of their impact on C_L at $\alpha = 6°$. On the basis of the results, a pre-selection of suitable strake parameters is made that delimits the design range.
2. Within the second step, higher angles of attack are calculated based on the design range of the first step in order to evaluate the strake parameters' impact on $C_{L,max}$. Subsequently, further configurations are then selected by means of these evaluations, calculated and analysed at α_{max} .
3. Finally, the most promising strake of the previous step is regarded in detail and further optimised by slight variations of single parameters.

Generally speaking, the problem of finding the best combination of nacelle strake parameters can be divided into the task of finding the optimal position and the task of finding the geometry in order to realise a proper strength of the vortex. The closer the strake vortex is located to the inboard nacelle vortex on the flap, the smaller the vortex strength can be dimensioned. Therefore, we will pay particular attention to the strake's location.

5.4.1 Strake Parameters

The nacelle strake parameters that are to be varied within this project and the expected associated impacts on the strake vortex are:

- **The strake setting angle $\boldsymbol{\alpha}_\mathbf{S}$**: According to Eq. 2.7, Eq. 2.11 and Eq. 2.17, the strength of the strake vortex is supposed to be linearly dependent on α_S, as long as the strake angle of attack is small. However, a constraint for the parameter study is the minimisation of the drag caused by the strake in cruise flight. Hence, the strake setting angle shall be mounted in such a way, that it is parallel to the streamlines. If the strake is positioned at some distance to the wing's leading edge, this will approximately be the case, if the angle is set in such a manner that it is equivalent to the negative angle of attack in cruise flight, meaning

  $$\alpha_S = -\alpha_{cruise}, \tag{5.1}$$

  which depends on the actual weight of the aircraft. In case of a flight with constant velocity and constant height, $C_{L,cruise}$ and α_{cruise} change constantly. Therefore, the average value of the cruise flight is used which results in a strake setting angle of $\alpha_S = -2.65°$. This parameter will not be changed any more during the optimisation process.

- **The streamwise strake position $\mathbf{x_S}$**: This parameter is basically assumed to have the following three major impacts on the strake vortex:

  1. The streamwise displacement of the strake and thereby of the origin of the strake vortex leads to a change of height of the vortex line, passing the wing, because the strake vortex is entrained by different layers of the oncoming flow.
  2. Due to the concave form of the nacelle, the strake position change in x-direction is accompanied by a displacement of the strake in y-direction. As a result, the vortex passes the wing either further inboard or further outboard. This effect can be clarified by regarding Figure 5.13.
  3. The strength of the vortex on the flap is altered. On the one hand, this is caused by the change of the path length from strake to flap and the associated changed dissipation. On the other hand, the closer the strake is placed to the wing, the higher is the effective angle of attack due to the circulation field around the wing.

  The streamwise strake position x_S will be given relative to the inital strake position.

- **The vertical strake position $\mathbf{z_S}$**: This parameter variation mainly affects the height of the vortex line, passing the wing. If the strake is additionally placed near the wing, the effective angle of attack at the strake is also influenced by this parameter. The vertical strake position z_S will also be given in relative coordinates.

- **The strake geometry relation given by the size factor $\mathbf{f_S}$ and the strake root chord-semispan ratio $\mathbf{h_S}$**: The variation of the strake geometry primarily affects the strength of the strake vortex linearly according to Eq. 2.7, Eq. 2.10 and Eq. 2.17. Nevertheless, the higher size factor f_S also results in a higher strake semispan, resulting in a vortex displacement in y-direction as well as a displacement of the strake trailing edge in x-direction. We also have to keep in mind that a modification of the strake root chord-semispan ratio h_S affects the strake aspect ratio, resulting in a different slope of the strake's lift curve (Equation 2.13), and thereby resulting in a slightly changed vorticity of the vortex.

Parameters	α_S	x_s	z_S	f_S	h_S
11-6S2	$-5°$	$0\,mm$	$0\,mm$	6.0	2.0

Table 5.4: Parameters of the initial strake

Together with these definitions, we can now summarise the strake parameters of the initial strake (configuration 11-6S2) in Table 5.4. All position modifications will in the following be given relative to the initial strake's position.

5.4.2 Influence of Parameter Changes on the Lift Coefficient at $\alpha = 6°$

To begin with the nacelle strake parameter study, we will first focus on the modification of single and multiple parameters in order to obtain an idea about their basic influences on the lift coefficient at an angle of attack of $6°$ and of the effects with respect to the flow field.

Variation of the streamwise Strake Position $\mathrm{x_S}$

Firstly, the streamwise strake position x_S is varied while the other parameters are kept constant. Figure 5.13 shows the top view of the modifications. In relation to the initial strake at $z_S = 0\ mm$, the positions are set to -200, 100, 200, 400 and $600\ mm$. It can be seen that the displacement also results in a slight change of the y-coordinate of the strake. The resulting lift coefficients at $\alpha = 6°$ are revealed by Figure 5.14. We can see that the highest C_L is obtained if the strake is located at a position of about 0 to $200\ mm$ relative to the initial strake, which is represented by a white dot. Thereby, a relative minimum occurs at $x_S = 100\ mm$, suggesting that no algebraic relation between C_L and x_S exists. We also observe that a single displacement streamup has no eligible effect. On the other hand, the strake's effect deteriorates as soon as it approaches the wing leading edge.

Figure 5.15 shows the distribution of $c_{p,min}$ on the flap in the frame of the vortex paths for some of the variations. Since the suction peak is very sensitive to the local flow conditions, it is suitable to identify the effect of the strake modifications. In addition, the distribution for configuration 11-6 is depicted. The suction peaks on the flap are supposed to appear in the region of the highest curvature of the flap surface, which is near the main wing trailing edge. Here, the inboard nacelle vortex is located at about 25% of the wing's semispan, as can be seen from the loosely dashed curve, representing

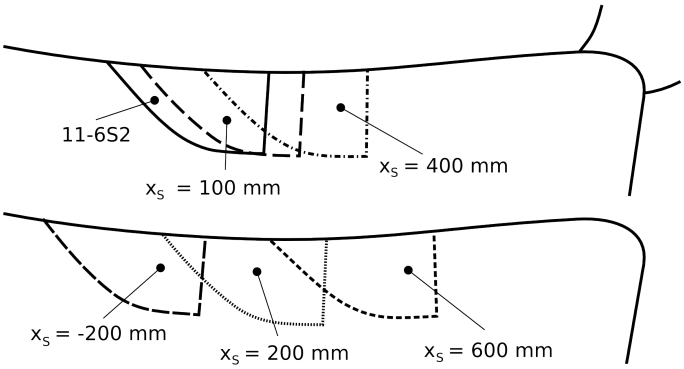

Figure 5.13: Strake configurations with different streamwise positions $\mathbf{x_S}$

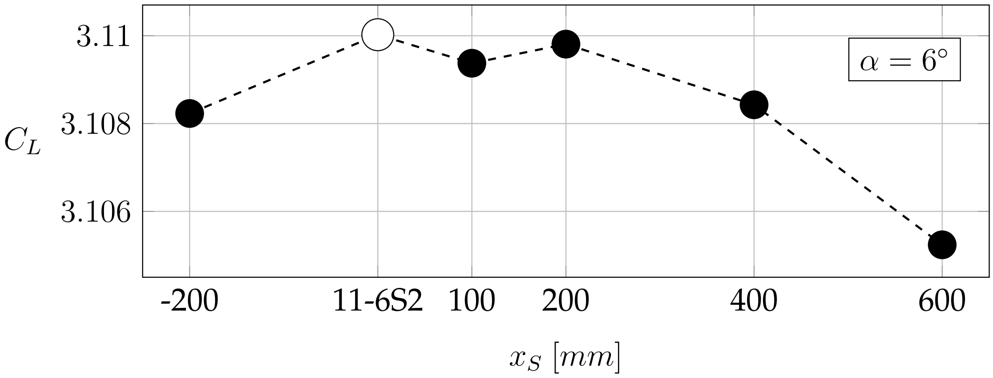

Figure 5.14: Influence of a variation of $\mathbf{x_S}$ on $\mathbf{C_L}$

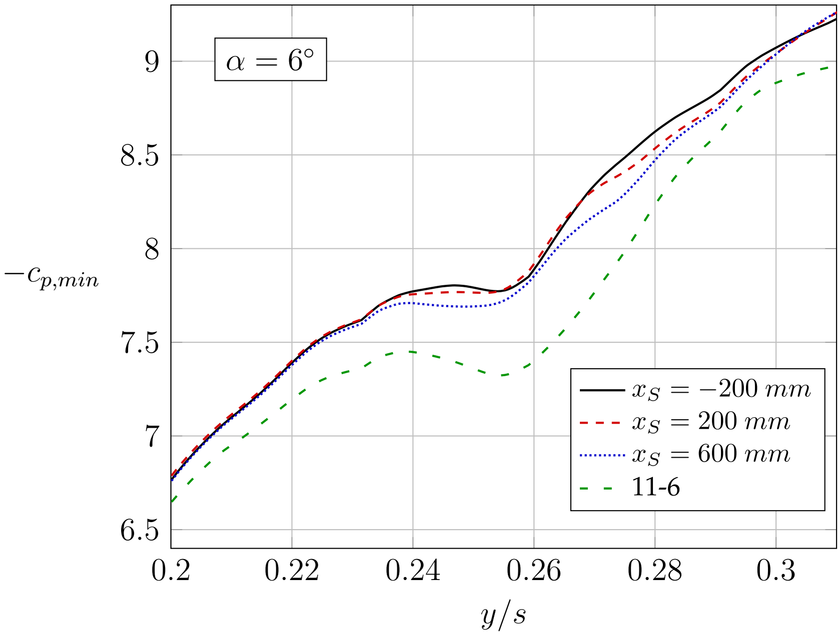

Figure 5.15: $\mathbf{c_{p,min}}$-distribution on the flap for different streamwise strake positions $\mathbf{x_S}$

configuration 11-6. The strake vortex lies, depending on the actual configuration, in a range of about $y/s \approx 0.265$ to 0.27. The vortices are characterised by a wave-like pattern with a relative maximum on the left and a relative minimum on the right-hand side. Against this background, it can be said that a hypothetical perfect strake would lead to a smooth distribution of $c_{p,min}$ without local extreme values. We can see that the strake at $x_S = 600\ mm$ shows the strongest interaction with the nacelle vortex. This might be caused by its supposingly stronger vortex because the strake is further in the circulation field of the wing. However, this is accompanied by a higher downwash on the right-hand side of the strake vortex, recognisable by the lower suction peak. The vortex shed by the strake at $x_S = -200\ mm$ has a different effect on the distribution. It does not perceptibly interact with the nacelle vortex, which is suggested by the distinct wave-like pattern. However, its downwash is also weaker which results in a higher suction peak on the right hand side. The strake at $x_S = 200\ mm$, resulting in the highest C_L of the configurations, discussed in this figure, shows moderate interaction with the nacelle vortex.

In summary, a single variation of the streamwise strake position has a relatively weak influence on the effectiveness of the strake at $\alpha = 6°$. The resulting changes of the lift coefficient lie in a range of $\Delta C_L \leq 0.5\ LC$.

Variation of the vertical Strake Position $\mathbf{z_S}$

Secondly, the consequence of a modification of the vertical strake position z_S shall be examined. Therefore, five different strake configurations at $z_S = -100$, 100, 150, 200 and $250\ mm$ are investigated. Figure 5.16 gives an idea of their arrangement on the nacelle by illustration of the side view. The resulting lift coefficients are depicted in Figure 5.17. According to this C_L-distribution the optimal range lies between $z_S = 100\ mm$ and $z_S = 250\ mm$. Below this range, the lift coefficient decreases considerably. Since the initial strake is located at a lower position, improvements of the strake by modificiation of this parameter seem to be attainable.

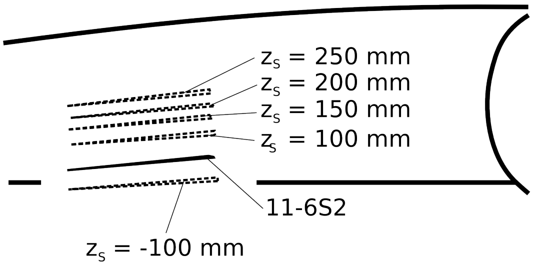

Figure 5.16: Strake configurations with different vertical positions $\mathbf{z_S}$

The suction peak distribution on the flap is represented by Figure 5.18. The distributions are given for three representative configurations. As can be seen, the configuration at $z_S = -100\ mm$ shows no good performance, which is in accordance with the lift coefficient. Due to the proximity of the vortex to the wing's surface, its downwash has a significant influence on the $c_{p,min}$-distribution on the right-hand side beyond $y/s \approx 0.27$. In addition, it does not seem to further minimise the nacelle vortex, for the

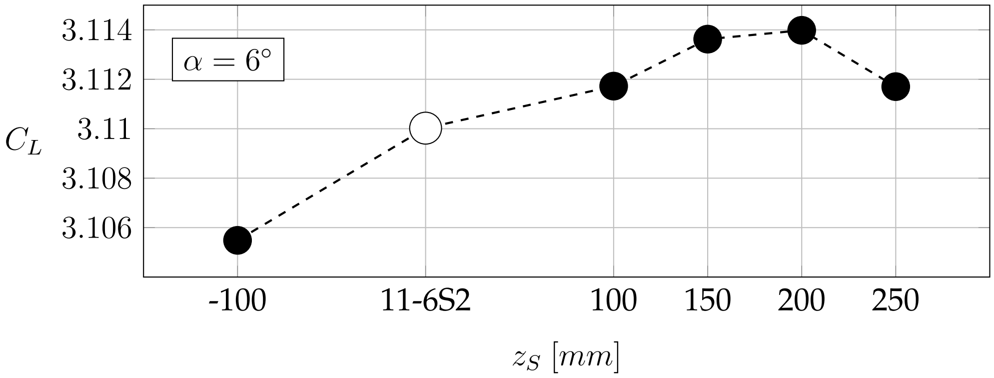

Figure 5.17: Influence of a variation of $\mathbf{z_S}$ on $\mathbf{C_L}$

distinct wave-pattern is still recognisable. On the contrary, the strakes at $z_S = 100\ mm$ and at $200\ mm$ both show a good behaviour with respect to the interaction with the nacelle vortex. We see that the wave-pattern is smoothed, which implies that the nacelle vortex is weakened, in the same way by both strakes. Nevertheless, the difference in C_L seems to arise from the downwash region of the strake vortex. The vortex of the strake, located at a higher z_S seemingly has a lower impact due to downwash on the flow near the surface. This results in a higher suction peak and likely in a higher lift coefficient. Therefore, the strake needs to be dimensioned in such a manner that the nacelle vortex is weakened as much as possible. On the other hand the effect of the vortex on the flow near the surface also needs to be minimised.

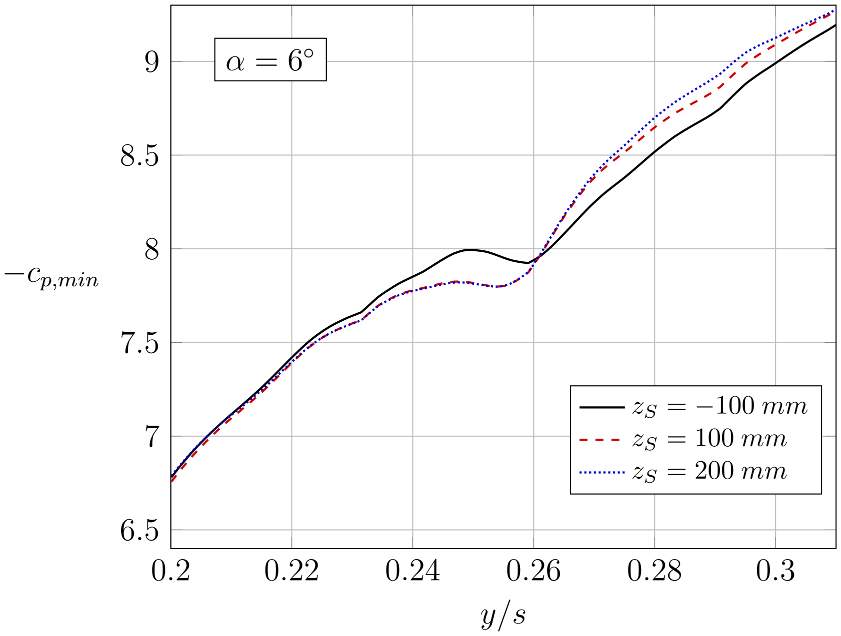

Figure 5.18: $\mathbf{c_{p,min}}$-distribution on the flap for different vertical strake positions $\mathbf{z_S}$

To conclude, the single variation of z_S can lead to a lift recuperation of up to $\Delta C_L \leq 0.8\ LC$, whereby the interaction of the strake vortex with the flow itself also plays an important role.

Variation of the Strake Geometry by $\mathbf{f_S}$ and $\mathbf{h_S}$

Finally, the geometry of the strake is modified. Therefore, two different parameters are available. On the one hand, the strake area can be varied by a modification of the strake root chord, whereas the strake semispan as well as its trailing edge position are kept constant. Figure 5.19 shows a strake with an underlying root chord increase of 33%, which is equal to a ratio of $h_S = 2.67$ and a resulting changed size factor of $f_S = 8.0$. On the other hand, the strake size factor f_S can be varied. Thereby, both root chord and semispan are modified by the same amount. As a consequence, the root chord-semispan ratio stays constant. A top view of a strake whose dimensions are increased by 33% is also provided by Figure 5.19. It has a new size factor of $f_S = 10.68$.

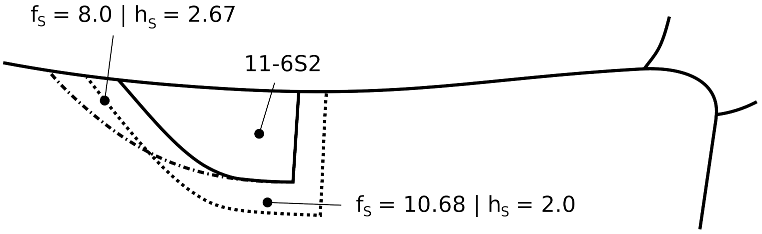

Figure 5.19: Strake configurations with different geometries

The resulting lift coefficients are depicted in Figure 5.20. As can be seen, the strake with $f_S = 8.0$ and $h_S = 2.67$ allows for an increase of $\Delta C_L \approx 0.5\ LC$. A further improvement is achieved by the other strake. The further increase of f_S, paired with an accompanied slight change in position, leads to an additional augmentation of $\Delta C_L \approx 0.1\ LC$ at an angle of attack of 6°. However, it can be supposed that the positive effect of a single change of the size factor reaches its limit in this range, because the further increase leads to a relatively small improvement compared to the foregoing modification of h_S.

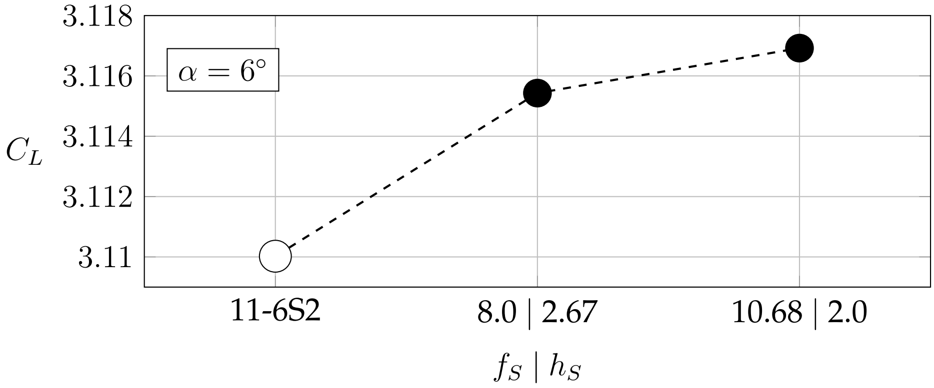

Figure 5.20: Influence of a variation of $\mathbf{z_S}$ on $\mathbf{C_L}$

The suction peak distributions on the flap for these configurations are given by Figure 5.21. We can observe that the strake with $f_S = 10.68$ and $h_S = 2.0$ shows a good performance in weakening the nacelle vortex. This is manifested through the suction peaks at about 25% semispan. Not only is the course clearly smoothed in this area, but the wave-like pattern, indicating the vortex, is nearly completely negated. Furthermore, we can observe that the suction peaks in the downwash area of the strake vortex are slightly higher than those of the initial configuration. This might be explained by the longer semispan of the strake. Due to the displacement of the vortex path in y-direction, it could be supposed that the region of downwash and thereby the line of $c_{p,min}$ is slightly shifted to a lower y/s. In addition, this displacement leads to a higher interaction between the nacelle and the strake vortex which also results in a higher reduction of the strake vortex. As a consequence, a fainter downwash is caused by the strake vortex and the magnitude of the suction peaks are increased.

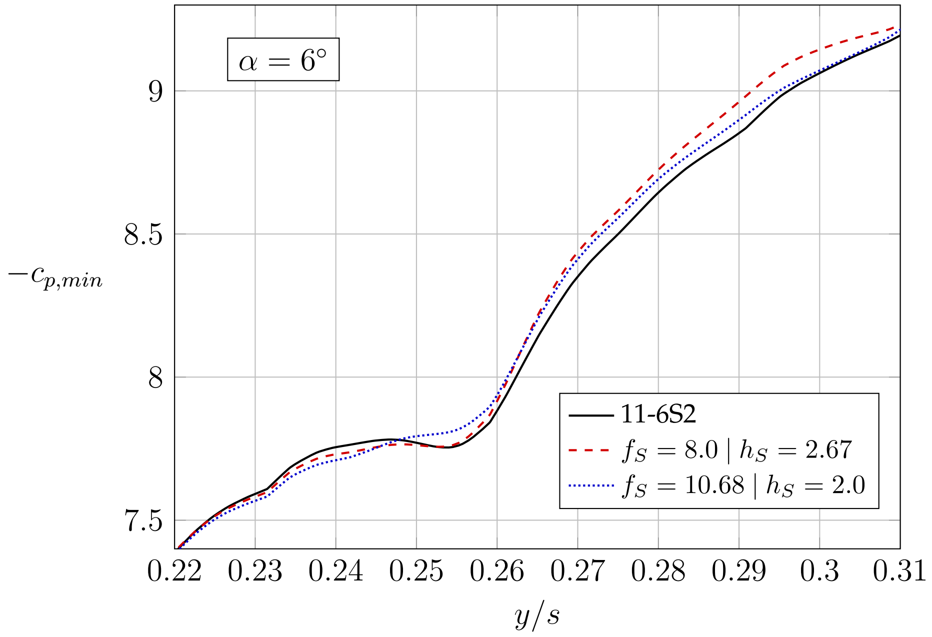

Figure 5.21: $\mathbf{c_{p,min}}$-distribution on the flap for different strake geometries $\mathbf{f_S}$ and $\mathbf{h_S}$

The strake with $h_S = 2.67$ also effectuates a weakening of the nacelle vortex. Indeed, the nacelle vortex still seems to be stronger than in the case of the bigger strake, but the wave-like pattern is less distinct than in the case of the initial strake. In addition, we see that it provides a higher distribution of $c_{p,min}$ on the right-hand side of the strake vortex compared to the strake of configuration 11-6S2. This suggests that the strake vortex might be reduced more effectively by the nacelle vortex than the one shed by the initial strake. Therefore, the downwash might be lower. Furthermore, the strake vortex of $h_S = 2.67$ is fainter than the vortex of the biggest strake. Hence, it is accompanied by a higher suction peak in this area compared to the strake with $f_S = 10.68$.

It can be summarised that by a single modification of the strake geometry, by means of the parameters f_S h_S, a lift recovery of up to $\Delta C_L \approx 0.6\ LC$ can be obtained at $\alpha = 6°$.

Multiple Variations of Strake Parameters

As we have seen, single parameter modifications have already shown improvements with respect to the lift coefficient at an angle of attack of $6°$. However, the increase of C_L is only moderate. Therefore, multiple parameters are varied in the following to obtain further augmentation. Thereby, we will not only concentrate on the range including the parameters that have shown the best results but also examine if synergies exist between parameter changes that have had little positive effect as a single modification. A single exception is made in the case of the strake at $x_S = 600\ mm$. The foregoing investigations have shown that this strake, especially due to the high strength of the shed vortex, has no potential to allow for an increase of C_L. This is caused by its locatation near the wing's leading edge and thereby in its circulation field. Thus, it can be expected that the effective strake angle of attack would increase stronger near α_{max} than those of the strakes being located further upstream. As a consequence, the resulting strake vortex would presumably be too strong.

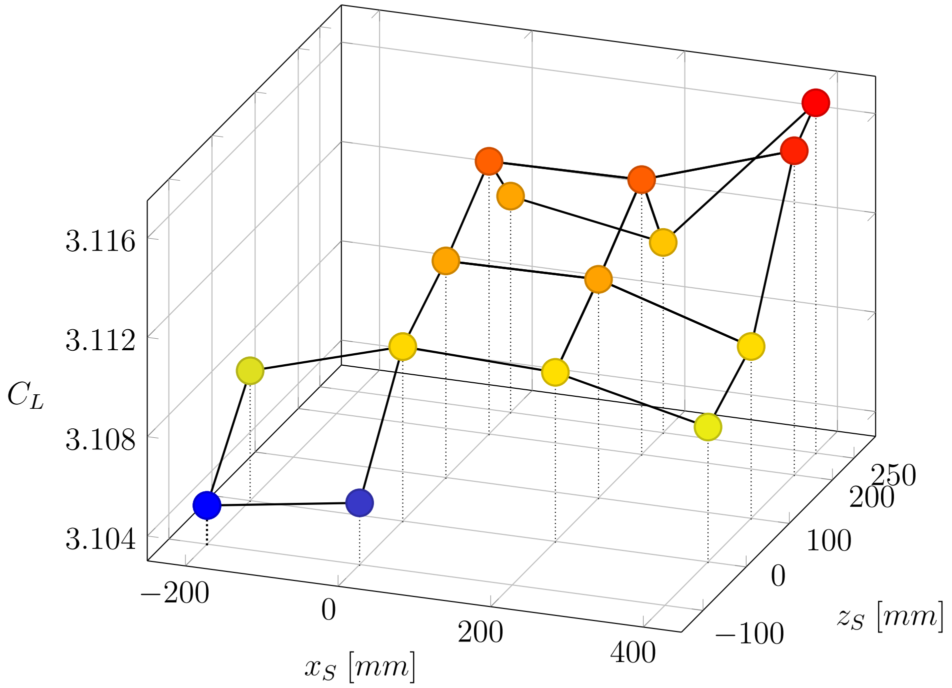

Figure 5.22: Influence of simultaneous variations of $\mathbf{x_S}$ and $\mathbf{z_S}$ on $\mathbf{C_L}$ at $\boldsymbol{\alpha} = \mathbf{6°}$

The calculated lift coefficients due to multiple strake position variations with the initial strake form are represented by Figure 5.22. As can be seen, a decrease of the vertical strake position z_S in relation to the initial strake does not result in an improvement, not even in combination with a variation of x_S. Besides, a strake at $x_S = -200\ mm$ neither seems to have any potential. On the contrary, strakes at z_S between $200\ mm$ and $250\ mm$ show a good performance, which is in accordance with the results obtained for single parameter changes. We can see that these strakes are most suitable at $\alpha = 6°$ in combination with streamwise positions at $x_S = 200\ mm$ and $400\ mm$. Unlike as observed within the single parameter changes, a maximum is observed at $x_S = 400\ mm$ and $z_S = 250\ mm$. With $C_L \approx 3.117$, the maximum is by $0.3\ LC$ greater than obtained for a single variation of a position parameter. At z_S between $0\ mm$ and $100\ mm$, the maximum lies at $x_S = 0\ mm$.

For a further increase of the lift coefficient, a strake geometry variation is now additionally undertaken. Due to the smaller surface, we choose the strake form with $f_S = 8.0$ and $h_S = 2.67$, in order to be able to achieve further improvement by geometry enlargement within the final optimisation step of the strake. Based on the results of the simultaneous position variations with the initial strake geometry, we will further delimit the range to $0\ mm \leq x_S \leq 400\ mm$ and $100\ mm \leq z_S \leq 250\ mm$.

Figure 5.23 represents the resulting lift coefficients for the simultaneous position variations in combination with the adjusted strake geometry. It is visible that a geometry variation has a negative effect on the strake at $x_S = 0\ mm$ and $z_S = 100\ mm$. With $C_L \approx 3.109$ a decrease of about $0.3\ LC$ is obtained compared to the initial form. Nevertheless, all other strakes experience an increase of C_L thanks to the adapted geometry. The absolute maximum is now again reached by the strake at $z_S = 200\ mm$, which is encircled by a dashed line. The corresponding x_S-position is at $200\ mm$. Its lift coefficient of about 3.124 is about $1\ LC$ higher than before the geometry change. Another relative maximum is obtained by the utilisation of the strake at $x_S = 400\ mm$ and $z_S = 250\ mm$. This configuration, which is also encircled in the figure, has represented the maximum in the investigations made before. Its increase of about 0.6 to $C_L \approx 3.13$ is therefore slightly lower. These results clearly indicate the non-linear dependencies of the lift coefficient at $\alpha = 6°$ on the different strake parameters.

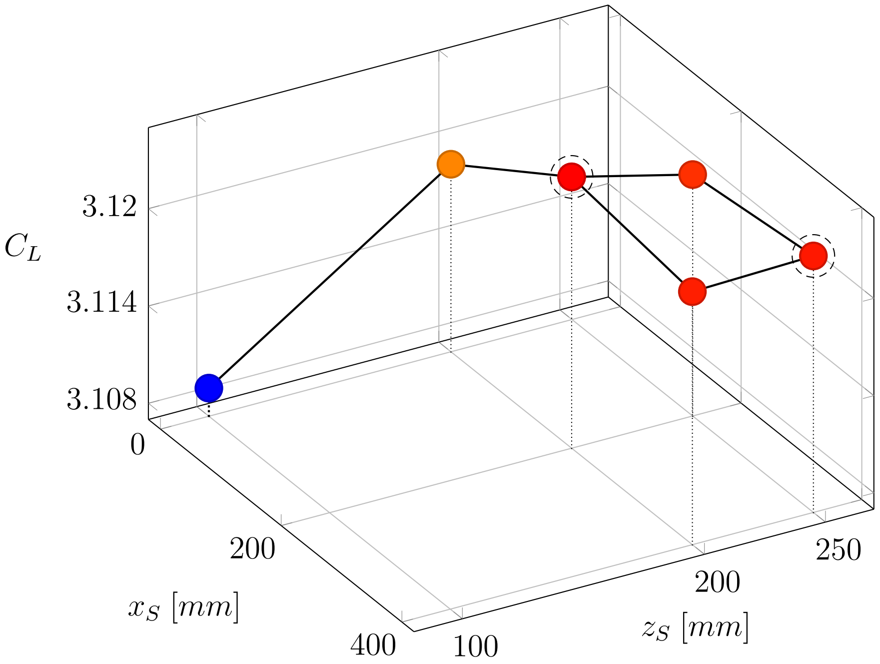

Figure 5.23: Influence of simultaneous position variations and $\mathbf{h_S = 2.67}$ on $\mathbf{C_L}$ at $\boldsymbol{\alpha = 6°}$

In the following, the strake configurations are examined at α_{max}. Since a complete lift curve needs to be generated for this purpose, the computational effort per configuration is quite high. Therefore, we will firstly concentrate on these two configurations that show the best results at $\alpha = 6°$ and which are marked in the figure.

5.4.3 Investigation of selected Strake Configurations at α_{max}

The lift curves of the strake configurations with $x_S = 200\ mm$, $z_S = 200\ mm$, $f_S = 8.0$ and $h_S = 2.67$ as well as with $x_S = 400\ mm$, $z_S = 250\ mm$, $f_S = 8.0$ and $h_S = 2.67$ are provided by Figure 5.24. In addition, the lift curve of the initial strake is depicted. As can be seen, the undertaken strake parameter changes do not allow for an increase of α_{max}. As well as in the case of the initial strake, $C_{L,max}$ is reached at $\alpha = 10°$. Nonetheless, we see that the modified strakes both result in a higher maximum lift coefficient than strake version 11-6S2. Hereby, the strake at $x_S = 200\ mm$ reaches $C_{L,max} \approx 3.278$ and the strake at $x_S = 400\ mm$ reaches $C_{L,max} \approx 3.265$ while configuration 11-6S2 is limited to $C_{L,max} \approx 3.260$. We can observe that the lift curves of the modified strakes are shifted to higher lift coefficients in the linear region. In addition, their slopes are slightly higher than the slope of the initial strake's lift curve. Until $\alpha = 8°$, they are of very similar values. However, as soon as stall occurs, a faster lift decrease can be observed for the strake at $x_S = 400\ mm$. In the area of post stall, C_L of this configuration even sinks below the value of the initial strake.

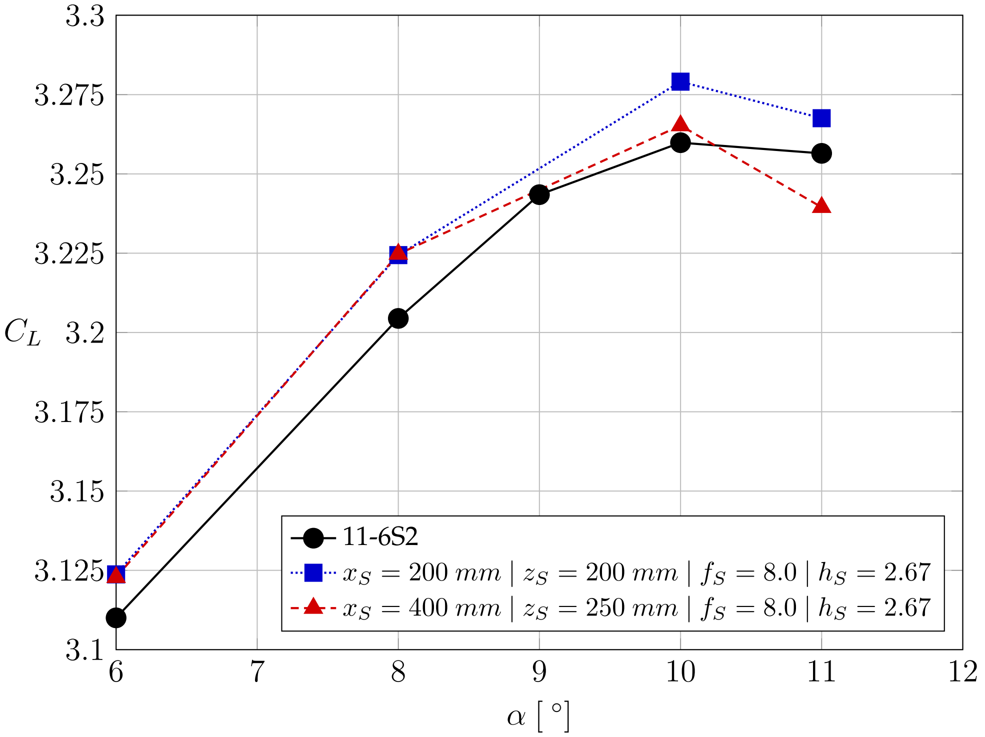

Figure 5.24: Lift curves of the most promising configurations according to $\boldsymbol{\alpha = 6°}$

In order to analyse the differences in detail with respect to the resulting flow field, Figure 5.25 shows the cutting planes at $x = 15.144\ m$, which represents a location on the flap behind the highest turning angle, as shown by Figure B.7 in the appendix. This location is chosen because the interaction between the nacelle vortex and the jet layer is already very distinct at this streamwise position. The cutting planes are coloured by the loss of total pressure, which reveals the vortices. As can be seen, the nacelle vortex is located at about 23% of the semispan. In contrast to this, the distribution of $c_{p,min}$ has indicated a nacelle vortex position at about 25% semispan (see subsection 5.4.2). This discrepancy arises from the high deflection of the vortex path across the highest turning angle, which can for instance be clarified by regarding Figure 5.10. 5.25(a) shows the vortices for the preferable strake at $x_S = 200\ mm$ and 5.25(b) unveils the vortices for the strake at $x_S = 400\ mm$. For reasons of clarity, the flap's surface is illustrated by the grey area.

It can be seen on the figures, that the nacelle vortex is still distinct in both cases. It interacts with the near surface flow layer and causes a gap in the high energy layer of active blowing, indicated by total pressure gain. This is supposed to occur since the vortex leads to a mixing of the high energy layer with low energy flow of the surrounding flow field. The total pressure loss near the core of the nacelle vortex for the strake at $x_S = 400\ mm$ is about 0.2% lower than in the case of the strake at $x_S = 200\ mm$. This suggests that the nacelle vortex for the strake at $x_S = 400\ mm$ is slightly weaker. The figure also gives an explanation why the strake at $x_S = 400\ mm$ results in a lower $C_{L,max}$. As can be seen, the associated loss of p_t in the core of the strake vortex ($x_S = 400\ mm$) is much higher This indicates that the vortex is too strong. An influence on the jet layer of the strake vortex itself can be observed. At $y/s \approx 0.25$, a reduction of the jet layer is visible that is likely to be caused by the sidewash of the strong strake vortex. On the contrary, due to its weaker nature, the vortex shed by the strake at $x_S = 200\ mm$ seems to have very little influence on the high energy layer itself. This supposed difference in strength of the two strake vortices is most likely caused by the streamwise strake position. As a consequence of the proximity to the wing and its circulation field, the lift generation of the strake at $x_S = 400\ mm$ rises disproportionately at high angles of attack, which results in a too strong vortex and a faster lift decrease.

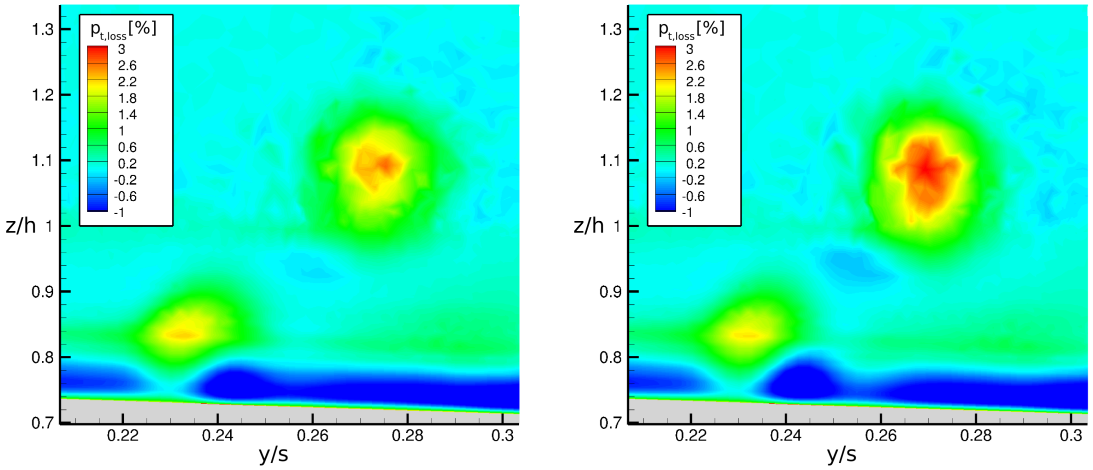

(a) Strake at $\mathbf{x_S = 200\ mm}$ and $\mathbf{z_S = 200\ mm}$ (b) Strake at $\mathbf{x_S = 400\ mm}$ and $\mathbf{z_S = 250\ mm}$

Figure 5.25: Best strakes (of $\alpha = 6°$): Cut at $\mathbf{x = 15.144\ m}$ revealing $\mathbf{p_{t,loss}}$ at $\alpha = 10°$

According to the results of these strakes, we can assume that a strake position of $x_S = 400\ mm$ is not suitable in our case. Therefore, we will continue the parameter study, using the strake with the parameters $x_S = 200\ mm$, $z_S = 200\ mm$, $f_S = 8.0$ and $h_S = 2.67$. However, we have observed that this strake is not yet able to reduce the nacelle vortex sufficiently. Therefore, further modifications will be examined in the following.

Further Variation of Geometry

One option to further optimise the strake is a modification of geometry. As seen in 5.25(a), the vortex shed by the strake at $x_S = 200\ mm$ and $z_S = 200\ mm$ is not very strong and its influence on the nacelle vortex is relatively low. Therefore, two different strake configurations with an increased strake area are examined with respect to $C_{L,max}$ in the following. On the one hand, the strake root chord and semispan are again increased by 33% each, resulting in a strake size factor of $f_S = 14.34$. In addition, a further increase of the root chord-semispan ratio is realised. Therefore, the root chord is enlarged to $c_{S,root} = 3.5 \cdot s_S$. Due to the limited space upstream, this root chord is symmetrically enlarged to both sides. In order to gain a better understanding of the modified strakes, Figure B.9 in the appendix can be regarded.

The resulting lift curves of the modified strakes are represented by Figure 5.26. As can be observed, none of the geometry modifications is capable of increasing the maximum lift coefficient. Nevertheless, the lift curves give some further understanding of the effect of an increase of the size factor. Apparently, a higher size factor shifts the lift curve to higher C_L in the area of the linear dependency on α. The differing lift coefficient values at $\alpha = 6°$ suggest that an approximately linear relation exists between C_L and

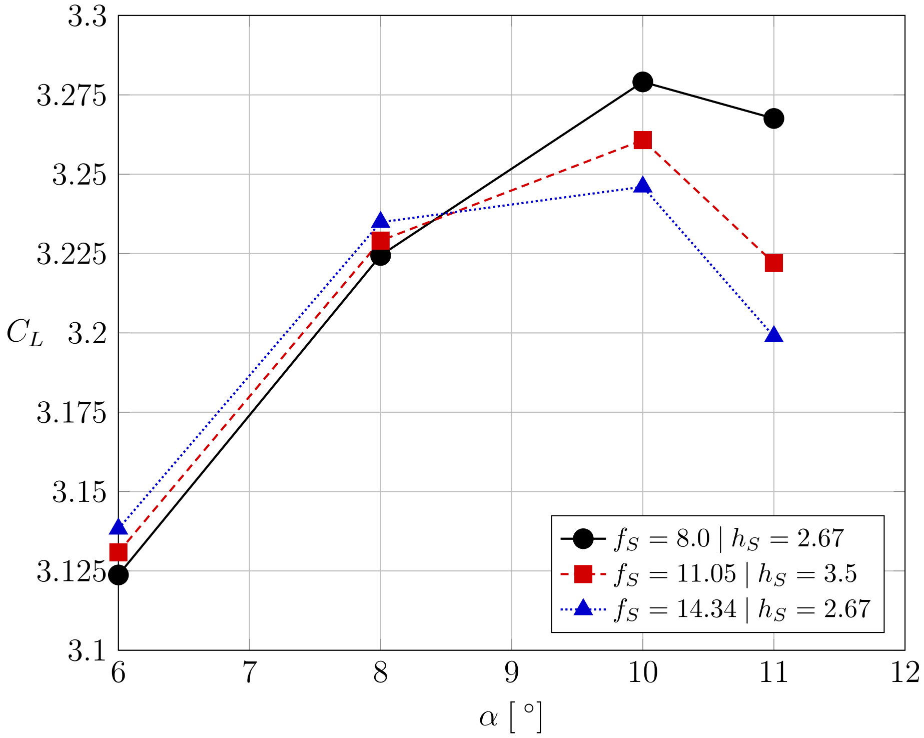

Figure 5.26: Lift curves due to geometry variations, $\mathbf{x_S = 200\ mm}$ and $\mathbf{z_S = 200\ mm}$

f_S. However, the closer we get to α_{max}, the faster C_L decreases for higher size factors. This indicates that the modified strakes are too big. Due to the high strength of the vortices at high angles of attack, their interaction with the jet layer becomes too strong and separation is thus forwarded.

In summary, neither the strake with $f_S = 14.34$ nor the one with $h_S = 3.5$ are able to achieve further improvements of $C_{L,max}$. In order to further increase the maximum lift coefficient, further changes of position thus need to be examined.

However, with $C_L \approx 3.138$ at $\alpha = 6°$, the biggest strake leads to an increase of about $1.5\ LC$ at this α. At this point of the lift curve, the strake apparently shows a very good performance with respect to the reduction of the nacelle vortex. In order to gain an understanding of the detailed flow conditions, we examine this case in detail. 5.27(a) shows the cutting plane at $x = 15.144\ m$. We can directly recognise that the inboard nacelle vortex has nearly completely vanished. The total pressure loss in its core is reduced to $p_{t,loss} \approx 1\%$. As a consequence, the jet layer below the nacelle vortex is indeed weakened but it is continuous, which represents an improvement compared to the results seen before. In addition, it is observable, that the strake vortex has an influence on the jet layer. At $y/s \approx 0.255$ a local decrease of the layer thickness is visible. However, its positive effects prevail. This suggests that a complete negation of the nacelle vortex is only possible in combination with an impact of the strake vortex on the high energy layer. Hence, a compromise between these two effects needs to be made. The distribution of suction peaks on the flap reflects the positive outcome of the strake. The wave-like pattern indicating the nacelle vortex is hardly visible. The distribution of $c_{p,min}$ is relatively homogenous in the inboard area without having any extreme values.

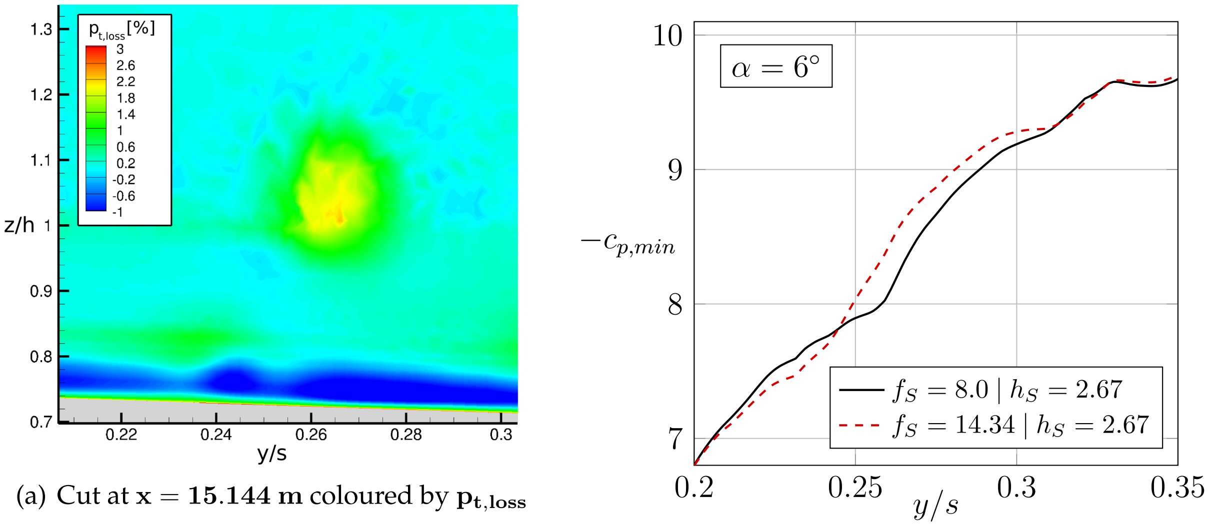

(a) Cut at $\mathbf{x = 15.144\ m}$ coloured by $\mathbf{p_{t,loss}}$

(b) $c_{p,min}$-distribution on the flap

Figure 5.27: Effects of a further strake size increase at $\boldsymbol{\alpha = 6°}$

In the following, we will assume that the behaviour, that the strake with $f_S = 14.34$ showed at $\alpha = 6°$ is near the optimum. Within the further parameter variation and optimisation process, it will therefore be the goal to obtain an approximately similar behaviour at α_{max}.

Further Variation of Position

As it has turned out, a further increase of the strake area has had a negative effect on $C_{L,max}$. In addition,the streamwise strake position has already been investigated extensively. Therefore, further variations of the vertical strake position can be evaluated. In doing so, we will concentrate on an increase of z_S. This is also in accordance with the results, obtained at $\alpha = 6°$, which has suggested that higher lift coefficients beyond $z_S = 250\ mm$ might be possible. Thus, positions of $z_S = 250$, 300, 350 and $400\ mm$ are regarded.

Figure 5.28 shows the distribution of $C_{L,max}$ for different z_S. As shown, a displacement in z-direction leads to a slight augmentation of the maximum lift coefficient. The maximum of $C_{L,max} \approx 3.282$ is reached with a strake at $z_S = 300\ mm$. This imports an additional increase by about $0.3\ LC$. At vertical strake positions of $z_S > 400$, the distribution again drops significantly. It can be supposed that the maximum at $z_S = 300\ mm$ represents the best compromise between an interaction of the strake vortex with the nacelle vortex and the interaction with the jet layer. Beyond this position, the nacelle vortex is less weakened. As a consequence, the distribution thus drops stronger than below $z_S = 300\ mm$.

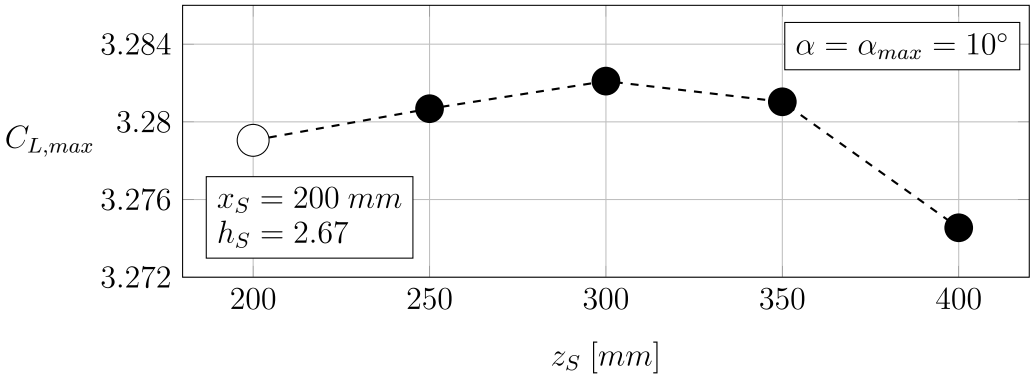

Figure 5.28: Influence of further variations of $\mathbf{z_S}$ on $\mathbf{C_{L,max}}$

To conclude, the investigations show that the most promising strake with respect to $C_{L,max}$ is located at $x_S = 200\ mm$ and $z_S = 300\ mm$ and disposes of a size factor of $f_S = 8.0$ and a root chord-semispan ratio of 2.67. In a final step, it will be examined, if a modification of the strake geometry, in contrast to the case of the strake at $x_S = 200\ mm$ and $z_S = 200\ mm$, allows for another increase of $C_{L,max}$ at this position.

5.4.4 Optimisation of the Strake in order to maximise the Maximum Lift Coefficient

Up to now, we have mainly focussed on the positioning problem of the strake. With the exception of the adaption of h_S within the first step of this study, the geometry has not been modified. For this reason, this section centers around a final increase of the strake area.

Final Improvement of the Strake Geometry

Therefore, the area of the strake will be increased stepwise. Hereby, both root chord and semispan are increased consecutively by 10%. Thereby, the strake size factors of $f_S = 9.68$, 11.55, 13.59 and 16.55 are obtained. The resulting strakes are depicted in Figure B.10 in the appendix.

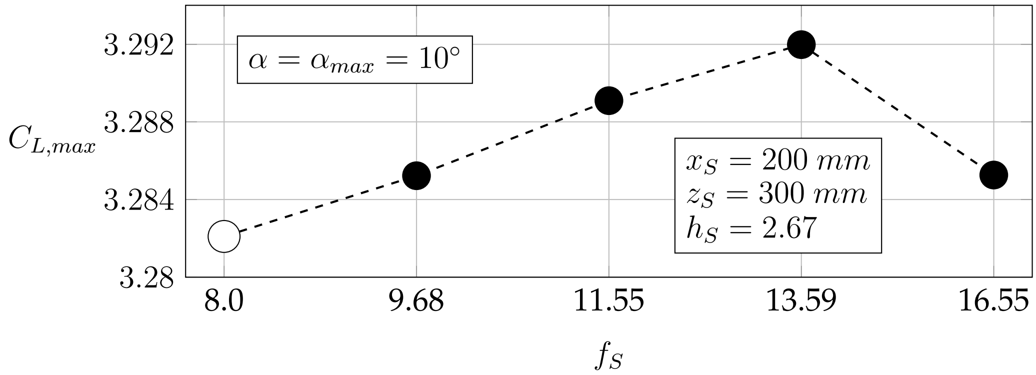

Figure 5.29: Impact of final optimisation of geometry by variation f_S on $\mathbf{C_{L,max}}$

Figure 5.29 shows the resulting distribution of the maximum lift coefficients along with the size factors. It is characterised by an approximately linear slope up to the maximum of $C_{L,max} \approx 3.292$ at $f_S = 13.59$. Thus, an increase of $\Delta C_{L,max} \approx 1\ LC$ can be achieved by the final optimisation of the geometry. Figure 5.30 unveils the nature of these improvements. It depicts the cutting planes at $x = 15.144\ m$ both for the strake configuration at $x_S = 200\ mm$ and $z_S = 300\ mm$ before and after the geometry modification. Basically, three changes can be observed. Firstly, due to the higher strake semispan, the vortex path is slightly shifted to lower y/s. While the vortex of the strake with $f_S = 8.0$ is about 27.5% of the wing semispan, the new strake vortex is located at about 26.5%. Secondly, it passes the wing a little higher. This effect can be explained by 5.31(b), which provides a front view of the final strake. As a consequence of the high vertical position of the strake, it is mounted at a position of the nacelle with higher rotundity. Since it is placed normal to its contours, the strake is therefore mounted with a small positive dihedral. Hence, the increase of the strake semispan is also accompanied by a higher shedding position of the vortex. As a result of the displacement in y and z-direction, the strake vortex has a different relative position with respect to the nacelle vortex and has therefore a higher capability of weakening it. Thirdly, thanks to the higher strength of the strake vortex, its influence on the nacelle vortex is much bigger

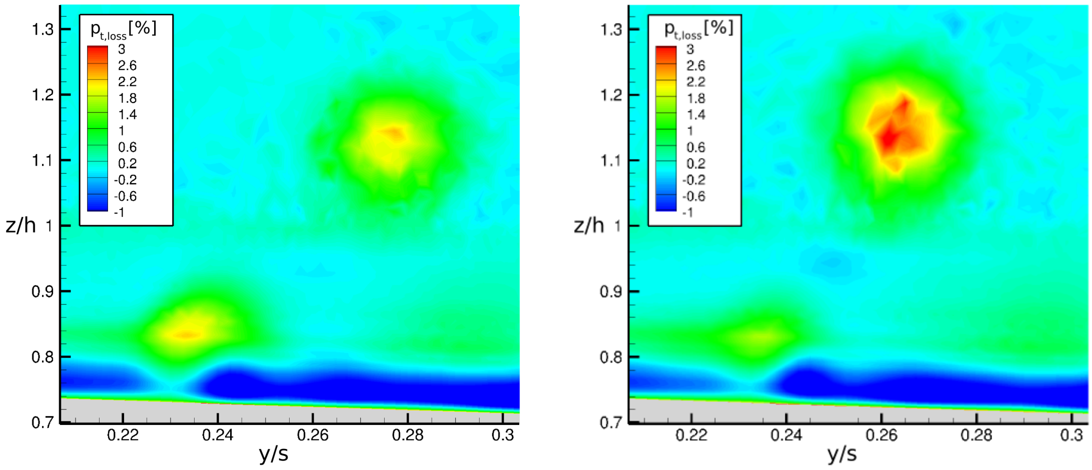

(a) Strake with $\mathbf{f_S = 8.0}$ (b) Strake with $\mathbf{f_S = 13.59}$

Figure 5.30: Final configurations: Cut at $\mathbf{x = 15.144\ m}$ revealing $\mathbf{p_{t,loss}}$ at $\boldsymbol{\alpha} = \mathbf{10°}$

than before the size modification. In accordance with these changes, we can observe that the nacelle vortex is much weaker and the gap inside the jet layer is also reduced. However, due to its higher distance to the surface, the influence of the strake vortex on the jet layer is similar to the case before the geometry modification.

Finally, we can summarise that the behaviour of the strake with $x_S = 200\ mm$, $z_S = 200\ mm$, $f_S = 14.34$ and $h_S = 2.67$ at $\alpha = 6°$ cannot completely be reproduced with this strake at α_{max} but the qualitative conditions are very similar.

Optimised Strake 11-6S3

Within this nacelle strake parameter study, the strake with the parameters $x_S = 200\ mm$, $z_S = 300\ mm$, $f_S = 13.59$ and $h_S = 2.67$ has been proven to be the best strake with respect to the maximum lift coefficient. With $C_{L,max} \approx 3.292$ its utilisation leads to a supplementary lift recovery of about $3.2\ LC$ compared to the initial strake and about $17\ LC$ relative to the case without strake. However, an increase of α_{max} compared to configuration 11-6S2 could not be obtained.

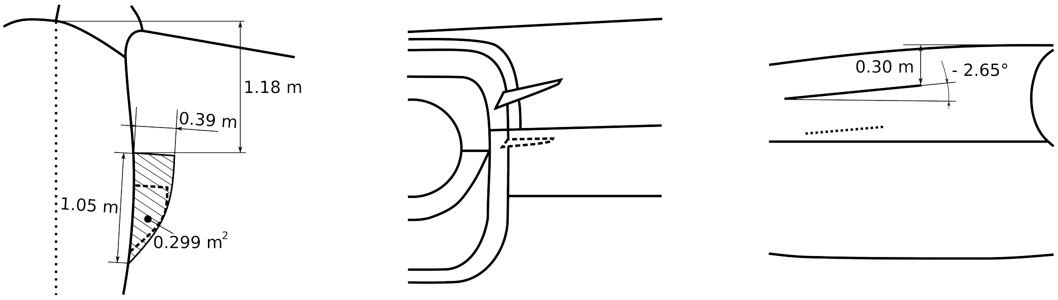

(a) Top view (b) Front view (c) Side view

Figure 5.31: Geometry and dimensions of the final strake 11-6S3

The modified strake is depicted in Figure 5.31. It is mounted with a setting angle of $\alpha_S = -2.65°$. It disposes of a strake root chord of $c_{S,root} = 1.05\ m$ and of a semispan of $s_S = 0.39\ m$. As a result, it has a strake area of $0.299\ m^2$.

6 Analysis of the Results

In the previous chapter, an increase of the maximum lift coefficient could be achieved by the new strake configuration 11-6S3, which has been optimised within three consecutive steps. In this chapter the nature of these improvements shall be outlined and the optimised strake's effects on the flow field shall be discussed in detail. First of all, the resulting lift curve of configuration 11-6S3 is presented by 6.1(a). In addition, the lift curves of configuration 11-6, which does not possess strake, and configuration 11-6S2, containing the initial strake, are shown. As already mentioned, the optimised strake leads to an increase of $C_{L,max}$ by around 17 LC compared to the case without strake and by roughly 3.2 LC compared to the configuration with the initial strake. Thereby, maximum lift is reached at $\alpha_{max} = 10°$, which is equivalent to configuration 11-6S2. This denotes an increase of α_{max} by $2°$ compared to configuration 11-6. However, another change of the lift curve can be observed. The augmentation of lift is primarily obtained through an increase of the slope $C_{L\alpha}$ compared to configuration 11-6S2 whose lift curve itself has a higher slope than the lift curve of configuration 11-6. This can likely be explained by the new strake's higher area. The strength of the vortex increases more rapidly along with the angle of attack and has therefore a better capability of weakening the nacelle vortex near α_{max}. 6.1(b) shows the spanwise distribution of the section lift coefficient at α_{max} and at post-stall angles of attack. As shown, c_l in the region of both nacelle vortex and strake vortex, which is to be found at

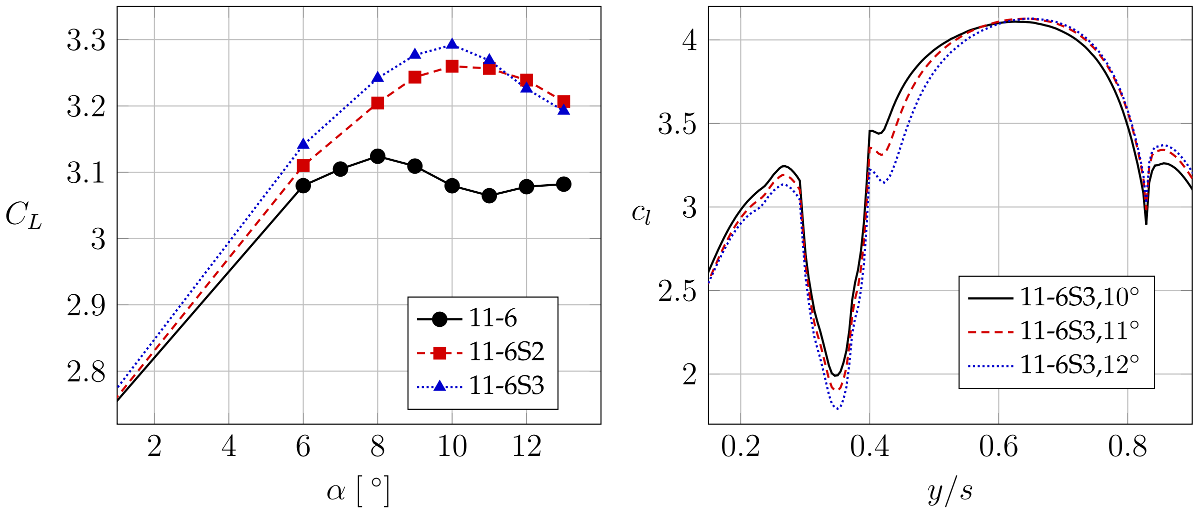

(a) Lift curve

(b) Spanwise distribution of $\mathbf{c_l}$

Figure 6.1: $\mathrm{C_L}$-characteristics of configuration 11-6S3

around 20% to 30% of the wing semispan, declines only in a moderate way at $\alpha > 10°$. Nevertheless, it can be seen that c_l beyond about 60% wing span still increases at these angles of attack. This indicates that the vortices still have a slight impact on the lift coefficient. However, the main lift loss arises from the region of the outboard nacelle vortex at $y/s \approx 0.44$. This circumstance will be analysed at the end of this chapter. In the following, we will concentrate on the solution at $\alpha = 10°$ since it is the most interesting case in order to analyse the strake's impact on $C_{L,max}$.

The foregoing parameter study has shown that the strake design underlies particularly a compromise between the most effective weakening of the nacelle vortex and the least interaction of the strake vortex itself with the flow close to the surface. Therefore, the improvement obtained thanks to the optimised strake can basically be explained by two circumstances. First of all, the strake vortex is located at a better y and z-position relative to both the nacelle vortex and to the aircraft's surface and secondly, its strength is adjusted. The consequences of these circumstances will be outlined in the following.

In order to understand the improvement due the position change of the strake vortex, Figure 6.2 shows the cutting planes at $x = 15.144\ m$, coloured by $p_{t,loss}$, for the initial strake configuration and for configuration 11-6S3. It can be seen that the total pressure loss for the optimised strake is significantly smaller than for the initial strake, which indicates that the nacelle vortex is much weaker. However, the most important matter that can be observed on these figures is the different location of the strake vortex paths. Due to the different propagation of the two vortices across the wing, the distance between them change along the vortex paths. Nevertheless, since the nacelle vortex most effects the flow near the flap trailing edge, the relative location of the vortices in this region is most important. As shown by 6.2(a) the strake vortex shed by the initial strake is closer to the flap's surface than to the nacelle vortex. As a consequence, both the flow close to the surface and the nacelle vortex are likewisely affected by the strake vortex. A further increase of the strake area therefore has a negative effect on $C_{L,max}$. On the contrary, the strake vortex shed by configuration 11-6S3, as shown by 6.2(b), is

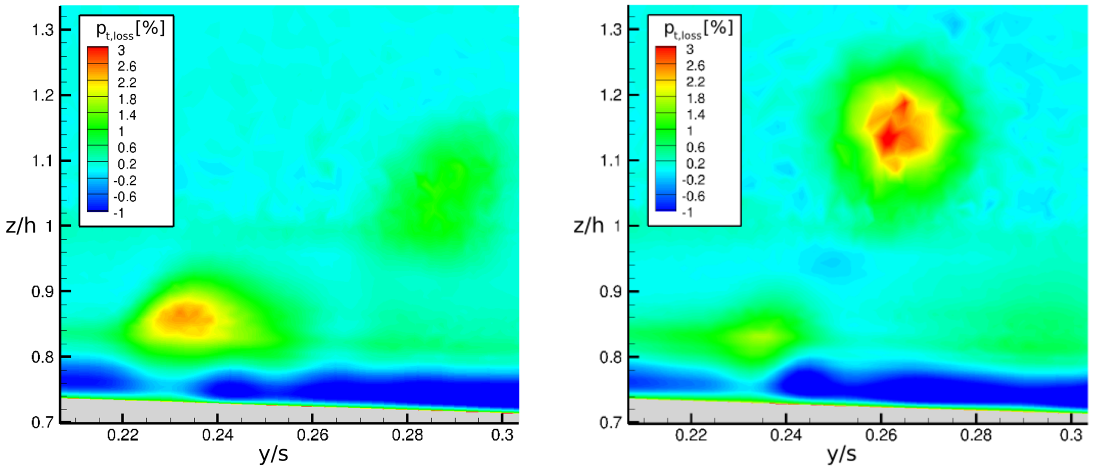

(a) Configuration 11-6S2

(b) Configuration 11-6S3

Figure 6.2: Cut at $\mathbf{x = 15.144\ m}$ revealing $\mathbf{p_{t,loss}}$ for 11-6S2 and 11-6S3 at $\boldsymbol{\alpha = 10°}$

located at a higher vertical position and is furthermore shifted to a smaller y/s. Hence, it primarily affects the nacelle vortex and has less impact on the jet layer. In spite of its significantly higher strength due to the larger strake geometry, which is indicated by the higher total pressure loss, its interaction with the flow close to the surface is small.

The impact of the adaption of the strake area size and thereby the influence of the shed vortex on the loss is illustrated by Figure 6.3. Here, cutting planes for three strakes from the last optimisation step of the foregoing parameter study are presented and coloured by $p_{t,loss}$. Since the differences are very small, the cutting planes are set at $x = 15.26\ m$, which is just before the flap's trailing edge, as can be verified on Figure B.7 in the appendix. Here, the differences are at least recognisable. 6.3(b) shows the distribution of $p_{t,loss}$ for the optimised strake configuration 11-6S3. The other strakes are located at the same position and have size factors of $f_S = 11.55$, as shown by 6.3(a), and $f_S = 16.55$, illustrated in 6.3(c). As can be recalled in Figure 5.29, these are the strakes that lead to a slightly lower $C_{L,max}$ than the optimised strake. On the one hand, it can therefore be assumed that the strake with $f_S = 11.55$ weakens the nacelle vortex less than the optimised strake. On the other hand, the strake with $f_S = 16.55$ is already too large and has thus a negative influence on the surface flow. This shall be surveyed in the following. We observe that the loss, caused by the nacelle vortex, is the highest for $f_S = 11.55$ and the flow field is also characterised by the largest gap inside the jet layer. As a consequence, the negative effect caused by the stronger nacelle vortex prevails. The $p_{t,loss}$-distribution of the strake with $f_S = 16.55$ hardly differs from the one of the optimised strake. However, it can be seen that the insection inside the jet layer at $y/s \approx 0.25$ is a little deeper than in the case of the optimised strake.

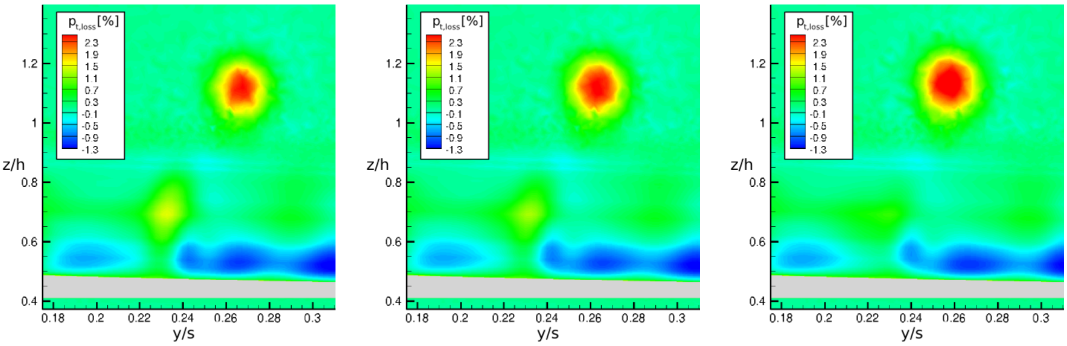

(a) Strake with $\mathbf{f_S = 11.55}$ (b) Strake with $\mathbf{f_S = 13.59}$ (c) Strake with $\mathbf{f_S = 16.55}$

Figure 6.3: Cut near flap trailing edge at $\mathbf{x = 15.26}$ revealing $\mathbf{p_{t,loss}}$ at $\boldsymbol{\alpha} = \mathbf{10}^\circ$

However, the higher $p_{t,loss}$ only indicates the lower maximum lift coefficient. In order to understand the direct impact of the differences of vortices on lift, the pressure coefficient can be regarded. Figure 6.4 shows the differences in the surface pressure coefficients of the above mentioned configurations. Thereby, 6.4(a) shows a Δc_p, obtained by c_p of the strake with $f_S = 11.55$ minus c_p of the optimised strake 11-6S3. Thus a positive Δc_p signifies a lower $|c_p|$ caused by the strake with $f_S = 11.55$ and thus a degradation compared to strake configuration 11-6S3. The frame contains the rear part of the main wing and the flap. It should be noted that Δc_p is highly resolved since the differences are very small. It can be observed that the values of $|c_p|$ are decreased on the left side of the flap for the strake with $f_S = 11.55$. This occurs in the region the nacelle vortex path passes. This is in accordance with the above made observance that the nacelle vortex is stronger for this case. Another difference can be seen. The weaker strake vortex of the strake with $f_S = 11.55$ seems to strengthen the outboard nacelle vortex less than the strake vortex of configuration 11-6S3. This can be observed by the region flooded with blue colour on the right side of the flap. However, the impact of this effect on c_p is relatively small compared to the increase of the pressure coefficient due to the weakening of the nacelle vortex. The altogether lower values of $|c_p|$ then result in a lower $C_{L,max}$. 6.4(b) shows the surface pressure coefficient differences, calculated according to $\Delta c_p = c_{p,f_S=16.55} - c_{p,f_S=13.59}$. The resulting distribution of c_p again confirms the assumptions. As can be seen, the stronger strake vortex results in a large area of reduced $|c_{p,min}|$. This occurs particularly at the wing trailing edge. It apparently

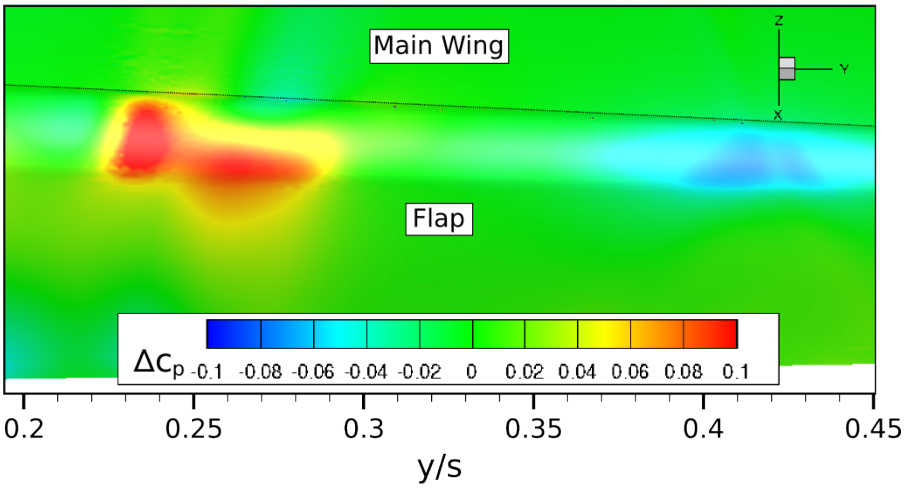

(a) Surface pressure coefficient difference $\mathbf{\Delta c_p = c_{p,f_S=11.55} - c_{p,f_S=13.59}}$

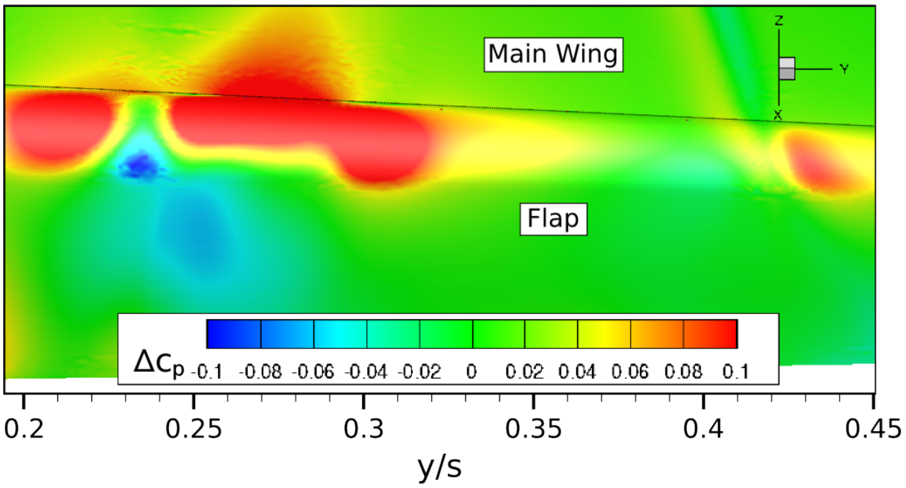

(b) Surface pressure coefficient difference $\mathbf{\Delta c_p = c_{p,f_S=16.55} - c_{p,f_S=13.59}}$

Figure 6.4: Differences in the surface pressure coefficient $\mathbf{\Delta c_p}$ at $\boldsymbol{\alpha} = \mathbf{10}^\circ$

also has an impact on the region on the left hand side of the nacelle vortex. However, it can also be observed that $|c_{p,f_S=16.55}| > |c_{p,f_S=13.59}|$ is true in the region of the nacelle vortex. This signifies that, the further weakening of the nacelle vortex results in a local lift recovery. However, the negative impact on the c_p-distribution prevails. The higher amount of positive values of Δc_p for this strake compared to the strake with $f_S = 11.55$ also explains the lower $C_{L,max}$, obtained with this strake. In accordance with the weaker outboard nacelle vortex for the strake with $f_S = 11.55$, the outboard nacelle vortex is strengthened here. To conclude, the optimised strake represents the best compromise between both effects and thus leads to the highest $C_{L,max}$. It should be noted that the enlargement of the strake geometry by f_S does not exclusively result in a higher strength of the shed vortex but also leads to a slight displacement of the strake vortex to lower y/s. Therefore, the changes of $C_{L,max}$ can not solely be attributed to the strengthening of the strake vortex. Finally, the differences of the maximum lift coefficients of these configurations are in a range of around $0.7\ LC$. This demonstrates that the final lift recovery is only obtained by a slight reduction of $p_{t,loss}$ whereas a compromise between the interaction of the strake vortex with the jet layer and with the nacelle vortex has to be made. The flow phenomena do not change at all.

Figure 6.5 shows the shedding of inboard and outboard nacelle vortex as well as of the strake vortex in the region of the droop nose-nacelle intersection at $\alpha = 10°$. Hereby, a comparison between configuration 11-6S2, shown by 6.5(a), and configuration 11-6S3, illustrated by 6.5(b), is given. The vortices are illustrated by means of Iso-Surfaces at the constant values of the kinematic vorticity number $\omega_k = 1.2$, 1.5 and 2.0. The blue colour of the inboard nacelle vortex and the strake vortex signifies the sense of rotation along the negative x- direction. The differences between the two configurations are

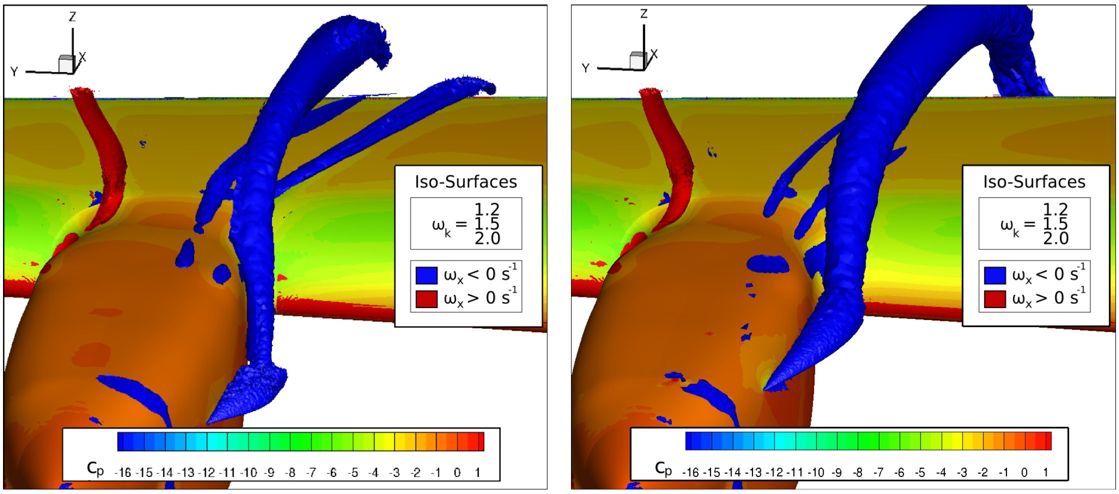

(a) Configuration 11-6S2 (b) Configuration 11-6S3

Figure 6.5: Shedding of vortices in the junction area at $\boldsymbol{\alpha = 10°}$

clearly visible. The strake vortex of configuration 11-6S3 is characterised by a bigger size, indicating the higher strength, and a higher vortex path, which is in accordance with the observations made before. Both the strake vortex shed by the initial strake and by the optimised strake lead to a splitting of the inboard nacelle vortex. However, in case of configuration 11-6S2, it is observable that the main part of inboard nacelle vortex is still existent at the passage between wing and flap. The secondary part has nearly vanished there. On the contrary, we can see that the optimised strake results in a strong reduction of both parts of the inboard nacelle vortex. From about 50% of the local chord length on, the nacelle inboard vortex is not visible any more. This does not exactly signify that it is not existent any more, but it implies that its strength has decreased significantly so that it does not fulfill the criteria of the Iso-Surfaces any more. The low strength of the nacelle vortex is also reflected by the pressure coefficient the surface is coloured with. This figure gives an insight to another favorable consequence of the strake optimisation. As can be seen on 6.5(a), the inboard nacelle vortex and the strake vortex pass the wing with a different deflection angle in the xy-plane. This can be best illustrated if the vortex paths are projected on the wing's surface. In case of the initial strake vortex, the vortex path of the strake vortex already crosses the one of the nacelle vortex behind the droop nose. Hence, the influence of the strake vortex on the nacelle vortex starts to decrease beyond this point. As already shown, the strake parameter modification leads to a shift of the strake vortex path to smaller y/s. Therefore, it crosses the nacelle vortex path at a higher streamwise position. As a result, the average distance between the two vortex paths is reduced. In combination with the higher strength of the strake vortex, this leads to a more effective reduction of the inboard nacelle vortex, already before the flap is reached.

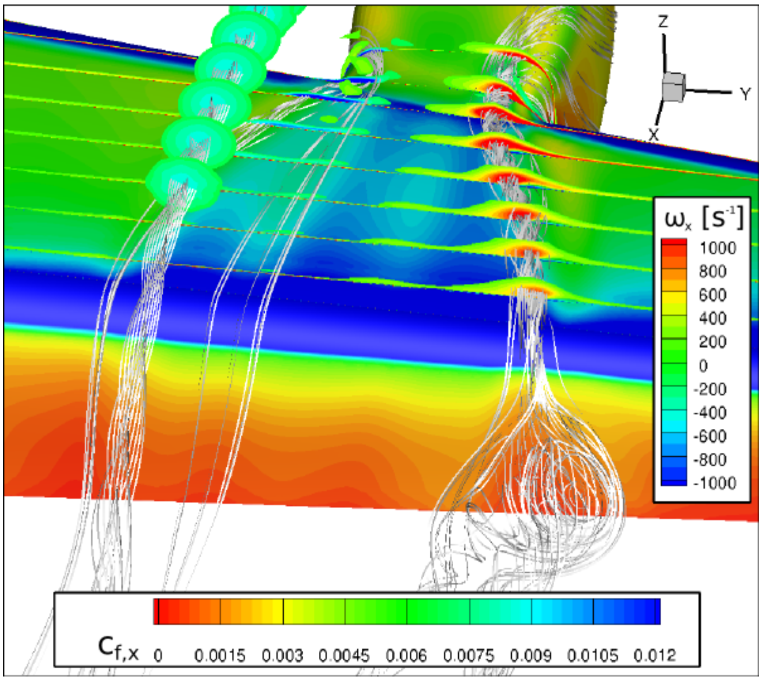

Figure 6.6: Nacelle and strake vortex propagation of configuration 11-6S3 at $\alpha = 10^\circ$

These observations are also reflected by Figure 6.6, which shows streamtraces, applied to the vortices, as well as the skin friction coefficient $c_{f,x}$ and the vorticity in x-direction for configuration 11-6S3. We can again see that the inboard nacelle vortex is weakened considerably. This is characterised by the low values of ω_x, illustrated by the slices and the low rotational movement of the streamtraces. Nevertheless, the skin friction coefficient at the flap trailing edge shows an extended region around the inboard nacelle vortex with values near zero. This is likely to be explained by the fact, that this vortex is indeed very faint but still existent. Therefore it weakens the local jet layer and reduces $c_{f,x}$. However, the streamtraces illustrate that there is no off-the-surface separation present and that the flow in the wake is still attached. On the contrary, the figure shows that the outboard nacelle vortex also starts to become critical at $\alpha = 10°$. While this vortex only had a minor impact on the flow on the flap at $\alpha = 8°$, as can be recalled by section 5.3, it here leads to an off-the-surface separation in the wake. This wake burst is characterised by the irregular streamlines in this region. In addition, the skin friction coefficient still has values of $c_{f,x} > 0$, suggesting that the surface flow is still attached. This fact explains the local loss of c_l at $y/s \approx 0.44$, as shown in 6.1(b).

In order to analyse the effect of the outboard nacelle vortex in a more detailed way, Figure 6.7 shows the local distribution of $p_{t,loss}$ on a cutting plane at $x = 15.09\ m$. This is a location on the flap near the wing trailing edge. Additionally, the velocity vectors tangential to the plane are shown, using uniform lengths in order to provide a better clarity. The vectors are furthermore given relative to the vertical velocity of the vortex core. It can be observed that the outboard nacelle vortex, revealed by the velocity vectors, rotates along with the positive x-direction. It entrains low energy flow of the outer flow field and inserts it into the lower flow layers. Thereby, it weakens the jet layer. In addition, it creates a sidewash and thus shifts flow of the jet layer to the right-hand side, causing a loss of momentum. As a consequence of the reduced energy of the jet layer in this region, it is not capable to entrain the outer flow any more along the convex surface of the flap. Due to the very high turning angle, off-the-surface separation then occurs in the wake, while the surface flow still stays attached. To conclude,

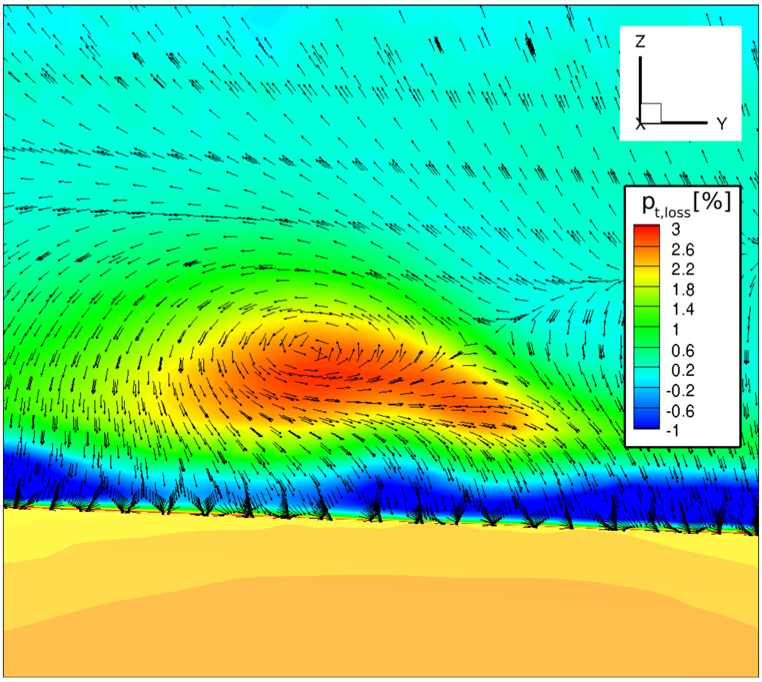

Figure 6.7: Total pressure loss due to outboard nacelle vortex, $\mathbf{x = 15.09\ m}$ and $\boldsymbol{\alpha = 10°}$

at higher angles of attack, the outboard nacelle vortex leads to the same negative effects in the flow field as the inboard nacelle vortex causes in the absence of the strake vortex. The loss caused by the outboard nacelle vortex is still small compared to the loss caused by the inboard nacelle vortex without strake, but at higher angles of attack, it increases clearly, as shown by 6.1(b). An outboard strake is very likely to achieve further improvements with respect to $C_{L,max}$. Thereby, a further increase of α_{max} can probably be obtained.

7 Strake Impact on the Cruise Configuration

In the foregoing chapters, the strake configuration 11-6S3 has been analysed and optimised with respect to its effects in the high lift configuration. In addition, its impact on drag during the cruise flight is determined within this chapter. Therefore, the clean configuration, described in section 3.2, becomes important. In the following, the grid generation process for this configuration as well as the underlying numerical setup for the calculations will shortly be outlined. Finally, the drag increase due to the utilisation of the new strake will be compared to both the configuration without and with the initial strake.

7.1 Grid Generation

Within the grid generation process for the cruise configuration, we refrain from the insertion of structured elements into the wing section. Since we are mainly interested in the additional drag, caused by the strake, rather than the precise resolution of local flow phenomena, we expect a proper refinement of the strake wake to be sufficient. In addition, due to the low angle of attack in cruise, the strake vortex and its influence on the flow field around the wing is supposed to be weak. Since no structured elements

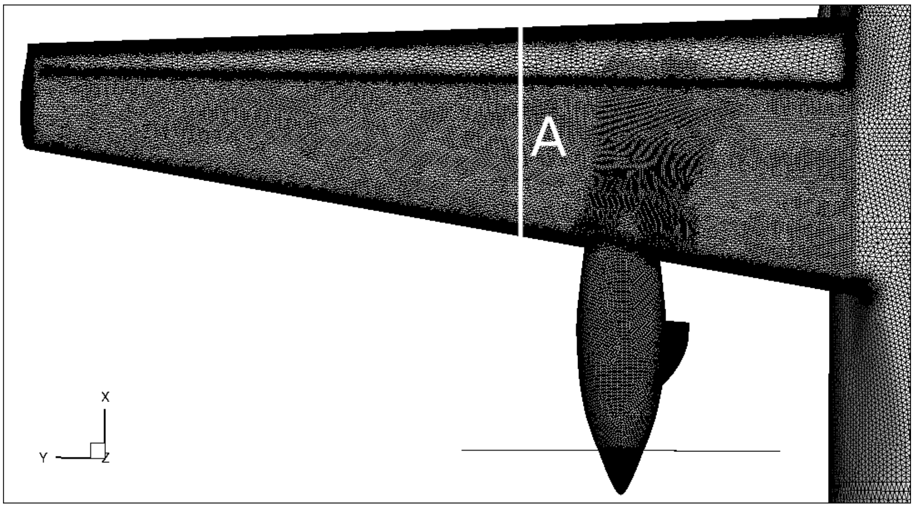

Figure 7.1: Complete surface grid of cruise configuration

are employed, the time-consuming repartioning process of the wing panels can also be omitted. The different grids are again constructed using modular grid generation. As already described in chapter 4, this does not only minimise the effort but also permits a better comparability. The detailed explanation of the modular grid generation is not given here, as it is performed in the same manner as described in chapter 4.

Figure 7.1 shows the surface grid of the cruise configuration, including the main zone and the module box. The underlying geometry contains the optimised strake 11-6S3. As shown, the grid cells are locally refined in the wake of the nacelle to account for the strake vortex. The surface grid of the fuselage is similar to the one of the high lift configuration and is thus not depicted for a better visibility. Cut A, shown in the figure, is depicted by Figure 7.2. It represents a cut, normal to the span-direction, that unveils the airfoil profile of the clean configuration. As can be seen, the slot is not modelled since there is no use for active blowing during the cruise flight. The cut also reveals the prism layers. The first prism layer thickness is again dimensioned in such a manner that $y^+ < 1$ is approximately ensured at every point. Due to the higher Reynolds number in cruise flight, the prism layer is thinner than in the case of the high lift configuration. For the complete wing 37 prism layers are used.

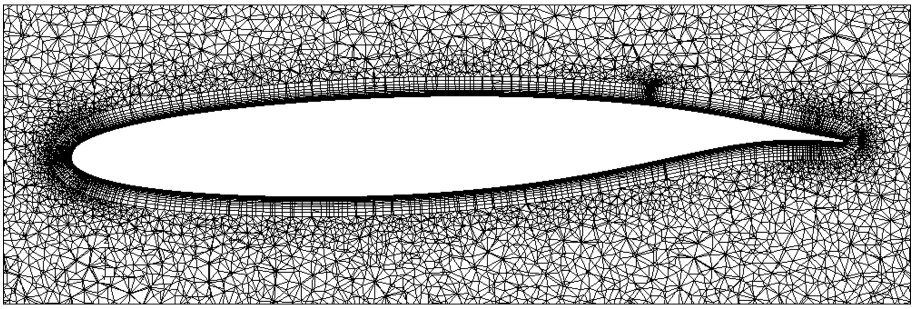

Figure 7.2: Cut A: Prism grid of airfoil section of cruise configuration

Zone	Main	Module box
Node points	$22.7 \cdot 10^6$	$1.8 \cdot 10^6$
Grid cells	$93.6 \cdot 10^6$	$4.6 \cdot 10^6$
Surface elements	$0.7 \cdot 10^6$	$0.1 \cdot 10^6$
Hexahedra, prisms and pyramids	$19.4 \cdot 10^6$	$3.1 \cdot 10^6$
Tetrahedra	$74.2 \cdot 10^6$	$1.5 \cdot 10^6$

Table 7.1: Grid statistics of cruise configuration

The overall grid statistic is summarised by Table 7.1. With altogether about 25 million node points and roughly 95 million grid cells, the grid of the cruise configuration contains considerably less elements than the high lift configuration.

7.2 Numerical Setup

The following calculations are performed at the beginning of the cruise flight. If the flight is operated at constant altitude and with constant velocity, $C_{L,cruise}$ changes constantly. Using the beginning of cruise, when the aircraft's weight is maximal and the angle of attack is highest, we ensure the determination of the maximal additional drag caused by the strake. It should however be noted, that the calculations are again performed without tailplane. An altitude of $10\ 600\ m$ is predetermined. The corresponding atmospheric values are obtained assuming a standard atmosphere. The Mach number is 0.74 and the Reynolds number is around 20 million. The underlying flight conditions are summarised in Table 7.2. The required lift coefficient at this point of the flight envelope is assumed as $C_L = 0.463$, which leads to an initial angle of attack of $\alpha \approx 3.66°$. As can be noted, this differs from the value that has been used in order to configure the strake setting angle α_S. There are mainly two reasons for this discrepancy. Firstly, we have used the average of α, assuming a constant velocity and constant altitude flight and secondly, the preliminary design data have been used in order to define the strake setting angle, which differs slightly from the actual version of the SFB 880 aircraft.

Mach number Ma	0.74	
Reference altitude H_0	$10\ 600$	m
Reference density ρ_0	0.38372	kg/m^3
Reference kinematic viscosity ν_0	$3.7436 \cdot 10^{-5}$	m^2/s
Reference temperature T_0	219.36	K
Reynolds number of incident flow Re_∞	$20 \cdot 10^6$	
Lift coefficient $C_{L,cruise}$	0.463	
Angle of attack α_{cruise}	≈ 3.66	$^\circ$

Table 7.2: Flight conditions at the beginning of cruise flight

The underlying numerical settings for the calculations of the cruise flight are very similar to those of the simulations of the approach. However, the calculations are performed under consideration of thrust. The load distribution on the actuator disk is thereby dimensioned in such a way that a thrust of $F = 13\ 960\ N$ is obtained, which signifies a balanced flight for this configuration. In addition, the calculations are performed at an angle of attack, defined by the target lift coefficient $C_{L,target} = 0.463$. This means that the corrresponding angle of attack is altered within the iteration steps until the desired lift coefficient is reached. Finally, $10\ 000$ iteration steps are processed in order to obtain a converged solution.

7.2.1 Convergence Behaviour

Figure 7.3 shows exemplarily the convergence behaviour of the calculations in the cruise configuration. It shows the courses of the aerodynamic coefficients C_L and C_D as well as the normalised density residual ρ_{res}/ρ_0 in case of the configuration without strake. Since the convergence behaviour of the other cruise calculations is similar, only this case will be discussed representatively. As can be seen, the solution converges fast to steady-state. The density residual ρ_{res} is reduced to less than 1% of the reference density ρ_0 within the first $3\ 000$ iterations. As can be observed, it further drops until it reaches an asymptote at about 0.2%. After about $2\ 000$ iteration steps the lift coefficient already reaches $C_{L,target}$ and oscillates around this value with a small amplitude. These high-frequency variations are then damped within the next $2\ 000$ iteration steps. Finally, the perturbations in C_D are damped to a minimum within the first $6\ 000$ iteration steps. As we have seen in case of the convergence behaviour of the high lift configuration, the values of the converged solution showed a repetitive oscillation around an average course. The amplitude of these oscillations were about $0.5\ LC$ for C_L and about $5\ DC$ for C_D. In this case, the order of these variations is by 10^{-2} lower as can be seen in Figure B.11 in the appendix.

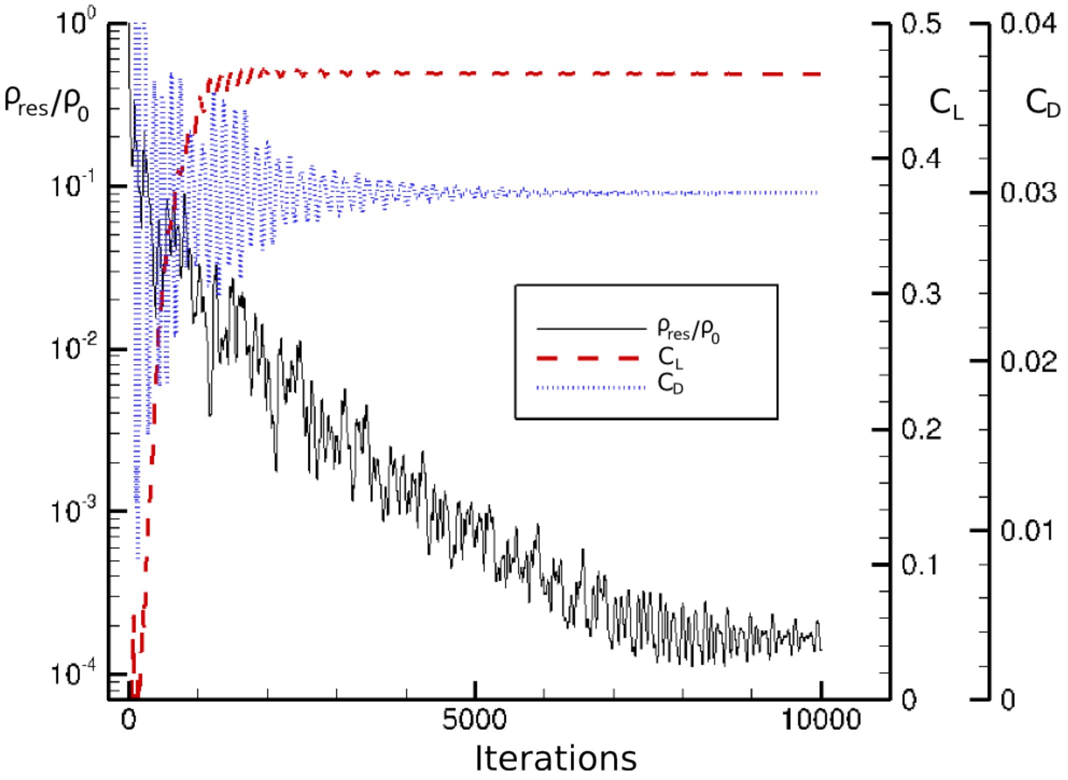

Figure 7.3: Convergence behaviour of the cruise configuration

7.3 Strake Influence on Drag

The positive effect of the optimised strake in the high lift configuration is naturally accompanied by a negative effect during the cruise flight. Since the foregoing nacelle strake parameter study included an enlargement of the strake area and of the strake setting angle, a drag increase is to be expected. In order to determine the strake's impact on C_D quantitavely, configuration 11-6S3 will in the following be compared to the configuration without strake and to configuration 11-6S2, containing the initial strake. In addition, the final strake of the second step, which has a strake size factor of $f_S = 8.0$ and is located at the same position as the optimised strake, will be considered. Since it also shows good results with respect to $C_{L,max}$ in combination with a significantly smaller area, it also represents a possible solution. Figure 7.4 shows the initial cruise drag coefficients for the different configurations. The aircraft without strake is subject to a drag coefficient of about 299.65 DC. As can be seen with a ΔC_D of about 0.34 DC, drag of configuration 11-6S2 is slightly higher. With about 300.08 DC, drag of configuration 11-6S3-fS=8.0 is again augmented by around 0.43. This is the result of the increase of the strake area and the setting angle. Finally, we can see that the additional enlargement of the strake size factor, as undertaken for configuration 11-6S3 has a strong influence on C_D. With about 300.31 DC, the optimised strake leads to a drag increase of about 0.66 DC. Table 7.3 summarises the drag increase in every case. As shown, the relative increase of the drag coefficient for configuration 11-6S3 amounts less than 0.25% of C_D of the sole aircraft without strake. In order to gain a better understanding of the nature of the drag increase, the table additionally shows the partial drag that occurs on the strake panel. Hereby, the partial drag on the panel is denoted as $\Delta C_{D,S}$. Since a strake can approximately be regarded as a flat plate and given the small strake angle of attack in cruise, it is supposable that friction drag is predominant in $\Delta C_{D,S}$. As documented by the table, the portion of $\Delta C_{D,S}$ is around 60% for

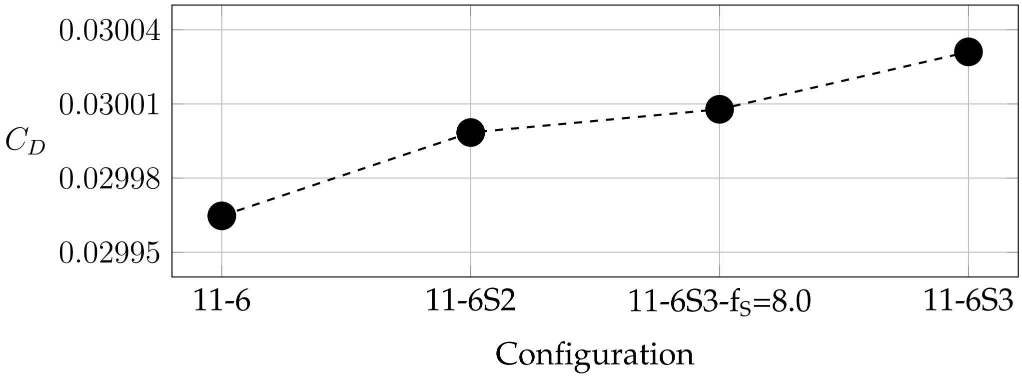

Figure 7.4: Strake impact on $\mathbf{C_D}$ during cruise flight

	11-6S2	**11-6S3-f$_S$=8.0**	**11-6S3**
ΔC_D	0.34 DC	0.43 DC	0.66 DC
$\frac{\Delta C_D}{C_{D,11-6}}$	0.112%	0.144%	0.222%
$\frac{\Delta C_{D,S}}{\Delta C_D}$	59.35%	45.01%	45.78%

Table 7.3: Components of drag increase due to different strake configurations

configuration 11-6S2. In contrast, both for configuration 11-6S3-fS=8.0 and for configuration 11-6S3, this portion only represents about 45% of the total drag increase. One of the main reasons for this might be the stronger strake vortex shed by the optimised strake and its influence on the flow field. Firstly, the increase of the strake root chord-semispan ratio results in a decrease of the strake aspect ratio, resulting in a stronger vortex. Secondly, the strake setting angle has been modified. The geometric strake angle of attack with respect to the oncoming flow of the initial strake is $\alpha \approx -1.3°$ while it is $\alpha \approx 1°$ in case of the newer strakes. The resulting higher lift generation again leads to an increase of the strength of the shed vortex. In addition, the strake position has changed. Especially due to the higher position of the strake, the strake vortex passes closer to the wing than the initial strake's vortex which again leads to an increase of drag. Figure 7.5 illustrates these issues. 7.5(a) shows the shedding of a relative weak vortex on strake 11-6S2 in cruise flight while 7.5(b) shows the vortex shed by the strake of configuration 11-6S3. The vortices are revealed by multiple slices, coloured by the vorticity in x-direction ω_x. It should be noted that especially due to high shear inside the boundary layer, the near surface flow is represented by blue colour which is equivalent to the core of the vortices. However, it can be seen that the vortex shed by the optimised strake during cruise flight is clearly stronger than the strake vortex shed by the strake of configuration 11-6S2. In addition, it can be observed that it strikes the wing leading edge and gets split while one part passes the wing on the upper and the other passes it on the lower side. On the contrary, the strake vortex of configuration 11-6S2 passes the wing solely on the lower side.

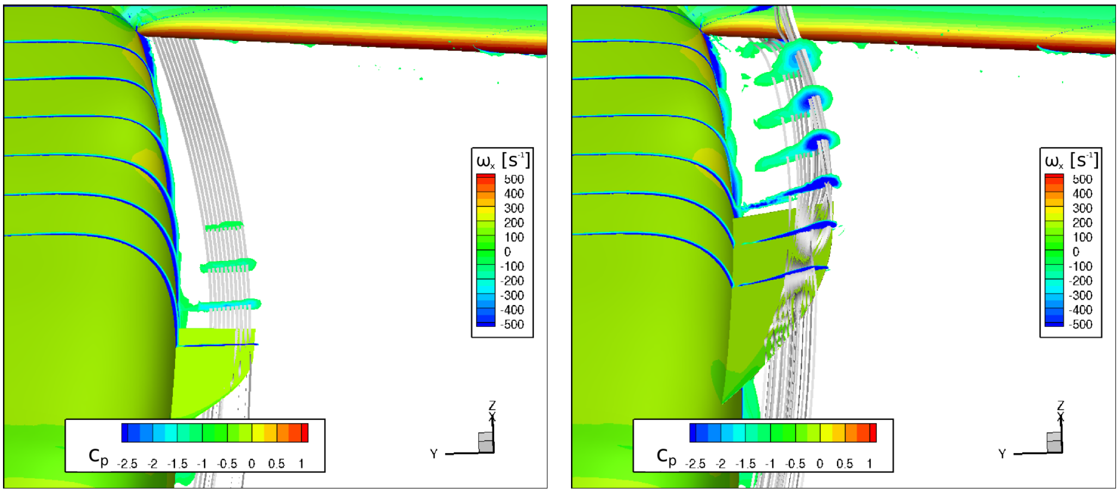

(a) Configuration 11-6S2 (b) Configuration 11-6S3

Figure 7.5: Shedding of a weak strake vortex during cruise flight

In summary, the utilisation of the strake configuration 11-6S3 leads to a drag increase in cruise flight of 0.222%, wheras a part of this increase results from a stronger strake vortex. The underlying calculations have been made for the beginning of the cruise flight, which characterises the point of the maximal aircraft weight and accordingly the maximal C_L. In a later stadium of the cruise flight, C_L will be lower and the induced drag of the strake will consequently decrease.

8 Conclusion

Within this research project the generic aircraft of the research project SFB 880, equipped with a droop nose and an active Coanda flap, has been investigated. In the landing configuration vortices shed by the large turboprop engines have caused a wake burst which has led to a significant lift loss near the flap trailing edge inboard of the nacelle. An initial strake that had been dimensioned in a foregoing study, has proven to allow for a partial lift recovery. However, an investigation has shown that an additional increase of $C_{L,max}$ could be achieved by a further modification of the strake. Therefore, a nacelle strake parameter study with the aim to maximise the maximum lift coefficient has been undertaken. Another objective of the parameter study should be to obtain a further understanding of the effects of the parameter variations.

In the first instance, a grid has been generated for the landing configuration, based on an unstructured hybrid grid. In order to obtain a better resolution of the inboard and outboard nacelle vortices as well as of the strake vortex, structured elements have been inserted into the wing panels. In addition, the nacelle wake has been discretised with structured elements, using hexahedral blocks. Modular grid generation has been utilised since it allows for a better comparability and reduces the numerical effort of the grid generation process.

The nacelle strake parameter study has comprised the variation of the streamwise strake position x_S, the vertical strake position z_S, the strake size factor f_S and the ratio between the strake root chord and its semispan h_S. In addition, the strake setting angle α_S has for a first approximation been set to the average value of $-\alpha_{cruise}$ of the conceptional aircraft to have a minor impact on cruise drag. Nevertheless, it has to be kept in mind that for a minimisation of additional drag in cruise flight the strake has to be installed parallel to the stream lines. Therefore, the optimal setting angle also depends on the streamwise and the vertical strake position. In the first step of the parameter study, various combinations of strake parameters have been investigated at $\alpha = 6°$. This has particularly been performed in order to find a design range on whose basis further investigations should be performed with respect to $C_{L,max}$. The aim of this procedure has particularly been the reduction of the numerical effort. Based on these results, further strake configurations have been analysed at α_{max}. Thereby, it has turned out that strakes located too close to the wing are less effective. The reason for this is the higher strength increase of the vortices due to the circulation field of the wing and the associated higher strake angle of attack. Furthermore, a higher vertical strake position has resulted in a greater lift recovery. In a final optimisation step, the strake size factor has been stepwisely increased. In combination with the optimised position the size increase has resulted in a further weakening of the nacelle vortex, which has allowed another increase of the maximum lift coefficient.

The highest $C_{L,max}$ could be obtained by a displacement of the strake by $200\ mm$ in x and $300\ mm$ in z-direction. In addition, its strake root chord-semispan ratio has been set to $h_S = 2.67$ which amounts 133% of the initial strake's ratio and the strake area has been increased to $f_S = 13.59$, which is equivalent to 226% of the initial area. This optimised strake allows for an increase of $C_{L,max}$ by around $17\ LC$ compared to the case without strake and by $3.2\ LC$ compared to the initial strake. Furthermore, important insights into the nature of these improvements have been gained. On the one hand, the vortex shed by the optimised strake has a greater distance to the wing's surface compared to the initial strake. On the other hand, its vortex passes closer to the nacelle vortex. It therefore has a greater potential of negating it without having a negative influence on the near surface flow. The strake size is therefore optimised in such a manner that the best compromise between weakening of the nacelle vortex and interaction with the near surface flow is found. However, apart from the increase of $C_{L,max}$, an augmentation of α_{max} could not be achieved. Nonetheless, investigations have shown that further potential to increase the maximum lift coefficient and probably α_{max} exist. Since the outboard nacelle vortex leads to a wake burst beyond $\alpha = 10°$, an outboard strake would result in further improvements. The findings achieved within this study can also accelerate and support a possible design of an outboard strake.

Within the next step, the strake impact on drag at the beginning of cruise has been determined. Therefore, an unstructured hybrid mesh without structured elements has been taken as a basis. The investigations have shown that the optimised strake leads to a supplementary drag of $0.66\ DC$ which is equivalent to an increase of 0.222% compared to the configuration without strake. Besides the increased profile drag of the strake, the position and strength of the strake vortex shed in cruise flight has caused another drag increase.

Nevertheless, all the results have solely been obtained by means of numerical simulations. It should be noted that numerical calculations are always subject to various influences, thereunder particularly the grid influence and the impact of the numerical setup. Due to the high complexity of the landing configuration of the aircraft, a grid convergence study has not been performed. Instead, the grid has been evaluated on a qualitative basis. Thereby, the wake region of the vortices on the wing has been refined locally in order to provide a better resolution of the vortices. The comparison between the solution on the coarse and the refined grid has shown that the vortices are less dissipated on the finer grid. The resulting higher strengths, particularly of the nacelle vortex has lead to a relative lift decrease along with the angle of attack. However, the qualitative behaviour of the flow and especially the locations of the vortices seemed to be identical. Therefore, it is probable that the additional lift decrease due to the higher strength of the vortices is lower for the optimised strake. Since the strake vortex has a better position with respect to the nacelle vortex, it has a better capability of weakening the nacelle vortex and therefore of reducing the additional lift loss on the refined grid. In addition, due to the high amount of calculations within this research project, the central discretisation scheme with scalar dissipation has been used. This is most likely to have another significant impact on the results since the vortices are again stronger dissipated. Assuming that the vortex propagation paths are also similar in case of lower dissipation, this might lead to the same effect like the refined grid.

Another influence could arise from the deployed turbulence model. In spite of the inclusion of a rotational and a vortical correction into the *Spalart-Allmaras turbulence model*, more sophisticated turbulence models like *Reynolds stress models* might be more suitable for the simulation of vortices.

9 Future Work

As already stated before, a couple of simplifications have been made within this nacelle strake parameter study in order to keep the numerical effort low. These simplifications are supposed to have a significant impact on the accuracy of the solution. After a wide range of strake parameter changes have been compared and evaluated, the first and most fundamental step of future tasks would be the evaluation of the optimised strake by more precise means or at least by estimation of the accuracy. In the first instance, the optimised strake could be calculated on the finer grid. that has already been generated for the grid evaluation. This very simple test could already identify if the strake size needs to be reduced. Alternatively, a grid convergence study could be processed for the actual grid. The solution for an infinitesimal fine grid could then be extrapolated and the results obtained for different strake configurations could be compared again.

In addition, the numerical setup could be modified in order to provide a more physical representation of the flow problem. First of all, the central discretisation scheme with matrix dissipation should be used. In addition, another turbulence model could be utilised. The *Spalart-Allmaras turbulence model* is based on the *Boussinesq eddy-viscosity hypothesis* which has deficiencies in flows with high turning angles [9]. It is indeed extended by a rotational correction, but it might however be more accurate to utilise a *Reynolds stress model*. Furthermore, the results of the numerical calculations, performed with a more accurate setup, should be validated by wind tunnel tests.

Another possibility of improving the inboard nacelle strake could be to consider a condition with respect to drag in cruise into the design process. Therefore, the streamlines in the proximity of the nacelle during the cruise flight need to be investigated first. The modification of either the streamwise strake position or the vertical strake position would then be accompanied by a change of the strake setting angle. As a result, drag could be reduced to a minimum.

The analysis of the optimised strake at $\alpha = 10^\circ$ showed a wake burst, caused by the outboard nacelle vortex. This leads to a rapid decrease of lift. Thus, an outboard strake should be designed. This would not only lead to another lift recovery at $\alpha = 10^\circ$ but could also allow for an increase of α_{max}.

In case it is taken into consideration to install the optimised inboard strake, it should be respected that, with a strake root chord of around $1\ m$, it has a very large size. In combination with its little thickness, a structural analysis would become absolutely necessary.

Bibliography

[1] Blazek, J., *Computational Fluid Dynamics: Principles and Applications*. Kidlington, Oxford: Elsevier Science, 2001.

[2] Brodersen, "Numerische Analyse der aerodynamischen Triebwerksinstallationseffekte an Transportflugzeugen", PhD thesis, 2003.

[3] Burnazzi, M. and Radespiel, R., "Design and Analysis of a Droop Nose for Coanda Flap Applications", *Journal of Aircraft*, vol. 51, no. 5, pp. 1567 to 1679, 2014.

[4] Burnazzi, M. and Radespiel, R., "Design of a Droopnose Configuration for a Coanda Active Flap Application", *AIAA 2013-0487*, 2013.

[5] CentaurSoft, "Website, https://www.centaursoft.com", [Accessed 15th december 2015].

[6] Dam, C. van, "The Aerodynamic Design of Multi-Element High-Lift Systems for Transport Airplanes", *Progress in Aerospace Sciences*, no. 38, pp. 101 to 144, 2002.

[7] Dassault Systems, "Website, http://www.3ds.com/products-services/catia", [Accessed 15th december 2015].

[8] Emunds, R., "Leading Edge Vortex System of the A380 at high Angles of Attack in Landing Configuration", Airbus Operations GmbH, Tech. Rep., 2012.

[9] German Aerospace Cente, "Technical Documentation of the DLR TAU-Code Release 2015.1.0", Tech. Rep.

[10] Haines, A. and Young, A., "Scale Effects on Aircraft and Weapon Aerodynamics", *AGARD-AG-323*, 1994.

[11] Institute of Aircraft Design and Lightweight Structures, "Website, https://www.tu-braunschweig.de/ifl/forschung/flugzeugvorentwurf", [Accessed 9th december 2015].

[12] Jensch, C., Pfingsten, K., Radespiel, R., Schuermann, M., Haupt, M., and Bauss, S., "Design Aspects of a Gapless High-Lift System with Active Blowing", *Deutscher Luft- und Raumfahrtkongress*, 2009.

[13] Keller, D., "Numerical Approach Aspects for the Investigation of the Longitudinal Static Stability of a Transport Aircraft with Circulation Control", *Notes on Numerical Fluid Mechanics and Multidisciplinary Design, Springer*, vol. 124, pp 13 to 22, 2014.

[14] Keller, D. and Rudnik, R., "Numerical Investigation of Engine Effects on a Transport Aircraft with Circulation Control", *Journal of Aircraft*, vol. 52, no. 2, pp. 421 to 438, 2015.

[15] Lengers, M., "Industrial Assessment of Overall Aircraft Driven Local Active Flow Control", *ICAS 2014 - 29th Congress of the International Council of the Aeronautical Sciences*, 2014.

[16] Neitzke, K.-P., Rudnik, R., and Schröder, A., "Low Speed Validation Tests on Engine/Aircraft Integration within the EC Project EUROLIFT II", *AIAA 2005-3704*, 2005.

[17] Pott-Pollenske, M., Alvarez-Gonzalez, J., and Dobrzybski, W., "Effect of Slat Gap on Farfield Radiated Noise and Correlation with Local Flow Characteristics", *9th AIAA/CEAS Aeroacoustics Conference*, 2003.

[18] Reckzeh, D., "Aerodynamic Design of the A400M High-Lift System", *ICAS 2008 - 26th International Congress of the Aeronautical Scienes*, 2008.

[19] Rudnik, R., "Stall Behaviour of the EUROLIFT High Lift Configurations", *AIAA 2008-836*, 2008.

[20] Schlichting, H., Krause, E., Gersten, K., and Oertel, H., *Grenzschicht-Theorie*. Springer, 2006.

[21] Schlichting, H. and Truckenbrodt, E., *Aerodynamik des Flugzeuges, Band 1: Grundlagen aus der Strömungsmechanik, Aerodynamik des Tragflügels (1)*. Springer Berlin Heidelberg, 2000.

[22] Schlichting, H. and Truckenbrodt, E., *Aerodynamik des Flugzeuges, Band 2: Aerodynamik des Tragflügels (2), des Rumpfes, der Flügel-Rumpf-Anordnung und der Leitwerke*. Springer Berlin Heidelberg, 2000.

[23] Smith, A., "High-Lift Aerodynamics", *Journal of Aircraft*, vol. 12, no. 6, pp. 501 to 530, 1975.

[24] Tikoff, B. and Fossen, H., "The Limitations of Three-Dimensional Kinematic Vorticity Analysis", *Journal of Structural Geology*, vol. 17, no. 12, pp. 1771 to 1784, 1995.

[25] Tritton, D., *Physical Fluid Dynamics*, ser. Oxford Science Publications. Clarendon Press, 1988.

[26] v. Geyr, H., Schade, N., Burg, J. v. d., Eliasson, P., and Esquieu, S., "CFD Prediction of Maximum Lift Effects on Realistic High-Lift-Aircraft-Configurations within the European Project EUROLIFT II", *AIAA*, 2007.

[27] Weiss, T. and Heinze, W., "Multidisciplinary Design of a CESTOL Aircraft with Powered Lift System", *Sonderforschungsbereich 880 - Biennial Report 2012*, 2012.

[28] Wild, J., "Experimental Investigation of Mach- and Reynolds-Number Dependencies of the Stall Behavior of 2-Element and 3-Element High-Lift Wing Sections", *AIAA 2012-0108*, 2012.

[29] Zhang, W., Chen, H., Zhang, Y., Fu, S., Chen, Y., Li, Y., and Zhou, T., “Numerical Research of the Nacelle Strake on a Civil Jet”, *ICAS2012*, 2012.

A Theoretical Background

A.1 The *Spalart-Allmaras Turbulence Model*

The differential form of the *Spalart-Allmaras turbulence model* with compressibility corrections is a transport equation for the SA viscosity

$$\mu^t = f_{v1}\widetilde{\rho}\widetilde{\nu} \tag{A.1}$$

given by the following equation, containing the closest wall distance d and the laminar kinematic viscosity ν^t [1], [9]:

$$\begin{aligned} \frac{\partial\widetilde{\nu}}{\partial t} + \frac{\partial}{\partial x_j}\left(\widetilde{\nu}v_j\right) = \; & C_{b1}\left(1 - f_{t2}\right)\widetilde{S}\widetilde{\nu} \; + \; \frac{1}{\sigma}\left[\frac{\partial}{\partial x_j}\left(\left(\nu^l + \widetilde{\nu}\right)\frac{\partial\widetilde{\nu}}{\partial x_j}\right) + C_{b2}\frac{\partial\widetilde{\nu}}{\partial x_j}\frac{\partial\widetilde{\nu}}{\partial x_j}\right] \\ - \; & \left(C_{w1}f_{w1} - \frac{C_{b1}}{\kappa^2}f_{t2}\right)\left(\frac{\widetilde{\nu}}{d}\right)^2 - \frac{1}{\sigma}\left(\nu^l - \widetilde{\nu}\right)\frac{\partial\widetilde{\rho}}{\partial x_j}\frac{\partial\widetilde{\nu}}{\partial x_j} \end{aligned} \tag{A.2}$$

The first term on the right-hand side represents the production of $\widetilde{\nu}$ and contains the following expressions [1]

$$\begin{aligned} f_{v1} = \frac{\chi^3}{\chi^3 + C_{v1}^3}\,, \quad f_{v2} = \left(1 + \frac{\chi}{C_{v2}}\right)^{-1}\,, \quad f_{v3} = \frac{\left(1 + \chi f_{v1}\right)\left(1 - f_{v2}\right)}{\max\left(\chi, 0.001\right)}, \\ \chi = \frac{\widetilde{\nu}}{\nu^l}\,, \quad \widetilde{S} = f_{v3}S + \frac{\widetilde{\nu}}{\kappa^2 d^2}f_{v2}\,, \quad S = \sqrt{2\Omega_{ij}\Omega_{ij}}\,, \quad \Omega_{ij} = \frac{1}{2}\left(\frac{\partial v_i}{\partial x_j} - \frac{\partial v_j}{\partial x_i}\right) \end{aligned} \tag{A.3}$$

In Equation A.3 Ω_{ij} is the rotation-rate tensor. The second term models the diffusion of the eddy viscosity. The third term on the right-hand side, accounting for the destruction of $\widetilde{\nu}$, contains the functions [1]

$$f_w = g\left(\frac{1 + C_{w3}^6}{g^6 + C_{w3}^6}\right)^{1/3}\,, \quad g = r + C_{w2}\left(r^6 - r\right)\,, \quad r = \frac{\widetilde{\nu}}{\widetilde{S}\kappa^2 d^2}. \tag{A.4}$$

The final term on the right-hand side is a compressibility correction. In addition, there are the terms that respect the laminar-turbulent transition [1]:

$$\begin{aligned} f_{t1} = C_{t1}g_t\exp\left(-C_{t2}\frac{\omega_t^2}{\Delta U^2}\left(d^2 + g_t^2 d_t^2\right)\right) \\ f_{t2} = C_{t3}\exp\left(-C_{t4}\chi^2\right)\,, \quad g_t = \min\left(0.1, \frac{|\Delta\vec{v}|}{\omega_t\Delta x_t}\right) \end{aligned} \tag{A.5}$$

The subscript "t" marks the so-called user-specified trip point and with this ω_t is the vorticity at the trip point, d_t is the local distance from the trip point, $|\Delta\vec{v}|$ is the absolute value of the difference between the current point and the trip point and Δx_t is the grid spacing at the trip point [1].

Finally, the constants used in the Equations A.2 - A.5 are defined as [1]:

$$C_{b1} = 0.1355\ , \quad C_{b2} = 0.622\ , \quad C_{v1} = 7.1\ , \quad C_{v2} = 5\ ,$$

$$\sigma = 2/3\ , \quad \kappa = 0.41, C_{w1} = \frac{C_{b1}}{\kappa^2} + \frac{(1 + C_{b2})}{\sigma}\ , \quad C_{w2} = 0.3\ , \quad C_{w3} = 2\ ,$$

$$C_{t1} = 1\ , \quad C_{t2} = 2\ , \quad C_{t3} = 1.3\ , \quad C_{t4} = 0.5$$

It should be noted that there are various versions of the *Spalart-Allmaras turbulence model*. Depending on the version, the different terms can slightly vary and additional terms can occur [9].

A.2 *Navier-Stokes Equations*

In order to provide a better readability and clarity, the complete system of the *Navier-Stokes equations* without external sources can be expressed in the compact form if the conservative variables inside the stationary control volume and the fluxes over the boundary are separated. The set of equations then reads

$$\frac{\partial}{\partial t} \iiint\limits_{\Omega} \vec{W}\, d\Omega + \iint\limits_{\partial\Omega} \overline{\overline{F}} \cdot \vec{n}\, dS = 0. \tag{A.6}$$

The vector $\vec{W}$ contains the conservative variables:

$$\vec{W} = \begin{pmatrix} \rho \\ \rho u \\ \rho v \\ \rho w \\ \rho E \end{pmatrix} \tag{A.7}$$

The flux density vector contains the convective (subscript "c") and the viscous (subscript "v") fluxes [1]

$$\vec{F} = \vec{F}_c - \vec{F}_v = \overline{\overline{F}} \cdot \vec{n}, \tag{A.8}$$

which can be expressed as [1]:

$$\vec{F}_c = \begin{pmatrix} \rho(\vec{n} \cdot \vec{v}) \\ \rho u(\vec{n} \cdot \vec{v}) + n_x p \\ \rho v(\vec{n} \cdot \vec{v}) + n_y p \\ \rho w(\vec{n} \cdot \vec{v}) + n_z p \\ \rho H(\vec{n} \cdot \vec{v}) \end{pmatrix} \quad , \quad \vec{F}_v = \begin{pmatrix} \vec{0} \\ n_x\tau_{xx} + n_y\tau_{xy} + n_z\tau_{xz} \\ n_x\tau_{yx} + n_y\tau_{yy} + n_z\tau_{yz} \\ n_x\tau_{zx} + n_y\tau_{zy} + n_z\tau_{zz} \\ n_x\Theta_x + n_y\Theta_y + n_z\Theta_z \end{pmatrix} \tag{A.9}$$

while Θ denotes [1]:

$$\vec{\Theta} = \begin{pmatrix} u\tau_{xx} + v\tau_{xy} + w\tau_{xz} + k\frac{\partial T}{\partial x} \\ u\tau_{yx} + v\tau_{yy} + w\tau_{yz} + k\frac{\partial T}{\partial x} \\ u\tau_{zx} + v\tau_{zy} + w\tau_{zz} + k\frac{\partial T}{\partial z} \end{pmatrix}$$

Assuming the eddy-viscosity hypothesis Equation A.6 can be transformed into the RANS equation, by substituting the shear stress tensor and the thermal conductivity coefficient by

$$\overline{\overline{\tau}} = \overline{\overline{\tau^l}} + \overline{\overline{\tau^t}} \tag{A.10}$$

$$k = k^l + k^t, \tag{A.11}$$

Substituting these values by sums of the molecular values, occuring in laminar flow and the modelled turbulent values, turbulence can be taken into account.

B Supplementary Figures

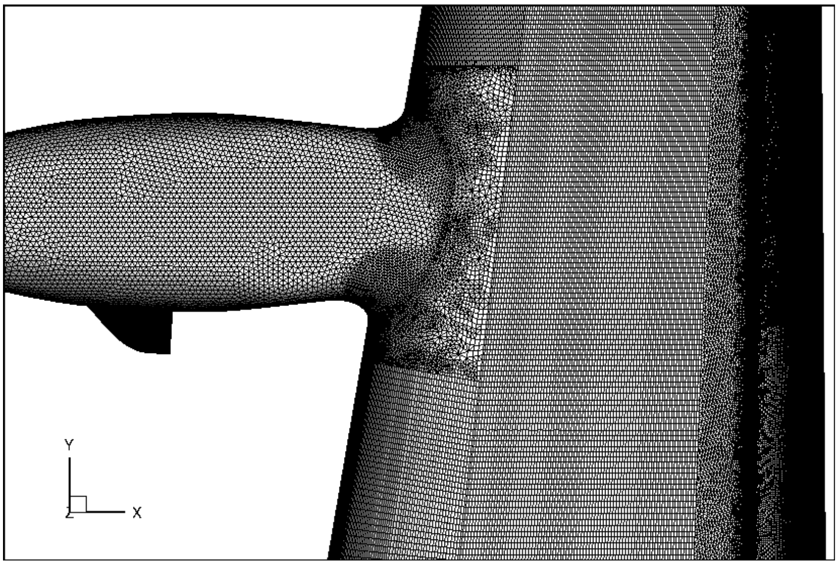

Figure B.1: Basic surface grid in the nacelle wake region

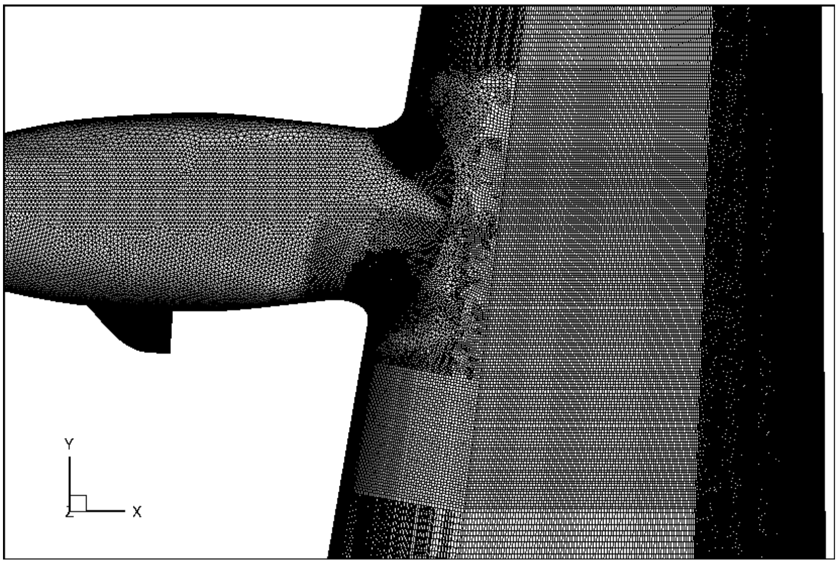

Figure B.2: Refined surface grid in the nacelle wake region

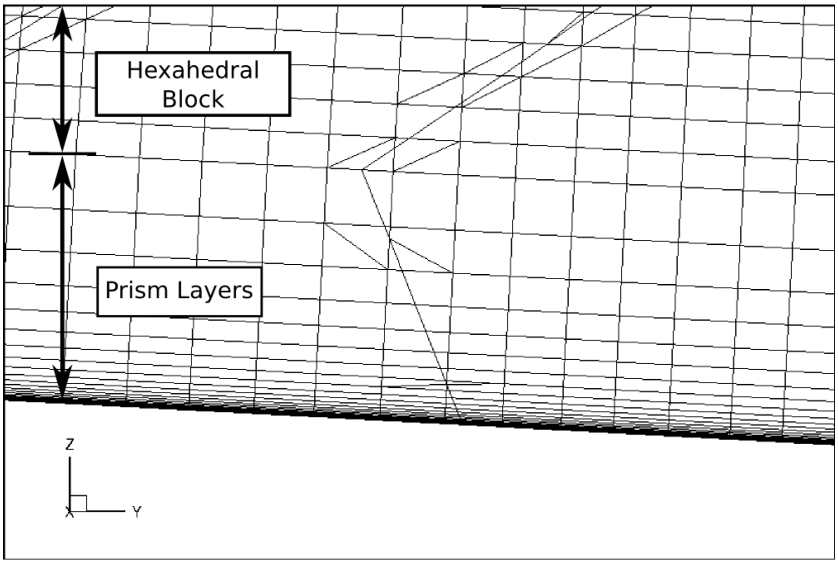

Figure B.3: Cut through basic grid showing prism layers of the wing at $x = 14.0\ \mathrm{m}$

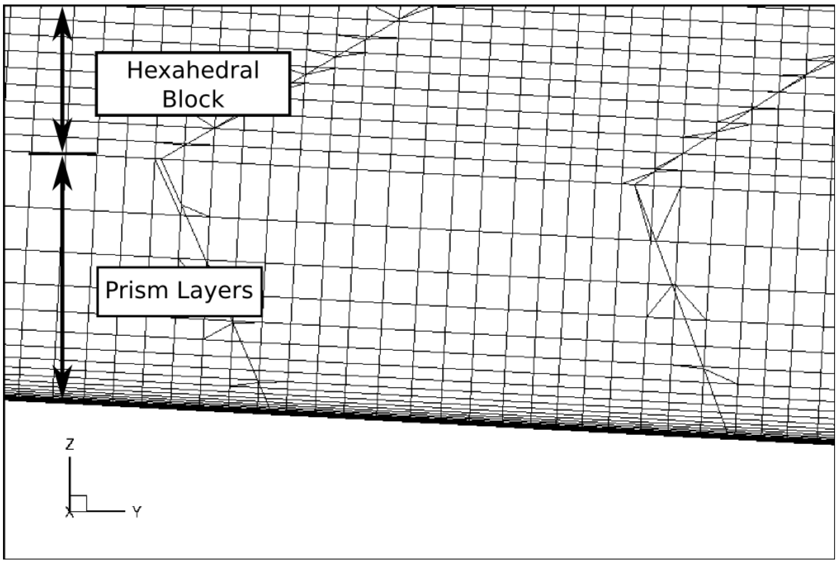

Figure B.4: Cut through refined grid showing prism layers of the wing at $x = 14.0\ \mathrm{m}$

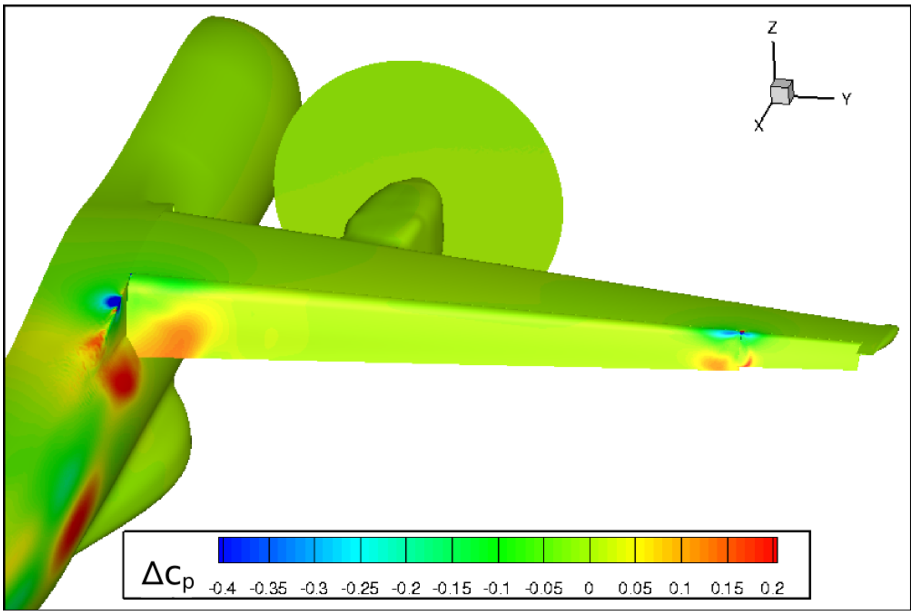

Figure B.5: High-frequency variations of c_p during calculation without strake, $\alpha = 6°$

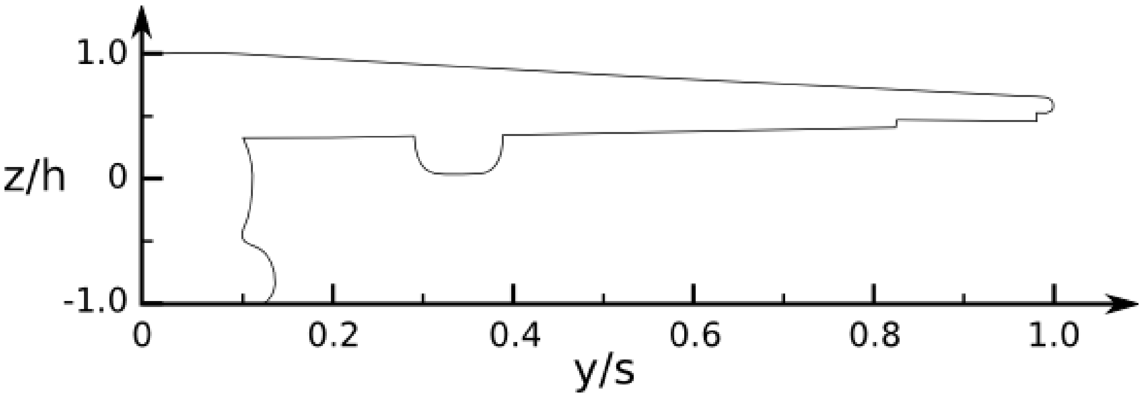

Figure B.6: Normalised wing coordinate system in yz-plane

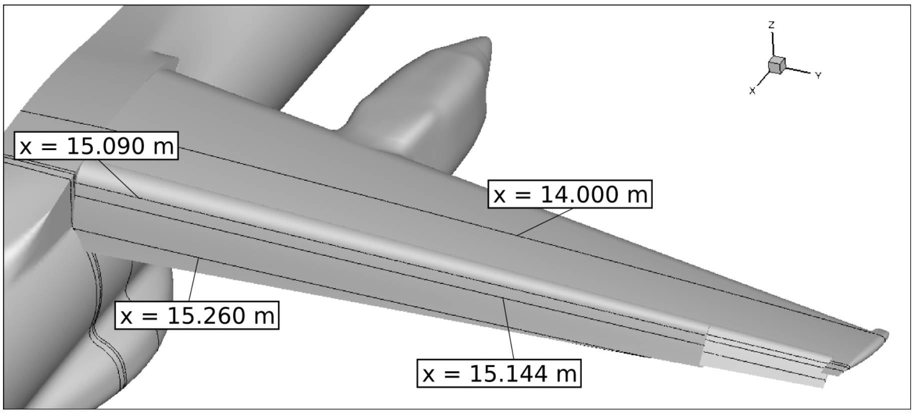

Figure B.7: Overview of the cutting planes used within this project

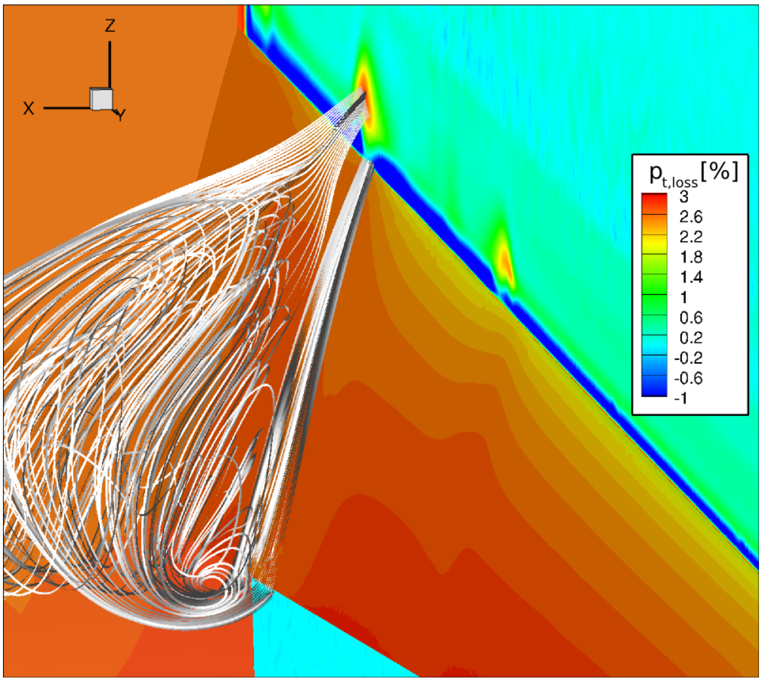

Figure B.8: Wakeburst above the flap for configuration 11-6 at $\alpha = 8°$

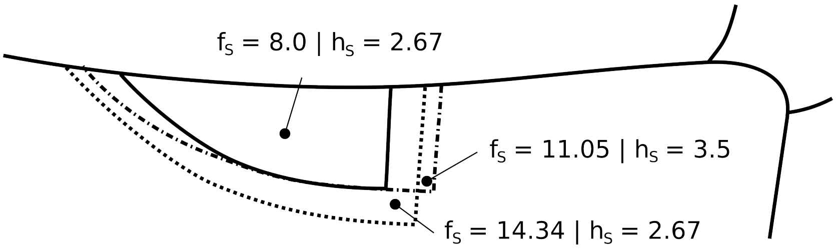

Figure B.9: Geometry variations of the strake at $x_S = 200$ mm and $z_S = 200$ mm

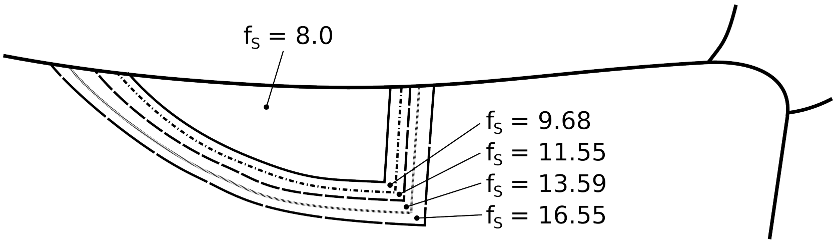

Figure B.10: Final optimisation of the strake geometry at $x_S = 200$ mm and $z_S = 300$ mm

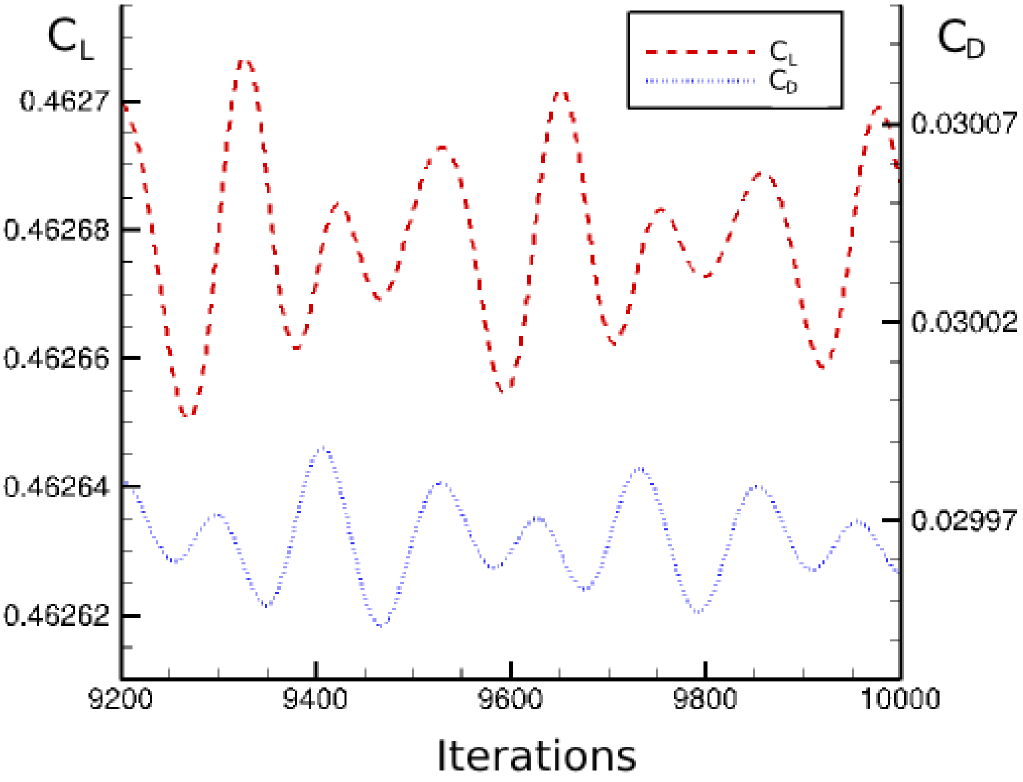

Figure B.11: Convergence behaviour of the cruise configuration, close-up view

C Aerodynamic Coefficients

C.1 Lift Coefficients in High-Lift Configuration

x_S [mm]	z_S [mm]	f_S	h_S	$C_L(6^\circ)$
-200	-100	6.0	2.0	3.1046
-200	0	6.0	2.0	3.1082
0	-100	6.0	2.0	3.1055
0	0	10.68	2.0	3.1169
0	0	8.0	2.67	3.1154
0	100	6.0	2.0	3.1117
0	150	6.0	2.0	3.1136
0	200	6.0	2.0	3.1140
0	200	8.0	2.67	3.1186
0	250	6.0	2.0	3.1117
100	0	6.0	2.0	3.1094
200	0	6.0	2.0	3.1098
200	200	6.0	2.0	3.1141
200	250	6.0	2.0	3.1107
400	0	6.0	2.0	3.1084
400	100	6.0	2.0	3.1099
400	200	6.0	2.0	3.1160
400	200	8.0	2.67	3.1226
400	250	6.0	2.0	3.1171
600	0	6.0	2.0	3.1052

Table C.1: Lift coefficients of single calculations at $\alpha = 6^\circ$

Configuration	$C_L(0^\circ)$	$C_L(6^\circ)$	$C_L(7^\circ)$	$C_L(8^\circ)$	$C_L(9^\circ)$	$C_L(10^\circ)$	$C_L(11^\circ)$	$C_L(12^\circ)$	$C_L(13^\circ)$
11-6	2.6906	3.0797	3.1048	**3.1241**	3.1092	3.0796	3.0646	3.0782	3.0820
11-6S2	2.6914	3.1100	–	3.2044	3.2434	**3.2598**	3.2564	3.2389	3.2065
11-6S3	2.7012	3.1411	–	3.2418	3.2434	**3.2920**	3.2686	3.2259	3.1925

Table C.2: Lift coefficients of the main configurations

x_S [mm]	z_S [mm]	f_S	h_S	$C_L(0^\circ)$	$C_L(6^\circ)$	$C_L(8^\circ)$	$C_L(10^\circ)$	$C_L(11^\circ)$	$C_L(12^\circ)$	$C_L(13^\circ)$
0	-100	8.0	2.67	2.7033	3.1087	3.2172	**3.2772**	3.2689	3.2505	3.2496
200	-100	6.0	2.0	2.5634	3.1118	3.2079	**3.2647**	3.2621	3.2519	3.2310
200	200	8.0	2.67	2.5813	3.1237	3.2244	**3.2790**	3.2675	3.2440	3.2422
200	200	14.34	2.67	2.7106	3.1382	3.2348	**3.2460**	3.1989	3.1071	3.0872
200	200	11.05	3.5	2.6921	3.1308	3.2290	**3.2607**	3.2220	3.1515	3.0934

Table C.3: Further lift coefficients for complete lift curves

x_S [mm]	z_S [mm]	f_S	h_S	$C_L(6°)$	$C_L(8°)$	$C_L(10°)$	$C_L(11°)$
200	250	8.0	2.67	3.1219	3.2252	**3.2807**	3.2683
200	250	3.55	2.67	3.1072	3.2052	**3.2556**	3.2473
200	300	8.0	2.67	3.1244	3.2266	**3.2821**	3.2696
200	300	9.68	2.67	3.1301	3.2315	**3.2852**	3.2678
200	300	11.55	2.67	3.1339	3.2358	**3.2891**	3.2720
200	300	16.55	2.67	3.1445	3.2474	**3.2853**	3.2514
200	350	8.0	2.67	3.1244	3.2255	**3.2810**	3.2678
200	400	8.0	2.67	3.1181	3.2204	**3.2745**	3.2601
400	250	8.0	2.67	3.1228	3.2247	**3.2602**	3.2395

Table C.4: Further lift coefficients for partial lift curves

C.2 Drag Coefficients in Cruise Configuration

Configuration	$C_D(C_L = 0.463)$
11-6	0.0299647
11-6S2	0.0299984
11-6S3-f_S=8.0	0.0300078
11-6S3	0.0300311

Table C.5: Drag coefficients in cruise flight

DLR-IB-AS-BS-2017-10

Numerical Parameter Study of a Strake on a Turbo-prop Engine in Active High-Lift Configuration

Yasim Julian Hasan, Dennis Keller

Verteiler:

Institutsbibliothek	1 Exemplar
Verfasser/Co-Autoren	2 Exemplare
Institutsleitung	1 Exemplar
Abteilungsleiter	1 Exemplar
Deutsche Bibliothek in Frankfurt/Main	2 Exemplare
Niedersächsische Landesbibliothek Hannover	1 Exemplar
Techn. Informationsbibliothek Hannover	1 Exemplar
Zentralbibliothek BS	1 Exemplare
Zentralarchiv GÖ	1 Exemplar
Reserve	5 Exemplare